The Dissertation Committee for Jimmy Li-Shin Su Certifies that this is the approved version of the following dissertation:

Clinical photoacoustic imaging for detection and characterization of metal implants

Committee:

Stanislav Y. Emelianov, Supervisor

Andrew Dunn

Andrei Karpiouk

Richard Smalling

Konstantin Sokolov

Clinical photoacoustic imaging for detection and characterization of metal implants

by

Jimmy Li-Shin Su, B.S. BME; M.S.E.

Dissertation

Presented to the Faculty of the Graduate School of

The University of Texas at Austin

in Partial Fulfillment

of the Requirements

for the Degree of

Doctor of Philosophy

The University of Texas at Austin

August 2011

Dedication

To my parents who have loved and supported me

through all the successes and failures.

And to my beautiful wife, Carolyn,

whom apart from the Savior I have received no greater gift.

Acknowledgements

As I write this at the end of a seven year journey, there stands a legion of people who have supported me along the way. At times it was difficult to imagine the end of this season of life. Without the support of these individuals I would not be here today.

First of all, my utmost thanks and appreciation to my advisor, Dr. Stanislav Emelianov, who took me on as a lowly grad student with very little medical imaging experience. His guidance, both scientifically and personally, through the last four years, have helped to shape me into the person that I am today. I am also grateful for the financial support provided by him during my graduate work. Thank you, Stas, for your kindness and generosity to me and my family.

Thanks also goes to Dr. Richard Smalling and Jim Amirian at UT Health Science Center for helping with the animal studies, both regarding animal care and surgical procedures. Thank you also to Nadine Matthias at UTHSC who performed many of animal surgical procedures early on for our lab. To Dr. Andrew Dunn, I express my thanks for teaching me much in his Optical Spectroscopy course. To Dr. Konstantin Sokolov, who has developed a very close relationship with our lab, thank you for your insight and guidance with regards to my dissertation proposal and final research plans.

I also offer my deepest thanks to my labmates in the Ultrasound Imaging and Therapeutics Laboratory at the University of Texas at Austin. I look on my time here with fond memories as it was a joy to work with a collective group of such intellectual individuals. In particular, thanks to Bo Wang and Andrei Karpiouk for their tremendous insight regarding my project as well as teaching me about photoacoustics and imaging processing. Thank you to Iulia Graf who gave me invaluable support regarding cardiovascular physiology and who painstakingly took it upon herself to proofread my dissertation cover-to-cover and provide feedback on each section. Her edits and suggestions have served to make this dissertation stronger than it was before. For their insight and discussions on underlying physics and theory, I thank Yun-Sheng Chen, Wolfgang Frey, Kimberly Homan and Salavat Aglyamov for their help. Thanks also to Richard Bouchard whose research collaboration was very encouraging. Life in the office was never a dull moment thanks to the combined efforts of Jason Cook, Doug Yeager, Mohammad Mehrmohammadi and Seungsoo Kim. I enjoyed the many conversations we had on a plethora of topics on any given day.

I would like to acknowledge the faculty and staff in the Biomedical Engineering Department for their invaluable support throughout my graduate studies, especially Dr. Krishnendu Roy, Heidi Mallon, Carol Noriega and Tera Sherrard. Furthermore, I extend my gratitude to my lab, department, and the University for providing me with all the facilities throughout my degree program.

I owe a tremendous amount of debt to friends who believed in me throughout my graduate studies. Thank you to Ricky and Geoff for weekly lunches on campus. Thanks to Alex for your constant prayers on me and my family. Thank you Derrick and Angela for your love and encouragement each time I went to Houston. Thanks to Tim who I could always count on to ask how I was doing. And to countless others who supported me along the way. Your friendship is a gift to me.

Last, but certainly not least, thank you to my loving family for their support and encouragement throughout the years. Thank you to Mom, Dad and Janice for your care and love to me. Thank you for your never-ending love, patience, kindness and wisdom even when I did not deserve it. Thank you also to my parents-in-law, who treated me as one of their own family members from day one. To my precious Chloe, you bring me joy and amazement each day as I watch you grow. A thousand successes in this life could never make me as happy as you do. Finally, thank you to my amazing wife Carolyn who has always stood by my side regardless of the outcome, who has been there in my greatest times of need, and who encourages me to do my best in all things.

Clinical photoacoustic imaging for detection and characterization of metal implants

Jimmy Li-Shin Su, Ph.D.

The University of Texas at Austin, 2011

Supervisor: Stanislav Y. Emelianov

Accurate insertion and monitoring of metal implants in-vivo is essential for clinical diagnosis and therapy of various diseases. Clinical studies and examples have demonstrated that the misplacement errors of these metal devices can have dramatic consequences. This thesis focuses on three main metal devices that are in widespread use today: needles, coronary stents and brachytherapy seeds. Each application requires proper image-guidance for correct usage. For needles, image guidance is required to ensure correct local injection delivery or needle aspiration biopsy. Fine needle aspiration biopsies are performed in order to avoid major surgical excisions when obtaining tissue biopsy procedures. However, because of the small biopsy sample, the risk is that the sample is collected outside of the tumorigenic region, resulting in a false negative result. Implantation of stents requires that confirmation that proper stent apposition has been achieved due to balloon inflation. Furthermore, it is important to guide the stent to shield the vulnerable region of an atherosclerotic plaque. With prostate brachytherapy seeds, the ability to monitor seed placement is crucial because needle deflections or tissue deformation can result in seed misplacement errors, decreasing the efficacy of the pre-established treatment plan.

For the described applications and other possible clinical practices involving the use of metallic implants, an imaging technology that can accurately depict the location of the metal objects, relative to their respective backgrounds, in real-time, is necessary to improve the safety and the efficacy of these procedures.

Currently, ultrasound is used because of its real-time capabilities, non-ionizing radiation, and soft tissue contrast. However, due to high acoustic scattering from tissue, the contrast of metal implants can be low. Photoacoustic imaging can be used as an alternative, or complementary, imaging method to ultrasound for imaging metal. This thesis focuses on the benefits and the pitfalls of using photoacoustic imaging for detecting three different metal implants, each having unique requirements. Overall, the goal of this work is to develop a framework for clinical applications using combined ultrasound and photoacoustic imaging to help guide, detect and follow-up on clinical metal implants introduced in-vivo.

Table of Contents

List of Figures

Chapter 1: Introduction

1.1 Background

A wide variety of metal devices are used for temporary or permanent implantation into the human body. These devices can range from orthopedic or dental implants to smaller vascular endoprostheses. The use of metal devices in the human body is advantageous due to the strong biocompatibility, durability and high resistance to degradability of metal in the body [1]. However, the wide use of various metals and alloys has led to complications with the degradation products produced as a result of wear and corrosion [1-3]. The longer a metal is implanted in the body, the greater the need to monitor corrosion or movement. The need for monitoring also stems from the need to track the position of the metal and the environment in which it resides or passes. These metal devices can include temporarily implanted parts such as hypodermic needles for therapy which require image-guidance to accurately deliver injections to tumor sites. Accurate real-time imaging is necessary to guide the implant to the targeted location and to monitor the metal device's position and surrounding environment [4]. Furthermore, once the metal implant has been delivered, there exists a need to monitor the progression of these metal implants in the body with high accuracy and high contrast. Accurate real-time imaging is necessary to guide the installation of the metal device, to monitor the device's orientation, and to determine its impact on the in-vivo environment. Some devices are permanently implanted in the body, while others are temporarily implanted, such as hypodermic needles. Image-guidance is required in both cases to accurately

therapy to a local region of interest, such as in the latter case where a needle is used to deliver injections to tumor sites in therapy. Detection is needed to know the position of the metal object, as well as the environment in which it is located.

In this study, we propose the combination of photoacoustic and ultrasound imaging to accurately visualize specific metal objects used in clinical settings, and to image the position of these implants relative to the surrounding tissue. Imaging at different wavelengths and fluences, as well as performing different signal processing methods on the photoacoustic signal provides a necessary framework for developing new clinical methods to accurately image these metal objects in real-time.

1.2 Clinical Relevance

Currently, the most commonly used clinical strategy to visualize metal objects in real-time is ultrasound-guidance [5]. However, ultrasound alone is unable to visualize metal implants under all circumstances. In particular, the specular reflectivity of metal can cause the ultrasound beam to be reflected away from the transducer, rendering the metal object invisible. Visibility of the metal is highly dependent on the orientation angle of the metal surface incident with the ultrasound beam [6] and is best visualized only when this metal surface is perpendicular to, and in, the plane of the ultrasound transducer. Furthermore, the presence of background scatterers and acoustic artifacts in metal can introduce difficulties in accurately determining the exact location and orientation of metal objects.

An illustrative example of one such metal object is a metal injection needle which is commonly used for drug delivery, such as in cancer therapy, or for tissue collection in biopsy [5]. In these cases, the ability to visualize both anatomical surrounding structures and the advancing needle tip is required [7]. Needle deflection and deformation can occur when inserting needles into soft, non-homogeneous tissues [8] which can affect the location accuracy of insertion [9]. In ultrasound however, the needle tip oftentimes can be visualized better than the needle shaft because of the irregular surface of the machined cutting bevel which scatters the ultrasound (US) beam in all directions which reflects the beam, in part, back to the transducer [7]. Specular reflections from the metal surface can also deflect the ultrasound beam away from the transducer. To overcome these issues, mechanical or optical needle guides are used to keep the syringe needle in the transducer plane [10, 11]. However, these guides restrict needle movement when fine adjustments are needed by medical operators. Many clinicians prefer using a freehand technique during syringe operation [4]. Additionally, special surface-treated metal needles have been introduced in order to increase ultrasonic visualization. Surface treatments can include etching or polymeric coating that produce contrast bubbles when immersed in water. These needles have been shown to increase and improve visualization for clinicians performing biopsy procedures [12, 13].

Metal implants also include brachytherapy seeds, which are used to deliver localized radiation therapy to prostate cancer. The use of brachytherapy has been shown to be more effective than external beam radiation, as radiation delivery is localized and

dose is minimized [14]. Brachytherapy implantation requires accurate needle insertion into the prostate in order to maximize dose to the cancerous gland. In needle implantation of brachytherapy seeds, a needle deflection of 5 degrees from the insertion angle decreases the minimum target dose by 10% and increases the tumor-cell survival rate by a factor of 200 times [9]. The standard imaging modality for guidance of implantation of brachytherapy seeds is transrectal ultrasound (TRUS) [15]. Detection of seeds during post-surgery follow-up is conducted using X-Ray, CT or MRI, anywhere from 3 hours to 4 weeks after the implantation procedure. At this point, dose corrections can only be accomplished with external-beam radiation therapy [15]. Therefore, accurate detection and localization of seed placement in-vivo is required for proper treatment. Difficulties in using TRUS for detecting brachytherapy seeds are similar to the difficulties of using ultrasound for detecting needles. The smooth surface of the brachytherapy seeds strongly reflects ultrasound waves, the direction of which is highly dependent on the angle of the seed in relation to the transducer. Post-implantation studies have shown that radioactive seeds can drift over time, moving around the prostate, or even migrating to other parts of the body [16-18]. Use of X-ray or scintigraphy can only visualize a two-dimensional projection with little to no depth information for locating the seeds.

A third type of metal device commonly implanted in the body is the coronary artery stent. Coronary stents are used to treat blockage sites of coronary arteries by expanding a mesh-like tube in an artery that has been pre-dilated through balloon angioplasty. The use of coronary stents is the most widely used coronary intervention in

the United States. While the procedure is more than 95% successful [19], several unique issues affect stents including restenosis, hyperplasia [20], stent thrombosis [21] and stent drift. The ability to visualize stents both during the stenting procedure and during post-surgery follow-up is important in order to correctly assess the stent with respect to the plaques and vessel, and also identify its apposition within the vessel wall. Apposition is defined as the position of the stent strut to the lumen wall. Immediately following a stenting procedure, it is important to determine that the structure of the stent struts is in direct contact to the vessel wall. Ideally, the stent would be deployed in contact with the lumen wall; however, malapposition can occur resulting in the stent detaching itself from the wall. This can cause turbulent eddies to form in the vessel which can lead to thrombosis in the area of the stent. It is important when monitoring the stent to determine how much restenosis has formed around the stent struts. This distance that the stent struts are embedded into the vessel wall must be determined to assess stent viability. Currently, the most common method for assessing stent position is x-ray coronary angiography/fluoroscopy [22]. However, this procedure is problematic due to use of ionizing radiation and possible complications in using iodinated contrast agents. Furthermore, x-ray fluoroscopy can only depict a two-dimensional projection which can lead to an underestimation of the lumen diameter and the stent apposition within the lumen.

Magnetic resonance imaging (MRI) has been used to image stents due to its avoidance of radiation exposure and iodine contrast agents; however, the metallic

composition of stents can cause susceptibility artifacts, which can obscure the stent lumen and make it very difficult to visualize the relation between the stent and the vessel wall [19, 23]. Long scan times and low resolution also remains a major limitation of MRI. Multi-slice computed tomographic angiography (MSCTA) has been shown to image much faster than MRI; however, its low resolution and artifacts in metallic stents make assessing the surrounding vessel difficult [24].

Both intravascular ultrasound (IVUS) and optical coherence tomography (OCT) have reached widespread use in visualizing stents. IVUS can obtain bright signal reflections from the stent struts, but has insufficient contrast and resolution to determine its position against the vessel wall [25]. Extraneous beams of ultrasound generated from metallic stents can obscure the edges of the stent borders [26]. OCT directly competes with these disadvantages with a resolution of 10-20 μm but has severe depth limitations, allowing only a penetration depth of about 2 mm [27, 28]. The presence of blood flowing through the vessel limits this depth even further, requiring clinicians to flush the vessel during the imaging procedure [25, 29]. Furthermore, the tissue behind the stent strut becomes hidden due to scattering shadows in OCT, which prevents complete diagnosis of the stent's relation to the vessel lumen [25].

1.3 Combined Ultrasound (US) and Photoacoustic (PA) Imaging

Ultrasound is primarily used in clinical settings to detect metal implants because it does not require ionizing radiation, and the imaging modality has real-time capabilities. Ultrasound transducers can be designed in many shapes and sizes. The fundamental

operation of the imaging modality operates by transmitting an acoustic pulse, which is then reflected and/or scattered from tissue landmarks back to the transducer. Reconstructed images can provide structural and morphological information based on the acoustic scatterers present in the tissue. Ultrasound also demonstrates good resolution and sufficient penetration depth when imaging deep structures compared to optical imaging modalities which can only penetrate ~1 mm below the surface of the tissue. Furthermore, the imaging devices can be portable, increasing their utility in a variety of clinical operations. Ultrasound proves its effectiveness in imaging metal since a metallic surface is highly acoustically reflective. Specular reflections of acoustic signals transmitted in imaging are reflected back to the transducer with very little scatter or acoustic absorption from the metal itself. Since ultrasound can provide structural and morphological information of the tissue, the metal implant can be visualized in the context of the tissue for accurate placement and/or assessment of the implant itself. However, as previously stated, ultrasound is not flawless. Specular reflection of the acoustic pulse can render the metal invisible in ultrasound as the transmitted pulse can be reflected off the metal and away from the transducer. As the metal surface is angled away from the plane perpendicular to the propagated acoustic beam, the metal appears with markedly less contrast in the resulting b-mode image. Coupled with the ultrasound speckle from the background tissue, a shallow angle can decrease contrast enough that the metal object is unable to be seen. Ultrasound imaging of metal also produces artifacts known as comet-tails which result from the reverberation of the acoustic pulse within the metal itself [30,

31]. These comet-tail artifacts prevent accurate assessment of the metal implants' positioning in the processed ultrasound image.

A new imaging modality that has recently been introduced is photoacoustic imaging, which is based on the photoacoustic effect [32]. Briefly, the photoacoustic effect results from irradiating tissue with a short-pulsed laser beam in order to produce a thermal and acoustic response [33-35]. Light energy that is absorbed by tissue chromophores in a local region is converted into heat, and then converted into pressure due to the thermoelastic expansion of the tissue [36]. An ultrasound transducer detects the produced pressure, which is linearly related to the optical absorption coefficient, μ_a, the localized laser fluence, Φ, and the Grüneisen coefficient, Γ, of the surrounding environment, as seen in Equation 1.1.

$$P_0 = \mu_a \cdot \Phi \cdot \Gamma \qquad \textit{(Eq. 1.1)}$$

The main advantage in using photoacoustic imaging over ultrasound to view metal is the high contrast of the metal object relative to the background tissue. The optical absorption of 316L stainless steel, a material widely used in clinical implant devices because of its low corrosion and high biocompatibility, is several orders of magnitude higher than tissue constituents (Fig. 1) [37, 38]. Furthermore, the photoacoustic signal is produced omni-directionally from the area of laser irradiation, which avoids the effect whereby the acoustic signal is reflected away from the receiving transducer, such as in ultrasound [7, 39].

Multi-wavelength, or spectroscopic, photoacoustic imaging can be used to reconstruct the local optical absorption spectrum in the imaged regions of interest [40]. By normalizing the acquired photoacoustic signals to their local fluence and the Grüneisen coefficient of the environment, the absorption coefficient can be backcalculated at the corresponding wavelengths. Examining the unique absorption spectra from metal, water-based tissue or lipid-filled plaques can determine the composition of the corresponding photoacoustic image. The ability to image at different wavelengths and fluences [41], as well as perform different signal processing methods on the photoacoustic signal provide a necessary framework for developing new clinical methods to accurately image metal implants in real-time.

It should be mentioned that disadvantages exist in using photoacoustic imaging alone over ultrasound imaging for the purpose of visualizing metal implants. Generally, PA imaging cannot offer the soft tissue contrast that US imaging can provide. Therefore PA imaging alone lacks the ability to visualize tissue landmarks from which position information can be identified. To remedy this issue, we propose the combination of photoacoustic and ultrasound imaging to accurately visualize specific metal objects used in clinical settings, and to image these implants relative to surrounding tissue. The combination of photoacoustic with ultrasound is intuitive because both modalities operate using the same receive electronics. Furthermore, the two modalities complement each other in these applications: ultrasound can image the morphological and structural

information of the tissue, and photoacoustic can image the location of the metal relative to that tissue structure.

1.4 Surrounding Environmental Effects

To further identify the surrounding environment of the metal implant, characterization of tissue composition is required. Studies have also shown that the surrounding environment affects the photoacoustic signal intensity. As shown in Equation 1.1, photoacoustic imaging is directly related to the dimensionless Grüneisen coefficient, Γ:

$$\Gamma = \frac{\beta \cdot c^2}{C_p} \qquad \textit{(Eq. 1.2)}$$

The variable C_p is the heat capacity at constant pressure. The volume expansion coefficient, β, and the speed of sound, *c*, are both temperature dependent and linearly proportional to temperature [42, 43]. Studies have shown that on the nano scale, the photoacoustic response is primarily dictated by the environment [44]. The environment-dependence of the photoacoustic signal is thereby affected by the boundary between the nano-sized particle and the surrounding liquid environment by which heat diffusion propagates from the particle into the surrounding medium [45]. Previous work has shown that this change in photoacoustic amplitude is due to temperature effects which can cause the vaporization of water at the surface of metal nanoparticles [46]. The size of the absorber was shown to affect the photoacoustic amplitude based on this surface phenomenon. Though these boundary effects may not scale linearly going from the nano-

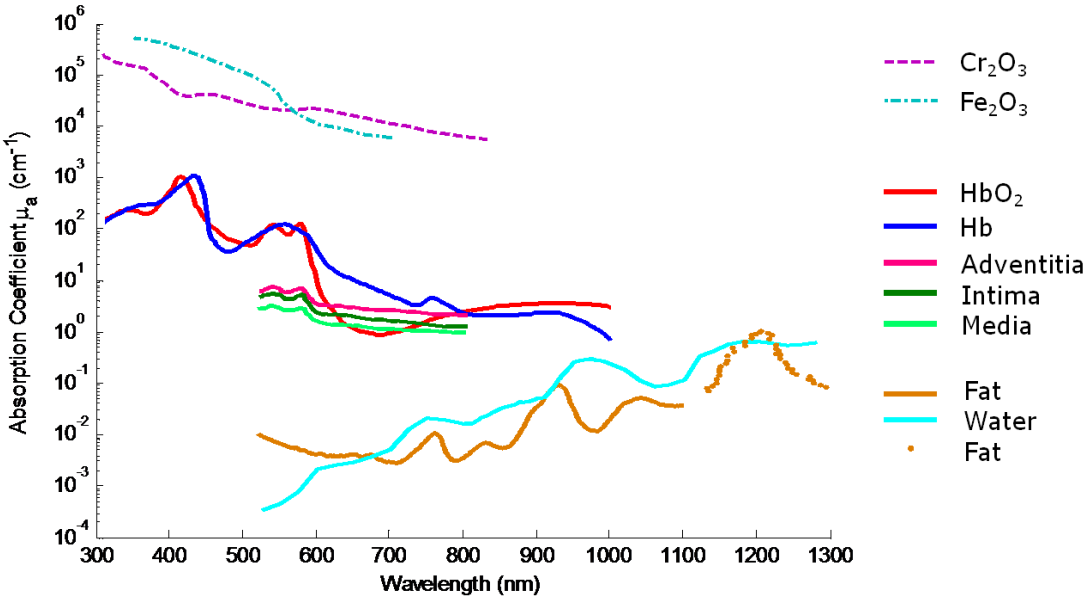

Figure 1.1: Optical absorption of tissue constituents in blood vessels compared with the main components found in 316L stainless steel. The stainless steel core consists of Fe2O3, while Cr2O3 is the outer passivation layer, which is responsible for the corrosion resistance of stainless steel. (Adapted from [37, 38]).

scale to the bulk solid scale, research has shown that heat propagation between a solid absorber and a liquid medium can still affect the photoacoustic signal [47]. Therefore, it is hypothesized that the heterogeneities in the Grüneisen coefficient should directly affect the photoacoustic response of a metal implant depending on the tissue environment in which it is inserted into [44, 48]. Environment-dependent signals could serve as confirmation that the metal object being implanted in-vivo has accurately arrived at the targeted region of interest.

Tissue composition can also be accomplished through detection of optical absorption coefficients. Since most tissue chromophores contain lower optical absorption, multi-wavelength or spectroscopic photoacoustic imaging is necessary to detect and distinguish between endogenous contrast agents. By acquiring images at multiple wavelengths and then processing the data through a spectroscopic analysis, quantitative measurements regarding the absolute concentration of specific chromophores can be obtained. Spectroscopic PA imaging has been used to detect functional information such as oxygen saturation in blood vessels and tumor regions with laser wavelengths in the NIR region [49]. PA imaging in the range of 1210 nm has been shown to provide contrast for lipid composition in atherosclerotic plaques [50]. With a priori knowledge of the spectral differences between various chromophores, it is possible to quantify the concentrations of these constituents. In addition to characterizing endogenous chromophore concentrations, spectroscopic imaging techniques can also be used to detect the presence of metal based on the unique spectra found in stainless steel (Fig 1.1).

1.5 AIM OF THE THESIS

The aim of the research described in this thesis is to investigate and design a framework by which to image metallic objects using photoacoustic imaging for diagnostic and therapeutic applications. Current imaging technologies are limited because of metallic susceptibility artifacts, orientation-dependencies or contrast limitations which reduce accurate identification of the implants in tissue. Adoption of a new image technology that could improve recognition would be a step forward for clinical imaging. In the current thesis, a framework is developed on the use of combined ultrasound and photoacoustic imaging for imaging clinical metal implants. Specifically, the following aims will be addressed in order to arrive at a feasible approach for imaging metal with sufficient resolution, contrast, and safety.

1. Ideally, the photoacoustic modality should be able to produce a reasonable contrast signal while maintaining safe laser standards. Furthermore, metal implants can be located up to several centimeters below the tissue surface; therefore, the proper imaging depths must be measured to determine whether or not photoacoustic imaging is suitable for particular applications. Quantitative comparisons with ultrasound imaging must be made in order to obtain a full picture of the specific advantages using photoacoustic imaging in lieu of ultrasound for metal detection. Choosing the correct imaging wavelength(s) is necessary for the best contrast and depth penetration.

2. Filtering techniques must be applied so to preserve resolution and contrast-to-noise, while reducing the presence of image artifacts.
3. Testing on three specific but very different metal implants will be performed to evaluate the appropriateness and relevance of photoacoustic imaging in these applications. Those particular implants are interventional needles, radioactive brachytherapy seeds, and coronary stents. Imaging experiments in ex-vivo tissue environments is necessary.
4. Finally, the sensing/characterization of the surrounding environment will help clinicians verify the correct positioning of metal implant. While accurate visualization of metal implants is necessary for proper guidance, implantation, and monitoring, an additional method to confirm accurate arrival of the metal implant being delivered to a specific region of interest will decrease positioning errors.

Although the proposed study may be useful beyond the specific clinical implants discussed here, the current application is focused on detection monitoring and therapy in the clinical settings where these metal implants are commonly used on patients.

1.6 ORGANIZATION OF THE THESIS

The research work is documented and organized into three sections. SECTION 1 describes the fundamentals of ultrasound and photoacoustic imaging that are necessary for clinical imaging of metal objects (CHAPTER 2). Based on the specific application, an ultrasound transducer that provides the appropriate depth and resolution is necessary.

Photoacoustic imaging will require the choice of a suitable optical window and fluence level to provide the contrast and depth penetration necessary. Furthermore, an overview of spectroscopic imaging will be provided as a framework for enhancing accurate differentiation of endogenous tissue chromophores versus exogenous metal implants.

SECTION 2 will cover specific applications of three metal implants that clinicians could benefit from improved image guidance provided by photoacoustic imaging. Though this selection is not representative of all metal devices implanted in the body, the three choices seen here should provide an overall perspective on the unique challenges of imaging metal devices of various sizes and in different locations of the body.

Interventional needle injections require accurate tracking of the needle to a specific region of interest, such as a tumor or epidural region (CHAPTER 3). Filtering methods to reduce artifacts present in the photoacoustic imaging of needle tracking will be discussed. Results of tissue composition based on photoacoustic signal amplitude will also be presented. Partial results from this study were published: J.L. Su, A.B. Karpiouk, B. Wang, and S.Y. Emelianov, "Photoacoustic imaging of clinical metal needles in tissue", *Journal of Biomedical Optics*, 15, 021309 (2010). Additional results will be submitted as an article for publication.

CHAPTER 4 will cover quantitative analysis of photoacoustic imaging for detection of radioactive brachytherapy seeds for use in prostate therapy. These minute capsules of stainless steel seeds (4.5 x 0.8 mm dimensions) are normally filled with a radioactive isotope, typically iodine-125 or palladium-103. Implantation is performed by injecting

seeds into a cancerous prostate through a patient's perineum by way of metal guide needles according to a pre-established treatment plan. Image guidance is required for accurate seed placement, as these seed positioning errors can result in underdosed treatment regions, requiring post-operative dose corrections that can only be performed through external-beam radiation therapy. Needle deflections of 5° from the insertion angle can decrease the minimum target dose by 10%, thus increasing the tumor-cell survival rate by a factor of 200. Analysis of the US and PA signal dependence to seed orientation was performed, and contrast values were reported demonstrating the benefit of PA over US. Furthermore, depth analyses were reported showing that optical extinction from tissue favors the use of higher wavelengths for increased optical penetration depths. The results from this study were published in: J.L. Su, R.R. Bouchard, A.B. Karpiouk, J.D. Hazle, and S.Y. Emelianov, "Photoacoustic Imaging of Prostate Brachytherapy Seeds", *Biomedical Optics Express,* 2(8), 2243-2254, (2011).

The thesis will then present data on the use of combined intravascular ultrasound and photoacoustic imaging for the visualization of coronary artery stents (CHAPTER 5). This study will show the use of photoacoustic imaging for detecting the apposition of stents deployed in coronary arteries with sufficient resolution and penetration depth to determine the shape and patency of the stent. Spectroscopic imaging can be performed to assess the type of tissue near the stent, as well as the metal stent itself. The results from this study were published in: J.L. Su, B. Wang, S. Emelianov, "Photoacoustic imaging of coronary artery stents" *Optics Express*, 17(22), 19894-19901 (2009).

As each clinical implant has unique applications for imaging, we summarize the results of the overall study in SECTION 3. We will address some of the limitations of the imaging technology, draw conclusions on its utility for clinical applications (CHAPTER 6), and recommend some areas of future work (CHAPTER 7).

1.7 REFERENCES

1. Singh, R. and N.B. Dahotre, *Corrosion degradation and prevention by surface modification of biometallic materials.* J Mater Sci Mater Med, 2007. **18**(5): p. 725-51.

2. Shih, C.-C., C.-M. Shih, Y.-Y. Su, L. Hui, J. Su, M.-S. Chang, and S.-J. Lin, *Effect of surface oxide properties on corrosion resistance of 316L stainless steel for biomedical applications.* Corrosion Science, 2004. **46**(2): p. 427-441.

3. Shih, C.C., C.M. Shih, Y.L. Chen, Y.Y. Su, J.S. Shih, C.F. Kwok, and S.J. Lin, *Growth inhibition of cultured smooth muscle cells by corrosion products of 316 L stainless steel wire.* J Biomed Mater Res, 2001. **57**(2): p. 200-7.

4. Chin, K.J., A. Perlas, V.W. Chan, and R. Brull, *Needle visualization in ultrasound-guided regional anesthesia: challenges and solutions.* Reg Anesth Pain Med, 2008. **33**(6): p. 532-44.

5. Charboneau, J.W., C.C. Reading, and T.J. Welch, *CT and sonographically guided needle biopsy: current techniques and new innovations.* AJR Am J Roentgenol, 1990. **154**(1): p. 1-10.

6. Schafhalter-Zoppoth, I., C.E. McCulloch, and A.T. Gray, *Ultrasound visibility of needles used for regional nerve block: an in vitro study.* Reg Anesth Pain Med, 2004. **29**(5): p. 480-8.

7. Chapman, G.A., D. Johnson, and A.R. Bodenham, *Visualisation of needle position using ultrasonography.* Anaesthesia, 2006. **61**(2): p. 148-58.

8. Abolhassani, N., R.V. Patel, and F. Ayazi, *Minimization of needle deflection in robot-assisted percutaneous therapy.* Int J Med Robot, 2007. **3**(2): p. 140-8.

9. Nath, S., Z. Chen, N. Yue, S. Trumpore, and R. Peschel, *Dosimetric effects of needle divergence in prostate seed implant using 125I and 103Pd radioactive seeds.* Med Phys, 2000. **27**(5): p. 1058-66.

10. Hatada, T., H. Ishii, S. Ichii, K. Okada, and T. Yamamura, *Ultrasound-guided fine-needle aspiration biopsy for breast tumors: needle guide versus freehand technique.* Tumori, 1999. **85**(1): p. 12-4.

11. Phal, P.M., D.M. Brooks, and R. Wolfe, *Sonographically guided biopsy of focal lesions: a comparison of freehand and probe-guided techniques using a phantom.* AJR Am J Roentgenol, 2005. **184**(5): p. 1652-6.

12. Jandzinski, D.I., N. Carson, D. Davis, D.J. Rubens, S.L. Voci, and R.H. Gottlieb, *Treated needles: do they facilitate sonographically guided biopsies?* Journal of ultrasound in medicine : official journal of the American Institute of Ultrasound in Medicine, 2003. **22**(11): p. 1233-7.

13. Hebard, S. and G. Hocking, *Echogenic Technology Can Improve Needle Visibility During Ultrasound-Guided Regional Anesthesia.* Reg Anesth Pain Med, 2011. **36**(2): p. 185-189.

14. Moule, R.N. and P.J. Hoskin, *Non-surgical treatment of localised prostate cancer.* Surg Oncol, 2009.

15. Wei, Z., M. Ding, D. Downey, and A. Fenster, *3D TRUS guided robot assisted prostate brachytherapy.* Med Image Comput Comput Assist Interv Int Conf Med Image Comput Comput Assist Interv, 2005. **8**(Pt 2): p. 17-24.

16. Morooka, M., K. Kubota, Y. Kono, K. Ito, K. Kurihara, T. Mitsumoto, T. Sato, Y. Oshiro, T. Aruga, K. Hasuo, M. Kanemura, and S. Minowada, *Scintigraphic detection of I-125 seeds migration after permanent brachytherapy for prostate cancer: how far do seeds travel?* Clin Nucl Med, 2009. **34**(7): p. 466-9.

17. Merrick, G.S., W.M. Butler, A.T. Dorsey, J.H. Lief, and M.L. Benson, *Seed fixity in the prostate/periprostatic region following brachytherapy.* Int J Radiat Oncol Biol Phys, 2000. **46**(1): p. 215-20.

18. Nguyen, B.D., S.E. Schild, W.W. Wong, and S.A. Vora, *Prostate brachytherapy seed embolization to the right renal artery.* Brachytherapy, 2009.

19. Maintz, D., R.M. Botnar, R. Fischbach, W. Heindel, W.J. Manning, and M. Stuber, *Coronary magnetic resonance angiography for assessment of the stent lumen: a phantom study.* J Cardiovasc Magn Reson, 2002. **4**(3): p. 359-67.

20. Costa, M.A. and D.I. Simon, *Molecular basis of restenosis and drug-eluting stents.* Circulation, 2005. **111**(17): p. 2257-73.

21. Barash, P. and S. Akhtar, *Coronary stents: factors contributing to perioperative major adverse cardiovascular events.* British journal of anaesthesia, 2010. **105 Suppl 1**: p. i3-15.

22. Elgort, D.R., C.M. Hillenbrand, S. Zhang, E.Y. Wong, S. Rafie, J.S. Lewin, and J.L. Duerk, *Image-guided and -monitored renal artery stenting using only MRI.* J Magn Reson Imaging, 2006. **23**(5): p. 619-27.

23. Hug, J., E. Nagel, A. Bornstedt, B. Schnackenburg, H. Oswald, and E. Fleck, *Coronary arterial stents: safety and artifacts during MR imaging.* Radiology, 2000. **216**(3): p. 781-7.

24. Maintz, D., K.U. Juergens, T. Wichter, M. Grude, W. Heindel, and R. Fischbach, *Imaging of coronary artery stents using multislice computed tomography: in vitro evaluation.* Eur Radiol, 2003. **13**(4): p. 830-5.

25. Kawase, Y., K. Hoshino, R. Yoneyama, J. McGregor, R.J. Hajjar, I.K. Jang, and M. Hayase, *In vivo volumetric analysis of coronary stent using optical coherence tomography with a novel balloon occlusion-flushing catheter: a comparison with intravascular ultrasound.* Ultrasound Med Biol, 2005. **31**(10): p. 1343-9.

26. Mintz, G.S., S.E. Nissen, W.D. Anderson, S.R. Bailey, R. Erbel, P.J. Fitzgerald, F.J. Pinto, K. Rosenfield, R.J. Siegel, E.M. Tuzcu, and P.G. Yock, *American College of Cardiology Clinical Expert Consensus Document on Standards for Acquisition, Measurement and Reporting of Intravascular Ultrasound Studies (IVUS). A report of the American College of Cardiology Task Force on Clinical Expert Consensus Documents.* J Am Coll Cardiol, 2001. **37**(5): p. 1478-92.

27. Barlis, P., K. Dimopoulos, J. Tanigawa, E. Dzielicka, G. Ferrante, F. Del Furia, and C. Di Mario, *Quantitative analysis of intracoronary optical coherence tomography measurements of stent strut apposition and tissue coverage.* Int J Cardiol, 2009.

28. Slottow, T.L., R. Pakala, T. Okabe, D. Hellinga, R.J. Lovec, F.O. Tio, A.B. Bui, and R. Waksman, *Optical coherence tomography and intravascular ultrasound imaging of bioabsorbable magnesium stent degradation in porcine coronary arteries.* Cardiovasc Revasc Med, 2008. **9**(4): p. 248-54.

29. Jang, I.K., B.E. Bouma, D.H. Kang, S.J. Park, S.W. Park, K.B. Seung, K.B. Choi, M. Shishkov, K. Schlendorf, E. Pomerantsev, S.L. Houser, H.T. Aretz, and G.J. Tearney, *Visualization of coronary atherosclerotic plaques in patients using optical coherence tomography: comparison with intravascular ultrasound.* J Am Coll Cardiol, 2002. **39**(4): p. 604-9.

30. Ziskin, M.C., D.I. Thickman, N.J. Goldenberg, M.S. Lapayowker, and J.M. Becker, *The comet tail artifact.* J Ultrasound Med, 1982. **1**(1): p. 1-7.

31. Gronningsaeter, A., T. Lie, K. Bolz, and A. Heimdal, *Ultrasonographic stent-imaging artifacts.* Journal of Vascular Investigation, 1995. **3**: p. 140-149.

32. Kruger, R.A., *Photoacoustic ultrasound.* Med Phys, 1994. **21**(1): p. 127-31.

33. Andreev, V.G., A.A. Karabutov, and A.A. Oraevsky, *Detection of ultrawide-band ultrasound pulses in optoacoustic tomography.* IEEE Trans Ultrason Ferroelectr Freq Control, 2003. **50**(10): p. 1383-90.

34. Kruger, R.A., P. Liu, Y.R. Fang, and C.R. Appledorn, *Photoacoustic ultrasound (PAUS)--reconstruction tomography.* Med Phys, 1995. **22**(10): p. 1605-9.

35. Wang, X., Y. Xu, M. Xu, S. Yokoo, E.S. Fry, and L.V. Wang, *Photoacoustic tomography of biological tissues with high cross-section resolution: reconstruction and experiment.* Med Phys, 2002. **29**(12): p. 2799-805.

36. Faraggi, E., S. Wang, and B. Gerstman. *Stress confinement, shock wave formation, and laser-induced damage*. in *Optical Interactions with Tissue and Cells XVI* 2005. San Jose, CA, USA

37. Karlsson, B. and C.G. Ribbing, *Optical constants and spectral selectivity of stainless steel and its oxides* J. Appl. Phys., 1982. **53**(9): p. 6340-6346.

38. Prahl, S.A. *Optical properties spectra compiled by Scott Prahl*. 2001 July 1, 2010]; Available from: http://omlc.ogi.edu/spectra/.

39. Su, J.L., A.B. Karpiouk, B. Wang, and S.Y. Emelianov, *Photoacoustic imaging of clinical metal needles in tissue.* Journal of Biomedical Optics, 2010. **15**(2): p. 021309-6.

40. Mallidi, S., T. Larson, J. Tam, P.P. Joshi, A. Karpiouk, K. Sokolov, and S. Emelianov, *Multiwavelength photoacoustic imaging and plasmon resonance coupling of gold nanoparticles for selective detection of cancer.* Nano Lett, 2009. **9**(8): p. 2825-31.

41. Ku, G. and L.V. Wang, *Deeply penetrating photoacoustic tomography in biological tissues enhanced with an optical contrast agent.* Opt Lett, 2005. **30**(5): p. 507-9.

42. Oraevsky, A.A. and A.A. Karabutov, *Optoacoustic tomography*2003: CRC Press.

43. Shah, J., S. Park, S. Aglyamov, T. Larson, L. Ma, K. Sokolov, K. Johnston, T. Milner, and S.Y. Emelianov, *Photoacoustic imaging and temperature measurement for photothermal cancer therapy.* J Biomed Opt, 2008. **13**(3): p. 034024.

44. Chen, Y.S., W. Frey, S. Kim, P. Kruizinga, K. Homan, and S. Emelianov, *Silica-coated gold nanorods as photoacoustic signal nanoamplifiers.* Nano Letters, 2011. **11**(2): p. 348-54.

45. Chen, Y.S., W. Frey, S. Kim, K. Homan, P. Kruizinga, K. Sokolov, and S. Emelianov, *Enhanced thermal stability of silica-coated gold nanorods for photoacoustic imaging and image-guided therapy.* Optics express, 2010. **18**(9): p. 8867-78.

46. Gonzalez, M.G., X. Liu, R. Niessner, and C. Haisch, *Strong size-dependent photoacoustic effect on gold nanoparticles by laser-induced nanobubbles.* Applied Physics Letters, 2010. **96**(17): p. 174104.

47. Gusev, V.E. and A.A. Karabutov, *Laser Optoacoustics*1993, New York: American Institute of Physics. 336.

48. Cox, B., J. Laufer, and P. Beard. *The challenges for quantitative photoacoustic imaging*. in *Proceedings of SPIE Vol. 7177*. 2009.

49. Laufer, J., D. Delpy, C. Elwell, and P. Beard, *Quantitative spatially resolved measurement of tissue chromophore concentrations using photoacoustic spectroscopy: application to the measurement of blood oxygenation and haemoglobin concentration.* Physics in medicine and biology, 2007. **52**(1): p. 141-68.

50. Wang, B., J.L. Su, J. Amirian, S.H. Litovsky, R. Smalling, and S. Emelianov, *Detection of lipid in atherosclerotic vessels using ultrasound-guided spectroscopic intravascular photoacoustic imaging.* Optics express, 2010. **18**(5): p. 4889-97.

Chapter 2: Photoacoustic Fundamentals for Imaging Metal

2.1 INTRODUCTION

The fundamentals of the photoacoustic effect recall back to the early 1880's when Alexander Graham Bell presented the results of his "photophone" to the American Association for the Advancement of Science [1]. Bell made the observation that modulated sunlight incident on a thin metal disc could be transformed into a sound wave, detectable by the human ear. The underlying physics of photoacoustic imaging have remained the same since then, though the use of sunlight has been replaced with high powered pulsatile lasers, and the use of the human ear has been replaced by sensitive ultrasonic detectors.

Biomedical applications of the photoacoustic effect did not appear until the mid-1990s when the use of photoacoustic signals as an imaging and sensing technique began to surface [2, 3]. Then, around the beginning of the 2000s, researchers began recognizing the clinical applications of photoacoustic technology. Since physiological and pathological changes often alter tissue composition and associated optical absorption, the magnitude of the received photoacoustic signal can reveal different characteristics of living tissue. Research in photoacoustic imaging and sensing has gained tremendous traction in the development areas of systems development, image-reconstruction algorithms, signal processing algorithms, contrast agent developments and basic biological applications. Many imaging applications have taken advantage of the strong potential of photoacoustic imaging from detection of cancer [4, 5] to diagnosis of

vulnerable atherosclerotic plaques [6, 7]. Since image contrast is obtained from the optical absorption property, imaging can be performed using endogenous or exogenous contrast. The primary endogenous optical absorber in tissue in the near infrared spectrum is hemoglobin. The absorption coefficient of hemoglobin is several orders of magnitude greater than the absorption of surrounding tissues [8]. *In vivo* photoacoustic imaging of blood content [9] has been used to monitor tumor angiogenesis, vasa vasorum in atheroscelerotic plaques, blood oxygenation [10], functional brain mapping [11], and also skin melanoma detection [12]. In other wavelengths, optical absorption of other tissue components (such as lipids) may dominate which assists in the differentiation of various tissue types [7, 13]. To further improve photoacoustic contrast, various exogenous contrast agents exist to provide targeted contrast to specific regions. These contrast agents include the use of dyes [9, 14], nanoparticles [5, 15] or other absorbers [16] targeted to various biomarkers to investigate a particular phenomenon.

2.2 PHOTOACOUSTIC FUNDAMENTALS

2.2.1. The Photoacoustic Signal

As previously stated in Chapter 1, the photoacoustic effect is produced by irradiating tissue with a pulsed nanosecond laser, although other timescale pulses have been implemented. Laser energy absorbed by the tissue results in a brief temperature rise and localized thermoelastic expansion within the tissue. The temperature relaxation following this expansion results in the emission of a broadband ultrasonic wave which is detectable using standard ultrasound transducers (Fig 2.1). Similar to ultrasound, a spatial

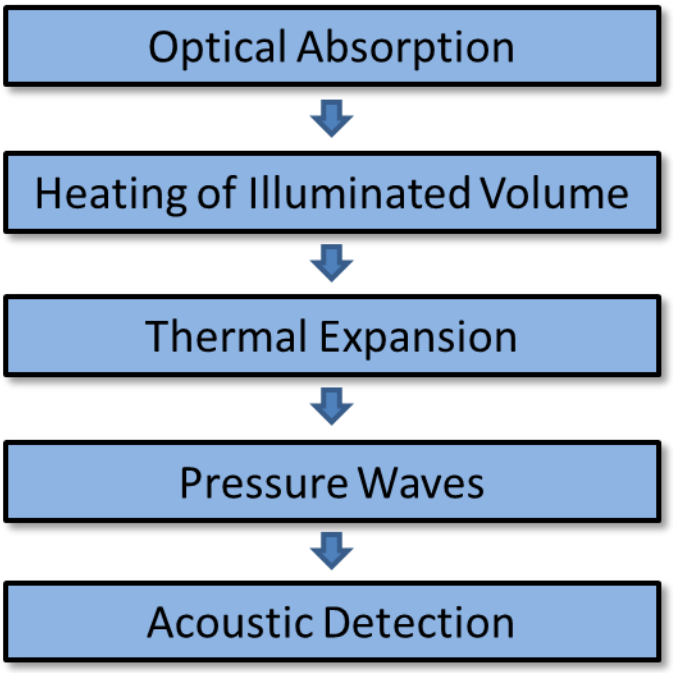

Figure 2.1. Evaluation of the photoacoustic signal.

image can be formed by measuring the time-of-flight of the acoustic pulses and knowing the speed of sound in the probed tissue region. Two-dimensional images or 3D tomographic images can be constructed depending on the scan parameters used in data acquisition. The initial pressure produced is found to be dependent on the optical absorption coefficient, μ_a, the localized laser fluence, Φ, and the Grüneisen coefficient, Γ, of the surrounding environment, as previously seen in Equation 1.1. Though one may assume that the photoacoustic signal is linearly proportional to the optical absorption of the tissue, writing Equation 1.1 in an explicit manner shows that this assumption is not necessarily true:

$$P_0 = \mu_a(r) \cdot \Phi(r;\, \mu_a, \mu_s, g) \cdot \frac{\beta \cdot c^2}{C_p} \qquad \textit{(Eq. 2.1)}$$

Equation 2.1 reveals that the optical absorption is related to the depth of the tissue sample, and its value also affects the local fluence at a specific depth along with optical scattering, and the anisotropy value, *g*. Furthermore, recent findings have suggested that the environmental contribution to the photoacoustic signal may be more significant than what was previously understood [17, 18] from the Grüneisen coefficient. The inter-dependence of optical parameters in tissue can make it difficult to accurately calculate quantitative values such as optical absorption or local fluence from the initial photoacoustic pressure. Despite these challenges, several research groups have attempted to indirectly measure optical absorption properties by examining the photoacoustic signal amplitude.

2.2.2. Spectroscopic Photoacoustic Imaging

Tissue composition can be derived from the variation in optical absorption coefficients. Since most tissue chromophores contain low optical absorption coefficients, multi-wavelength or spectroscopic photoacoustic imaging is necessary to detect and differentiate between endogenous contrast agents. By acquiring images at multiple wavelengths and then processing the data through a spectroscopic analysis, quantitative measurements regarding the absolute concentration of specific chromophores can be obtained. Spectroscopic PA imaging has been used to detect functional information such as oxygen saturation in blood vessels and tumor regions with laser wavelengths in the NIR region [19]. PA imaging in the range of 1210 nm has been shown to provide contrast for lipid composition in atherosclerotic plaques [13]. With a priori knowledge of the spectral differences between various chromophores, it is possible to quantify the concentrations of these constituents across a wide range of optical wavelengths. In addition to characterizing endogenous chromophore concentrations, spectroscopic imaging techniques can also be used to detect the presence of metal based on the unique spectra found in stainless steel (Fig 1.1).

As previously stated, one of the main challenges in spectroscopic PA imaging is that the optical properties of tissue are unknown, which can greatly affect laser fluence compensation for quantitative measurements [19, 20]. Without prior knowledge of the tissue properties through which the light passes, imaging in a small wavelength range (i.e. tens of nm) can reduce errors in the reconstruction process [20]. Another strategy to

overcome errors uses inverse algorithms to estimate both the ultrasonic measurement and the photoacoustic image reconstruction [21-23].

2.2.3 Ultrasound and Photoacoustic Imaging of Metal Objects

Currently, imaging of metal objects is performed primarily using ultrasound imaging. Metal is a strong reflector both acoustically and optically. The acoustic reflective property of metal is well-suited for ultrasound imaging. Acoustic pulses incident on a flat metal surface are reflected in a coherent manner provided that the dimension of the metal surface is large compared to the wavelength of sound. Given that ultrasound operates at frequencies of 5 MHz or higher, the surfaces of most medical metal devices fall under this category. These acoustic specular reflections are highly directional, and metal surfaces that are not parallel to the transducer face may reflect acoustic beams away from the transducer, rendering the metal invisible under ultrasound [24]. An ultrasound artifact that is produced despite the metal rendered invisible is an acoustic shadow that appears distal to the metal surface. This shadow appears as a dark hypoechoic region resulting from the acoustic beam unable to penetrate the metal surface and scatter through the distal lying tissue. Trained clinicians can use this acoustic shadow to recognize the presence, but not the precise location, of the metal implant in question.

The use of photoacoustic imaging is advantageous for visualization of metal implants in tissue. In general, metals have a high optical absorption coefficient due to the photoelectric effect (Fig 2.2) [25]. Though metal is usually thought of as being highly reflective, a small amount of light energy can be absorbed by electrons near the metal's

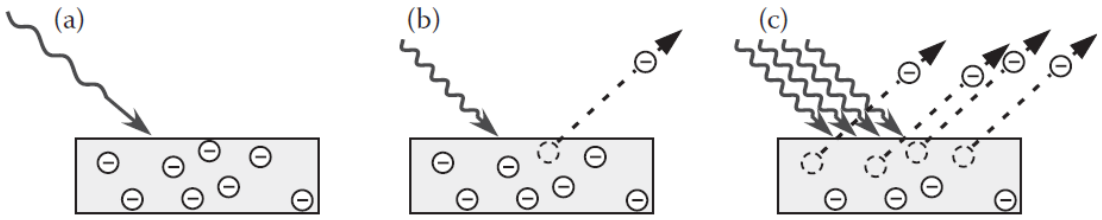

Figure 2.2 Illustration demonstrating the photoelectric effect resulting from photons incident on a metal surface. Adapted from [25]. (a) Low energy photons hitting a metal surface do not contain enough energy to dislodge electrons. While the majority of photons are reflected away, electrons can still absorb energy from photons contributing to localized thermal expansion. (b) A photon with a high enough frequency has enough energy to eject an electron from the metal surface. (c) With a high enough frequency of light, increasing the number of incident photons will increase the number of ejected electrons. The photoacoustic signal for imaging of metal implants, energy absorption mainly arises from the effect seen in (a).

surface. Individual photons incident on a metal surface can excite individual electrons. The effect is considered an all-or-nothing event. Photons that do not transfer their energy to electrons are reflected away. However, if the photon is successful in transferring its energy to the electron, it is considered to be absorbed. In metals, the densely packed electrons contribute to the increased probability of the energy transfer occurrence. The amount of energy required for absorption to take place is equal to the energy necessary to excite an electron to a higher-energy band, or exceed the ionization energy necessary to allow the electron to escape the atom. The minimum frequency required for light to eject an electron is known to be (through Planck's constant, h):

$$f = \frac{\varepsilon_{threshhold}}{h} \qquad (Eq.\ 2.2)$$

The energy thresholds in metal usually require light frequencies to be in the UV range to forcibly expel electrons. At lower energy thresholds (lower light frequencies) though, electrons are not expelled, but can still absorb energy. The electrons in metal are not confined as in other non-conducting solids, but rather are modeled as non-interacting free electrons that move through a crystal lattice. Absorption of photon energy by an electron can promote the individual electron to higher energy bands resulting in large kinetic oscillations within the electron cloud. The electrons in metals are much more delocalized than electrons in organic tissue constituents, thereby absorbing more energy from incident photons. In agreement with the described phenomena, the optical absorption spectrum of 316L stainless steel (Fig. 1.1) does offer a 3-4 order of magnitude increase (cm^{-1}) over endogenous tissue in optical absorption in the NIR wavelength range.

Thus, the irradiated area of the metal becomes an acoustic source when excited by the photoacoustic effect. Generally, the photoacoustic signal that arises from irradiating metal with a pulsed laser occurs omni-directionally from the target given that the spot size of irradiation is large compared to the total size of the metal object. When the metal object is evenly irradiated, acoustic energy will radiate omni-directionally from the region, allowing a greater freedom in placing the acoustic transducer position to detect the photoacoustic signal. However, in instances where the focused laser source is only incident on a small region, directional effects will apply. In the latter case, only a transducer that is located normal to the metal surface region will detect photoacoustic signals. The scenario of uniform light irradiation is more likely to be found in-vivo where the optical scattering properties of tissue provide beam spreading of the laser pulse, thereby diffusing the light and essentially "bathing" the metal implant with diffuse light in all directions.

2.3 ULTRASOUND TRANSDUCERS

In photoacoustic imaging, the acoustic signal is usually received using a standard commercial ultrasound transducer. This is a convenient and relatively inexpensive way to implement photoacoustic imaging using currently available technology. One should note that photoacoustic signals are broadband signals; however, ultrasound transducers are usually narrowbanded, only receiving a small fraction of the frequency content produced in the thermal elastic expansion and relaxation. The ultrasound transducers used depend on the in-vivo environment in which imaging will take place. For example, intravascular

imaging applications for imaging stents require a different resolution and penetration depth than an external ultrasound handheld array used for imaging needles inserted several cm through skin. Further details of transducer choices will be discussed in each chapter (CHAPTERS 3-5) as it relates to the image parameters needed in each unique imaging application.

One limitation in utilizing ultrasound transducers is the fact that most ultrasound transducers are narrow-banded in their detection frequency. The photoacoustic signal is usually wide-banded from several MHz to several tens of MHz. The lack of frequency detection for photoacoustics can reduce the resulting image quality, both in SNR and spatial resolution. Therefore, selection of the appropriate transducer with respect to center frequency is then a necessary criterion to consider when designing a photoacoustic system. Trade-offs between resolution and depth penetration must be taken into account when selecting the ultrasound transducer.

2.4 OPTIMAL WAVELENGTH CHOICES

In photoacoustic imaging, laser wavelengths in the near-infrared (NIR) region are usually employed. At this wavelength range, light penetrates deeply, and many tissue chromophores have unique absorption spectra which allows for differentiation based on photoacoustic amplitude. Though one might assume that the highest photoacoustic contrast will occur at the wavelength optical absorption peak, equation 2.1 shows that this is not necessarily true. For imaging of metal implants, Figure 1.1 shows that metal has higher absorption at wavelengths around 700-750 nm. However, at deeper tissue depths,

the laser fluence is reduced due to the high extinction coefficient of tissue at these wavelengths. In general, light penetrates deeper at longer wavelengths, and therefore, more optimal imaging wavelengths may occur at frequencies such as 1064 nm or higher [26]. Absorption of tissue is decreased at longer wavelengths, which could be used to minimize signal from background tissue. The selection of optimal wavelength(s) must take into account parameters such as optical absorption of imaging constituents, depth penetration, and required resolution for imaging.

For spectroscopic imaging, as discussed in section 2.2.2, the optimal wavelength range will depend on the tissue constituent being imaged. For example, for spectroscopically imaging deoxygenated blood, one might choose a wavelength range around 780 nm where a small absorption peak occurs, differentiating deoxygenated blood from oxygenated blood. The optical absorption spectra of metal is also unique from tissue, and could be used to further differentiate metal objects from tissue or other image artifacts in photoacoustic images. Imaging across a range of wavelengths may allow for better differentiation of metal implants, but must be done with appropriate information of the imaging environment, as tissue properties can change dramatically thereby affecting the received photoacoustic signal from the transducer [22].

2.5 Laser Repetition Rates

The time required to obtain photoacoustic images is usually limited by the pulse repetition rate of the laser, and the sequential nature of the detection scheme. Many tunable pulsed OPO lasers operate at 10 Hz, which prevent the use of real-time

photoacoustic imaging. In limited applications where single element ultrasound transducers are used, such as in photoacoustic microscopy or intravascular applications, this is a further restriction as each A-line requires one individual pulse. Therefore, laser faster repetition rates are necessary for these applications.

2.6 Photoacoustic Characterization of Metal Implants

Recent studies suggest that there exists an environmental contribution to the photoacoustic signal that may be more significant than what was previously understood [17, 18]. According to Equation 1.1, the produced photoacoustic amplitude is linearly dependent on the Grüneisen coefficient, Γ: a dimensionless parameter that describes the thermoelastic properties of the medium surrounding the photoacoustic absorber. Studies suggest that photoacoustic contrast arises from the heat flux out of the absorber over a short time scale following a fast and large deposition of heat [27, 28]. The Grüneisen coefficient is often-times assumed to be uniform across tissue especially for quantitative measurements. However, this uniformity is not necessarily the case, and in reality can vary widely between different tissue types [29]. For example, the Grüneisen coefficient in fat is approximately 0.7 to 0.9, while the Grüneisen value of blood is around 0.25. Therefore, the photoacoustic amplitude can be greatly influenced by the surrounding environment.

It is generally accepted that the environmental boundary directly adjacent to the absorber is a primary contributor to the resulting PA signal due to heat dissipation [28, 30, 31]. Therefore, the effect of the environment on the PA signal may play an important

role in characterizing the tissue in which a metal implant is inserted into. In the above example, a needle surrounded by fat ($\Gamma \approx 0.7$) could theoretically produce a PA signal amplitude around 300% more than a needle that is surrounded by blood ($\Gamma \approx 0.25$) given that other parameters remained constant. Analysis of the signal amplitude could then confirm arrival of a metal implant into either a fat-based or blood-based region of interest. A lookup table would be required to evaluate the differences in signal amplitude, as well as an accurate method to compensate for laser fluence attenuation. Another hypothetical situation could exist in which PA imaging of a metal object could determine whether the metal was adjacent to vulnerable plaques or stable lesions. Overall, a proper understanding of the generation of photoacoustic pressure is necessary to guide the application of the imaging of metal implants. From a theoretical standpoint, any quantitative application of photoacoustic imaging cannot occur simply under the assumption that the received signal is only proportional to the optical absorption of the local region of interest.

2.7 REFERENCES

1. Bell, A.G., *On the production and reproduction of sound by light.* American Journal of Science, 1880. **20**(305-324).

2. Kruger, R.A., *Photoacoustic ultrasound.* Medical physics, 1994. **21**(1): p. 127-31.

3. Hoelen, C.G., F.F. de Mul, R. Pongers, and A. Dekker, *Three-dimensional photoacoustic imaging of blood vessels in tissue.* Optics letters, 1998. **23**(8): p. 648-50.

4. Mallidi, S. and S. Emelianov, *Photoacoustic technique to measure beam profile of pulsed laser systems.* Rev Sci Instrum, 2009. **80**(5): p. 054901.

5. Shah, J., S. Park, S. Aglyamov, T. Larson, L. Ma, K. Sokolov, K. Johnston, T. Milner, and S.Y. Emelianov, *Photoacoustic imaging and temperature measurement for photothermal cancer therapy.* J Biomed Opt, 2008. **13**(3): p. 034024.

6. Sethuraman, S., J.H. Amirian, S.H. Litovsky, R.W. Smalling, and S.Y. Emelianov, *Ex vivo Characterization of Atherosclerosis using Intravascular Photoacoustic Imaging.* Opt Express, 2007. **15**(25): p. 16657-66.

7. Sethuraman, S., J.H. Amirian, S.H. Litovsky, R.W. Smalling, and S.Y. Emelianov, *Spectroscopic intravascular photoacoustic imaging to differentiate atherosclerotic plaques.* Opt Express, 2008. **16**(5): p. 3362-7.

8. Prahl, S.A. *Optical properties spectra compiled by Scott Prahl*. 2001 July 1, 2010]; Available from: http://omlc.ogi.edu/spectra/.

9. Hu, S. and L.V. Wang, *Photoacoustic imaging and characterization of the microvasculature.* Journal of Biomedical Optics, 2010. **15**(1): p. 011101-15.

10. Laufer, J.G., C.E. Elwell, D.T. Delpy, and C.C. Beard, *Spatially resolved blood oxygenation measurements using time-resolved photoacoustic spectroscopy.* Adv Exp Med Biol, 2006. **578**: p. 155-60.

11. Stein, E.W., K. Maslov, and L.V. Wang, *Noninvasive, in vivo imaging of blood-oxygenation dynamics within the mouse brain using photoacoustic microscopy.* J Biomed Opt, 2009. **14**(2): p. 020502.

12. Oh, J.T., M.L. Li, H.F. Zhang, K. Maslov, G. Stoica, and L.V. Wang, *Three-dimensional imaging of skin melanoma in vivo by dual-wavelength photoacoustic microscopy.* J Biomed Opt, 2006. **11**(3): p. 34032.

13. Wang, B., J.L. Su, J. Amirian, S.H. Litovsky, R. Smalling, and S. Emelianov, *Detection of lipid in atherosclerotic vessels using ultrasound-guided spectroscopic intravascular photoacoustic imaging.* Optics express, 2010. **18**(5): p. 4889-97.

14. McDonald, M.A., L. Jankovic, K. Shahzad, M. Burcher, and K.C. Li, *Acoustic fingerprints of dye-labeled protein submicrosphere photoacoustic contrast agents.* J Biomed Opt, 2009. **14**(3): p. 034032.

15. Li, P.C., C.W. Wei, C.K. Liao, C.D. Chen, K.C. Pao, C.R. Wang, Y.N. Wu, and D.B. Shieh, *Photoacoustic imaging of multiple targets using gold nanorods.* IEEE Trans Ultrason Ferroelectr Freq Control, 2007. **54**(8): p. 1642-7.

16. Shashkov, E.V., M. Everts, E.I. Galanzha, and V.P. Zharov, *Quantum dots as multimodal photoacoustic and photothermal contrast agents.* Nano Lett, 2008. **8**(11): p. 3953-8.

17. Chen, Y.S., W. Frey, S. Kim, K. Homan, P. Kruizinga, K. Sokolov, and S. Emelianov, *Enhanced thermal stability of silica-coated gold nanorods for photoacoustic imaging and image-guided therapy.* Optics express, 2010. **18**(9): p. 8867-78.

18. Chen, Y.S., W. Frey, S. Kim, P. Kruizinga, K. Homan, and S. Emelianov, *Silica-coated gold nanorods as photoacoustic signal nanoamplifiers.* Nano Letters, 2011. **11**(2): p. 348-54.

19. Laufer, J., D. Delpy, C. Elwell, and P. Beard, *Quantitative spatially resolved measurement of tissue chromophore concentrations using photoacoustic spectroscopy: application to the measurement of blood oxygenation and haemoglobin concentration.* Physics in medicine and biology, 2007. **52**(1): p. 141-68.

20. Maslov, K., H.F. Zhang, and L.H. Wang, *Effects of wavelength-dependent fluence attenuation on the noninvasive photoacoustic imaging of hemoglobin oxygen saturation in subcutaneous vasculature in vivo.* Inverse Problems, 2007. **23**(6): p. S113-S122.

21. Xu, M. and L.V. Wang, *Photoacoustic imaging in biomedicine.* Review of Scientific Instruments, 2006. **77**(4): p. 041101-22.

22. Cox, B.T., S.R. Arridge, and P.C. Beard, *Estimating chromophore distributions from multiwavelength photoacoustic images.* J Opt Soc Am A Opt Image Sci Vis, 2009. **26**(2): p. 443-55.

23. Modgil, D., M.A. Anastasio, and P.J.L. Riviere, *Image reconstruction in photoacoustic tomography with variable speed of sound using a higher-order geometrical acoustics approximation.* Journal of Biomedical Optics, 2010. **15**(2): p. 021308.

24. Chapman, G.A., D. Johnson, and A.R. Bodenham, *Visualisation of needle position using ultrasonography.* Anaesthesia, 2006. **61**(2): p. 148-58.

25. Raymer, M.G., *The silicon web : physics for the Internet age*2009, New York: Taylor & Francis. xxv, 571 p.

26. Homan, K., S. Kim, Y.S. Chen, B. Wang, S. Mallidi, and S. Emelianov, *Prospects of molecular photoacoustic imaging at 1064 nm wavelength.* Optics letters, 2010. **35**(15): p. 2663-5.

27. Diebold, G.J., A.C. Beveridge, and T.J. Hamilton, *The photoacoustic effect generated by an incompressible sphere.* The Journal of the Acoustical Society of America, 2002. **112**(5 Pt 1): p. 1780-6.

28. Oraevsky, A.A., A.A. Karabutov, and E.V. Savateeva, *Enhancement of optoacoustic tissue contrast with absorbing nanoparticles.* Proc. SPIE, 2001. **4434**: p. 60-69.

29. Cox, B., J. Laufer, and P. Beard. *The challenges for quantitative photoacoustic imaging*. in *Proceedings of SPIE Vol. 7177*. 2009.

30. Gusev, V.E. and A.A. Karabutov, *Laser Optoacoustics*1993, New York: American Institute of Physics. 336.

31. Calasso, I.G., W. Craig, and G.J. Diebold, *Photoacoustic Point Source.* Physical Review Letters, 2001. **86**(16): p. 3550-3553.

Chapter 3: Photoacoustic imaging for needle guided interventions

3.1 Introduction

A wide variety of metal implants are used clinically within the human body. These range from permanently implanted metals such as orthopedic replacements or coronary arterial stents, and include temporarily implanted metals such as surgical staples. Hypodermic needles are one such temporary metal implant used for a wide variety of clinical applications. Metal needles are commonly used for localized drug delivery, such as in cancer therapy, or for tissue collection in needle aspiration biopsies [1]. In either case, the ability to visualize both the anatomical surrounding structures and the advancing needle tip is required [2]. Accurate imaging is necessary to guide the needle to the targeted location [3]. Needle deflection and deformation can occur when inserting needles into soft, non-homogeneous tissues [4] which can affect the localized accuracy of insertion [5]. Currently, the most commonly used clinical strategy to visualize the direction of the needle shaft in real-time is ultrasound-guidance [1]. However, the needle tip can oftentimes be visualized better than the needle shaft because of the irregular surface of the machine cut bevel which scatters the ultrasound (US) beam in all directions, reflecting the beam in part back to the transducer [2]. However, visibility of the tip alone is not sufficient for the clinician to gauge the insertion angle of the needle. Visibility of the needle shaft is dependent on the angle of the needle relative to the transducer [6] and is best visualized only when perpendicular and in the plane of the ultrasound transducer. Needle deflections away from the transducer of only a few degrees

are usually enough to conceal the US signal from the needle. To overcome these issues, mechanical or optical needle guides are often used to keep the needle in the transducer plane [7, 8]. However, these guides restrict needle movement when fine adjustments are needed by medical operators; therefore, many clinicians prefer using a freehand technique during needle insertion and injection [3].

US imaging of metal needles can produce an unexpected echographic pattern resembling the shape of a comet tail [9]. The pattern is due to reverberations within the needle and is dependent on the acoustic impedance mismatch between the needle and its surroundings. In fact, these artifacts are present in ultrasound imaging of any metallic object [10]. While these artifacts can be helpful in determining the presence of foreign metal in-vivo, the existence of the comet tail pattern prevents visibility of objects directly below and adjacent to the needle [11]. This effect can detrimentally affect the ability to determine needle position relative to the background tissue.

In this paper, we demonstrate the ability of combined ultrasound (US) and photoacoustic (PA) imaging to visualize metal needles inserted into tissue. Briefly, the PA effect results from irradiating an object with a pulsed laser beam in order to produce a thermoacoustic response. Light absorbed in a specific local region is converted into heat, and then converted into pressure due to the thermoelastic expansion of the object. An ultrasound transducer detects the produced pressure, which is linearly related to the optical absorption coefficient, μ_a and the localized laser fluence. Since metal is generally highly absorbing, relative to endogenous tissue chromophores, the PA signal from metal

objects should be much higher relative to the background tissue within a given wavelength. Experiments were performed using common commercially available clinical metal needles inserted into tissue and tissue-mimicking phantoms. The presence of these clinical needles was detected using combined US and PA imaging. In each experiment, the acquired PA images outlined the presence of the metal implant, and the US image provided morphological information about the surrounding structure. During post-processing, the comet tail artifacts were reduced using a filtering approach thus allowing the previously distracted background in photoacoustic imaging to be better visualized. Using both US and PA imaging allowed for accurate measurements of the needle's position within the tissue. The accuracy of these measurements demonstrates the usefulness of photoacoustic imaging in visualizing metal needles and other metal implants in-vivo.

3.2 METHODS AND MATERIALS

To test the feasibility of US and PA to image metal needles in tissue, imaging studies were conducted using different sizes of needles. In the first experiment, a Cortex ultrasound imaging system (Winprobe Corporation, North Palm Beach, FL) was used for RF data acquisition (Fig 3.1). This ultrasound system was interfaced with a 7 MHz center frequency, 14 mm wide, 128 element linear array transducer to image the needles. An Nd:YAG pump laser output (Vibrant B, Opotek, Inc., Carlsbad, CA) at 1064 nm was used to optically illuminate the tissue phantom. Laser fluence in all experiments was measured to be approximately 10 mJ/cm^2. Laser light was delivered through an 18-

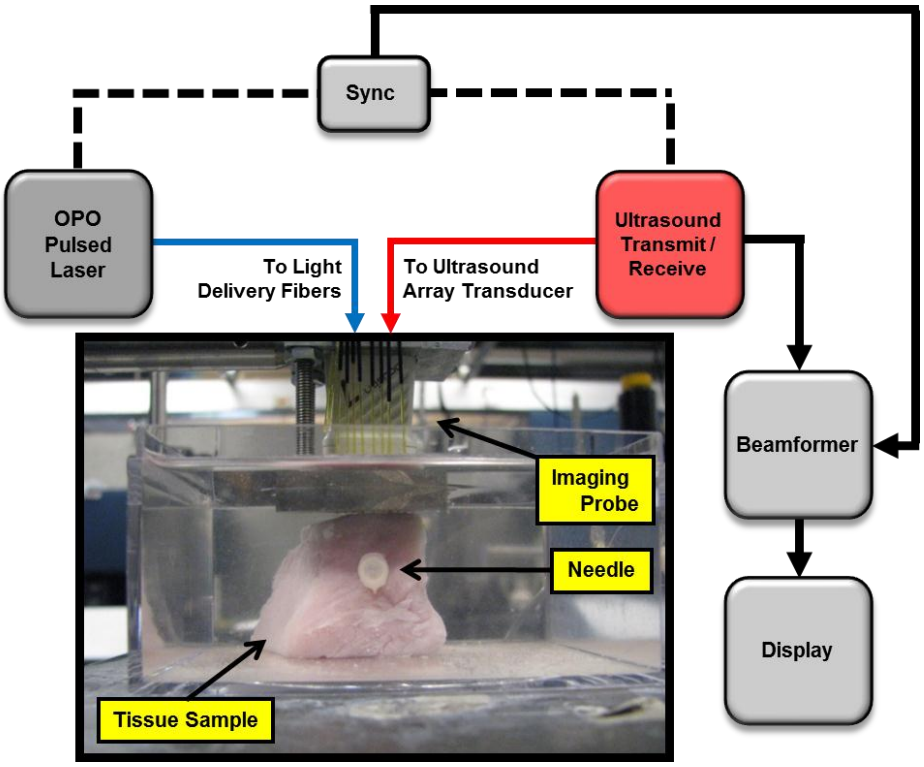

Figure 3.1: Experimental setup for imaging of metal needles in a porcine tissue sample. An imaging probe consisting of a 7 MHz linear array transducer and an 18-fiber bundle was positioned on the top of the sample. The pork sample was placed in a water tank for the purposes of acoustic coupling. The sample was irradiated at 1064 nm wavelength. Laser fluence was approximately 10 mJ/cm^2.

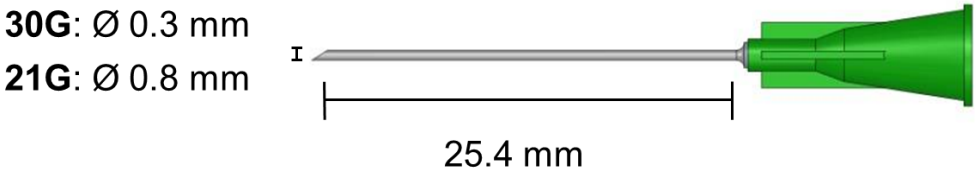

Figure 3.2: Schematic view of the 30-gauge (30G) and 21-gauge (21G) needles. The 30G needle was inserted into pork loin tissue perpendicular, and later re-inserted at an angle of approximately 15° to the surface of the ultrasound transducer. The 21G needles were inserted at various angles relative to the ultrasound transducer.

fiber optical bundle fixed around the transducer [12] and the needle sample was placed in the imaging plane of the ultrasound imaging transducer (Fig. 3.1). This arrangement allowed both light and sound delivery along the same plane. Each fiber in the bundle was 0.6 mm in diameter with NA of 0.22. Fiber bundle efficiency was approximately 60%. In this experiment, a 30-gauge (30G) x 1.0 inch hypodermic syringe needle (Fig. 3.2), made of 305 bulk stainless steel (Becton Dickinson, Franklin Lakes, NJ) was inserted horizontally into a fresh healthy porcine muscle specimen. The approximately 30 x 30 x 30-mm^3 tissue sample was immersed in water for acoustic coupling between the ultrasound transducer and the tissue (Fig 3.1). Ultrasound and photoacoustic RF-signals were collected with the needle oriented orthogonal to the imaging plane, then the transducer was axially rotated 90°, and the imaging procedure repeated, capturing the length of the needle in the imaging plane.

To investigate the angular dependence of the ultrasound and photoacoustic signal, a second experiment was performed using a 7.5 MHz, f#/4, single element transducer, mechanically scanned across the axial dimension of a set of needles using both ultrasound and photoacoustic imaging (Fig 3.3) [13]. The purpose of this experiment was to determine the needle angles at which the metal needle would be visible, both in ultrasound and photoacoustic imaging and to demonstrate the effectiveness of photoacoustic imaging for detecting needles. From a geometry standpoint, needles are usually oriented at an angle relative to the imaging transducer. Five 21-gauge (21G) x 1.0 inch needles made of 305 bulk stainless steel (Becton Dickinson, Franklin Lakes, NJ)

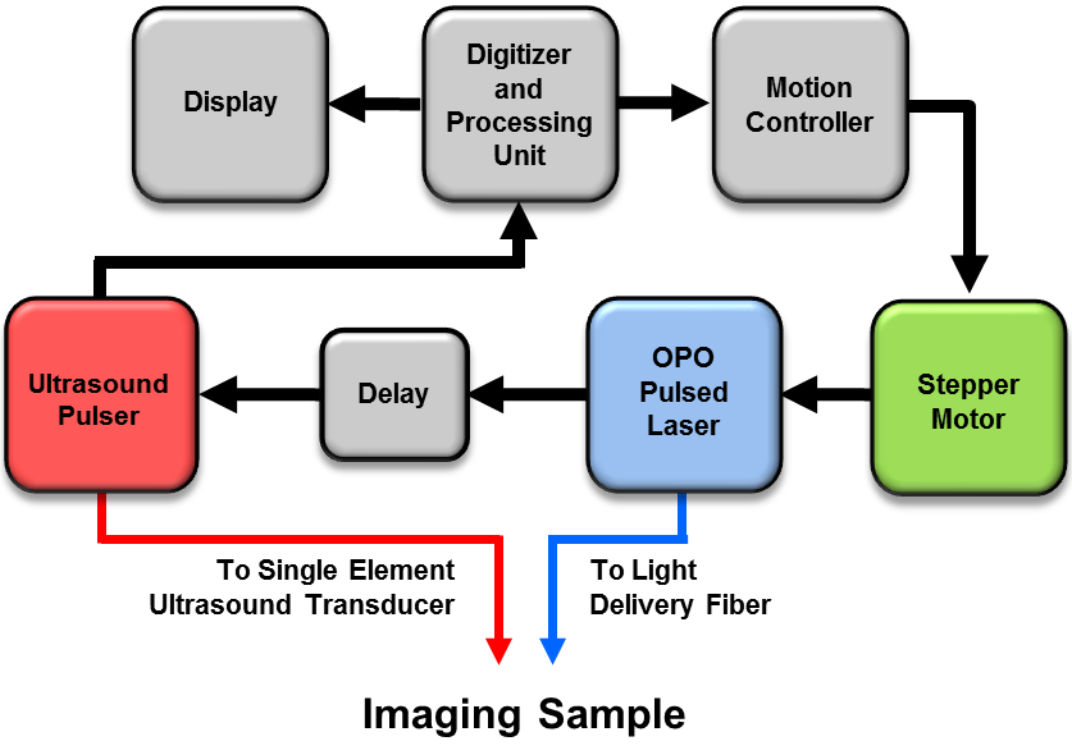

Figure 3.3: Experimental setup for imaging of metal needles positioned at different angles in water and gelatin phantom. Imaging was performed with a single element ultrasound transducer (7 MHz, f-number=4). The center frequency of this transducer was similar to the imaging array used in Fig 3.1. Imaging sample was irradiated at with 800 nm wavelength light. Laser fluence was approximately equal to 10 mJ/cm^2.

were positioned both in water and in gelatin phantoms at angles 0°, 5°, 10°, 20°, and 30° relative to the horizontal plane, i.e. the surface of the ultrasound transducer. The gelatin phantom was created using 6% gelatin by weight, and a small amount (less than 1%) of 40 μm size silica particles which served as optical scatterers. Photoacoustic imaging was conducted at 800 nm and light was delivered using a single optical fiber. The fiber had a diameter of 1.5 mm and NA of 0.39.

3.3 RESULTS

The first experiment the metal needle, in porcine tissue, was inserted parallel to the transducer surface and perpendicular to the imaging plane. Cross-sectional ultrasound and photoacoustic images of the needle and tissue were produced (Figs 3.4a and 3.4b). The ultrasound (Fig 3.4a) showed bright signal in the middle of the image where the needle is located. Surrounding the needle's signal was the ultrasound speckle obtained from the porcine tissue. The photoacoustic image at the same position also showed a bright signal in the center corresponding to the needle cross-section. After obtaining these images, the sample was rotated 90° relative to the transducer, aligning the needle shaft directly in the imaging plane of the transducer (Figs 3.4c and 3.4d). Similarly, the ultrasound image (Fig 3.4c) displayed a bright acoustic reflection from the needle, surrounded by acoustic speckle from the tissue background. The photoacoustic image of the needle shaft (Fig 3.4d) also produced a large signal from the needle, but very little signal from the background, similar to the photoacoustic image in Fig 4b. As the metal needle was placed parallel to the transducer surface in these images, the needle was easily

visible in the ultrasound and photoacoustic images. At this orientation (i.e., perpendicular angle between axis of the ultrasound beam and longitudinal axis of the needle), the needle produced strong ultrasound signal due to the high specular reflectivity of the needle. Ultrasound comet-tail artifacts were also created behind the needle since acoustic waves were reflected within the needle, creating additional signals that appeared to propagate beyond and around the needle (Fig. 3.4a,d). The artifacts introduced into the ultrasound image, subsequently reduced the ability to determine the precise location of the needle. However, the comet-tail made it very easy for the needle's presence to be identified in the image. The photoacoustic signals here confirmed the presence of the highly absorbing metal needle.

Ultrasound and photoacoustic images (Fig. 3.5) were also obtained with the needle inserted into the phantom at a slight downward angle. In these images, the cross-section of the needle was once again located in the center of the images, similar to Figures 3.4a and 3.4b. However the needle here was angled away from the transducer. The ultrasound still showed the background speckle of the porcine tissue but the needle in the center of the image cannot be easily visualized (Fig 3.5a). A photoacoustic image was obtained at the same position (Fig 3.5b). Despite the angled needle invisible in ultrasound, the photoacoustic image showed a bright spot in the center of the image where the cross-section of the needle was located. By combining Figures 3.5a and 3.5b, the co-registered ultrasound and photoacoustic images displayed the presence of the angled needle in the tissue background (Fig 3.5c).

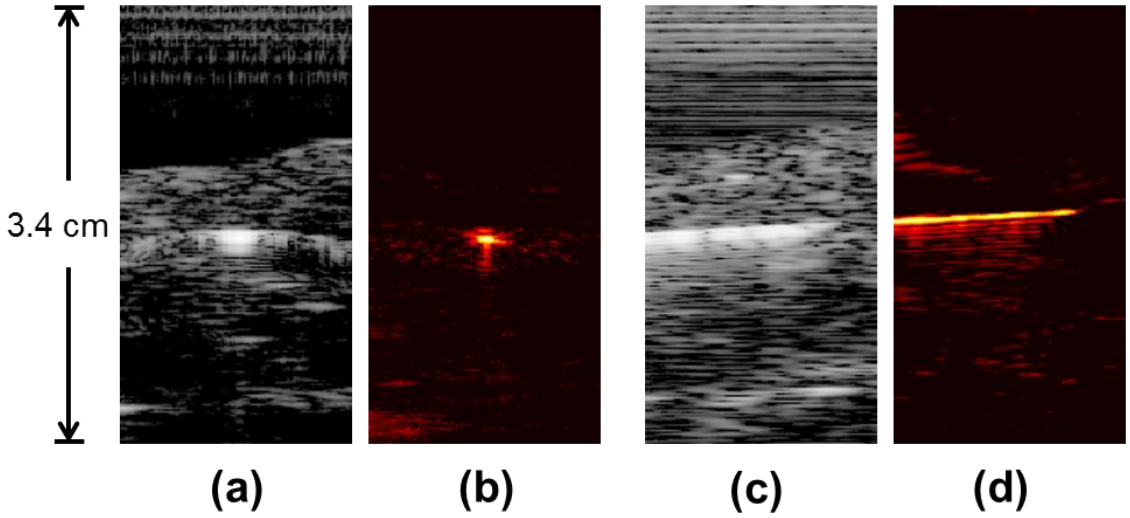

Figure 3.4: Images of hypodermic needle inserted perpendicular to ultrasound transducer. Needle is inserted horizontally through pork loin sample. Transducer is located towards the top of images. (a) Ultrasound image of needle cross-section in pork sample. (b) Photoacoustic image of needle cross section where the needle is easily visible. (c) Ultrasound image of needle and tissue in transducer imaging plane. (d) Photoacoustic image of needle in transducer imaging plane, where the metal needle is clearly visible. Dimensions of pork loin approximately 30 x 30 x 30 mm^3. Ultrasound images are displayed at 40 dB, photoacoustic images 20 dB.

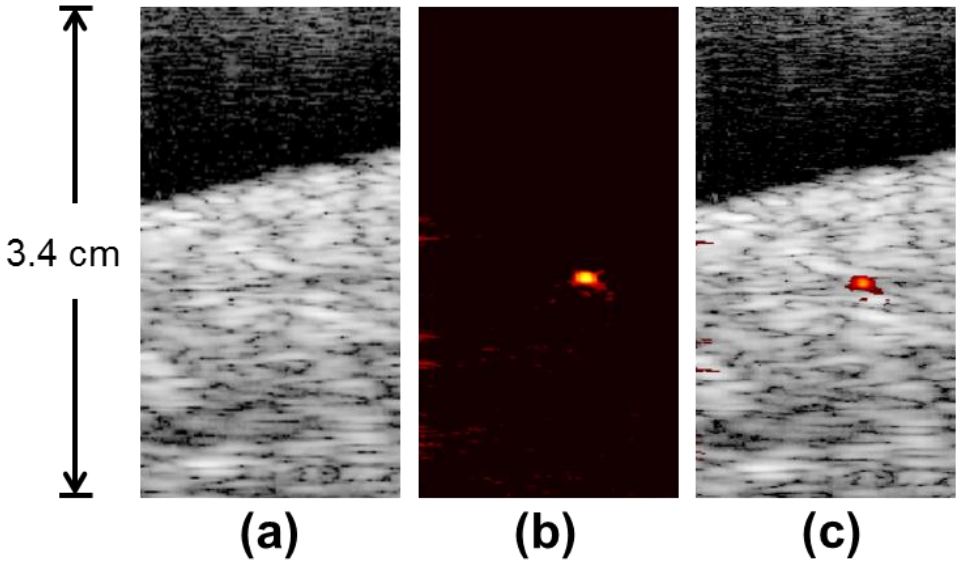

Figure 3.5: Images of hypodermic needle inserted angled approximately 15° with respect to horizontal. Needle is repositioned in the same tissue from Figure 4. Transducer is oriented at the top of the images. (a) Ultrasound image of tissue containing needle cross-section. The angled needle is not visible. (b) Photoacoustic image of same cross section as (a). The highly absorbing needle appears very clearly. (c) Combined US and PA image showing the exact location of the needle within the tissue. Ultrasound images are displayed at 40 dB, photoacoustic images 20 dB. Since ultrasound and photoacoustic images are obtained at the same position, the two images are spatially co-registered.

In ultrasound, the angled needle had reflected the acoustic pulses away from the transducer, thereby decreasing the signal intensity from the needle resulting in decreased visibility in the resulting image. However, the photoacoustic signal was not significantly affected by this angular dependence and the needle remained highly visible within the tissue background even when it was not perpendicular to the transducer. In general, the photoacoustic response from rounded objects occurs omni-directionally which allows for the signal to be less affected by needle angle compared to ultrasound. Comet-tail artifacts are, however, directionally dependent which is why they are not visible in the image of an angled needle. Furthermore and more importantly, there is excellent contrast in the photoacoustic response between the needle and the background tissue.

In the second experiment, cross-sectional ultrasound and photoacoustic images of the five angled 21G needles were obtained (Fig 3.6). From left to right, the needles were inserted into a acrylic holder at decreasing angles from 30° to 0°. The ultrasound image (Fig 3.6a) showed the cross-sections of the needle with decreasing visibility as the needle angle was increased. Similarly, the photoacoustic image (Fig 3.6b) showed the needles at the same position but with less decrease in signal as needle angle was increased. The addition of the gelatin phantom background in Figure 3.7 obtained shows both the ultrasound and photoacoustic images of the needles, similar to Figures 3.6a and 3.6b. The ultrasound image of the needles in the gelatin phantom showed overall decreased visibility of the needles in the presence of the background speckle. On the other hand, all the needles were fully visible in the photoacoustic image; the PA signal intensity did not

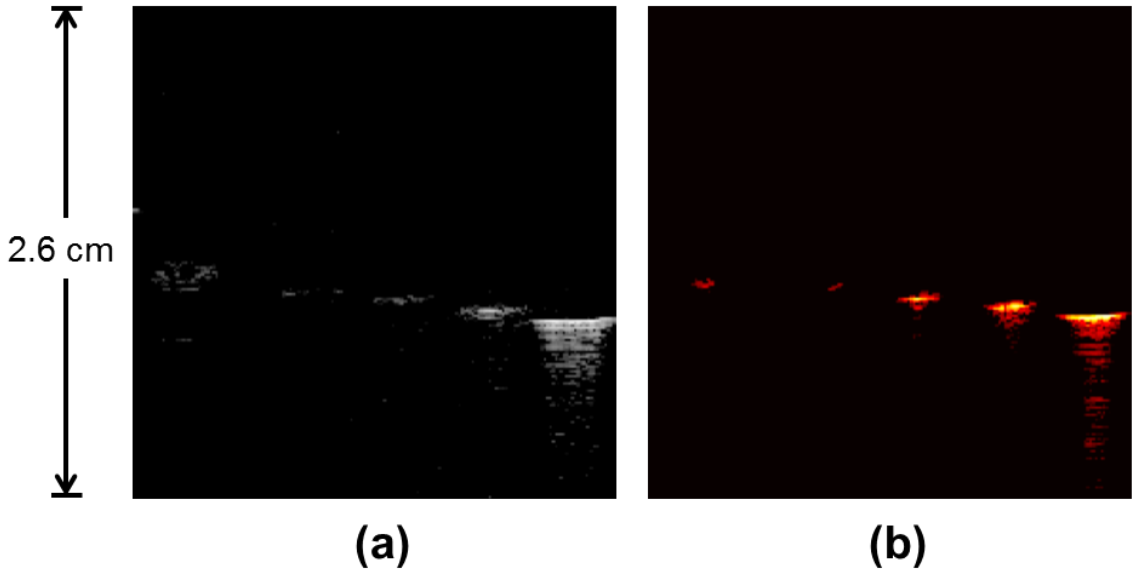

Figure 3.6: Cross-sectional image of five 21G needles in water. Needles are angled downwards with respect to the horizontal plane. From left to right, needles are angled at 30°, 20°, 10°, 5°, and 0°, respectively.

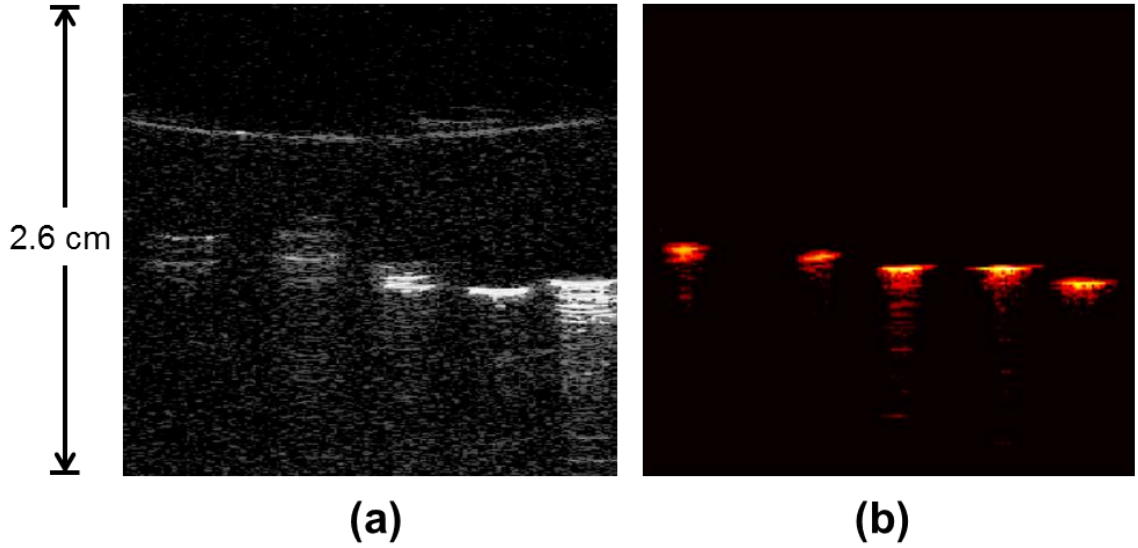

Figure 3.7: Cross-sectional image of five 21G needles inserted into tissue-mimicking gelatin phantom containing optical scatterers. From left to right, needles are angled at 30°, 20°, 10°, 5°, and 0° downwards with respect to horizontal plane.

decline with needle orientation at the angles used in this experiment. Furthermore, the presence of optical scatterers helped to deliver light within the phantom. Figure 3.7b showed increased photoacoustic signal due to better light delivery to the needles in the phantom.

In both the water (Fig 3.6) and tissue-mimicking phantom (Fig 3.7) experiments the maximum signal intensity came from the needles that were horizontal from the transducer surface. In water, all the needles were at least dimly visible in ultrasound, although the signal intensity and spatial resolution was severely limited at needles angled greater than 10°. The addition of acoustic scatterers in the phantom background made the needles less visible under ultrasound. Needles at angles greater than 10° were invisible against the background. The photoacoustic signals from the needles remained easily visible in the gelatin, except for a slight decrease in signal intensity due to light attenuation from the phantom. This did not adversely affect the imaging of the needles as they were still very visible due to the high absorption coefficient of metal.

3.4 Discussion and Conclusions

Overall, photoacoustic imaging was shown to image the needles with high contrast over ultrasound due to the lack of background tissue seen in photoacoustic imaging. Ultrasound and photoacoustic images of needles are shown in Figures 3.4-3.7. In each set of images, the photoacoustic images showed very high contrast between the metal and the phantom or tissue backgrounds. Indeed, the photoacoustic signal from the metal is very strong due to the high optical absorption of metal compared to the gelatin

phantom which has little to no photoacoustic response and therefore results in very high contrast. In tissue, high contrast between the metal structure and tissue constituents was found. Optical absorption of other tissue constituents is generally known to be far lower than that from the metal at the near infra-red spectrum range. By comparison, the ultrasound image visualized the tissue structure and morphological features. Since the ultrasound and photoacoustic images were already spatially co-registered, combining the two images showed complementary information. The locations of the metal implants (PA image) were given in relation to the background tissue (US image).

Both experiments showed strong comet-tail artifacts when imaged with ultrasound and photoacoustic imaging. Fast Fourier transforms of the A-lines containing RF signals showed that frequency content of the comet-tail was slightly different than the center frequency of the transducer. Therefore, bandpass filtering was performed to reduce the artifacts from the photoacoustic image of the needle in Figure 3.4. Prior to applying the signal filter, comet-tail artifacts could be seen emanating from the position of the needle in the photoacoustic image (Fig 3.8a). When correct bandpass filtering was performed (4 MHz to 10 MHz), the comet-tail disappeared from the image (Fig 3.8c). However, specifying the incorrect frequency range (3 MHz to 10 MHz) resulted in undesired treatment of the image and did not correctly remove the image artifacts (Fig 3.8b).

Bandpass filtering was able to remove the image artifacts, albeit at a decrease in the contrast to noise ratio (CNR) [14, 15]. Without filtering, the CNR of Figure 3.8a was

found to be 39 dB. Figure 3.8b was reported to contain a CNR of 38 dB, and Figure 3.8c had a CNR of 33 dB.

Attempts to perform the same filtering technique to the ultrasound image were unsuccessful. Examination of the time domain signal revealed that the comet-tail artifact produced in ultrasound contained a discontinuous signal different from the photoacoustic image. While the resulting artifacts in the ultrasound and photoacoustic signals were visually similar, the photoacoustic comet-tail signal was continuous, decreasing over time similar to an acoustic reverberation (Fig 3.9a). On the other hand, the ultrasound comet-tail was discontinuous, having burst-like signals that decreased in amplitude over time (Fig 3.9b). These burst-like signals in ultrasound are therefore not easily removed without using more advanced filtering methods.

The combined US and PA imaging modality was able to image 1-2 centimeters into tissue, necessary for the imaging of metal needles inserted into the body. Current practice using ultrasound imaging for guidance is ineffective to image metal in all cases, especially where highly reflective surfaces redirect ultrasound echoes away from the transducer. In most cases, clinicians are usually only able to use the ultrasound shadows from the metal to infer the location of the needle. The experimental results presented here demonstrate that photoacoustic imaging is suitable for imaging metal. Combined with ultrasound imaging, the PA signal from the metal inclusions was visible in relation to its position to the surrounding tissue/phantom structures, which were visible in the ultrasound signal.

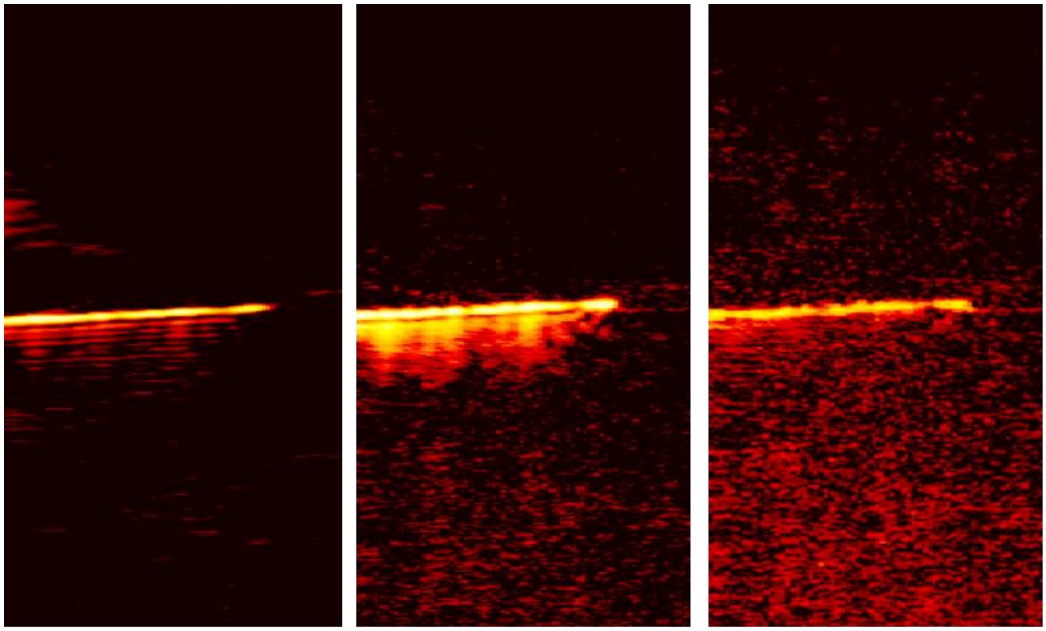

Figure 3.8: Photoacoustic image from Figure 4d showing filtering technique to remove comet-tail artifacts. (a) Unfiltered photoacoustic image of horizontal needle. FFT of the signal shows one frequency peak at the center frequency of the transducer (7 MHz), and one at a lower frequency, around 3 MHz, representing the signal from the comet-tail. (b) Result of bandpass filtering demonstrating incorrect choice of cut-off frequencies (3 MHz to 10 MHz). Low-frequency components are still present, blurring out the artifacts (c) Correct bandpass filtering (4 MHz to 10 MHz) which eliminated the comet-tail artifact. Contrast to noise ratio in (a), (b) and (c) calculated to be 39.3 dB, 38.2 dB, and 32.5 dB, respectively.

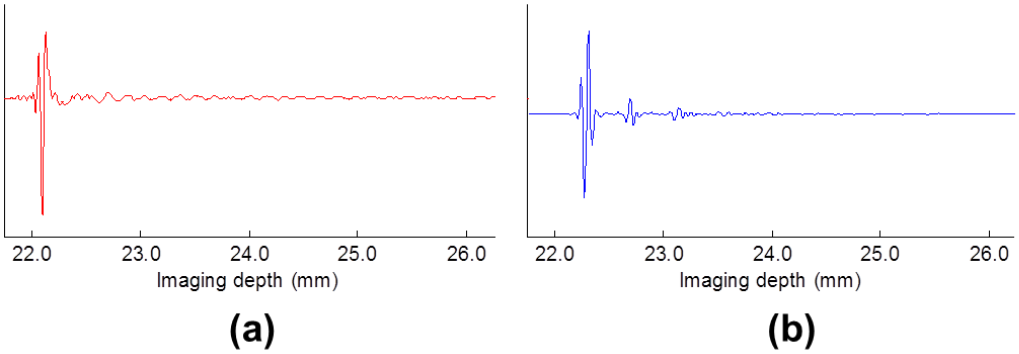

Figure 3.9: Individual A-lines of RF-signal through needle demonstrating the nature of the comet-tail artifact. Though the images appear similar, the underlying signals are not. (a) Photoacoustic A-line. The comet-tail artifact appears to be a continuous signal which diminishes over time. (b) Ultrasound A-line at the same location. The comet-tail artifact in ultrasound appears as a discontinuous train of signal bursts which decrease in amplitude over time.

The use of 1064 nm wavelength light is a huge advantage for clinical in-vivo settings due to low-cost and simplicity of the Nd:YAG laser, deep penetration of the light into tissue and high photoacoustic contrast between metal objects and surrounding tissue. By using a 1064 nm laser, users do not require an expensive, complex laser system to conduct imaging tests. At 1064 nm wavelengths, light offers deep penetration into tissue and therefore imaging will require less laser fluence for photoacoustic signal while still preserving signal-to-noise, contrast-to-noise and safety. The imaging studies conducted here used laser energies well below the maximum permissible exposure level set by the ANSI standard. These laser energies coupled with an array-based imaging transducer make it possible to image photoacoustic signals in real-time. Our current set-up in this experiment was limited to a repetition rate of 10 Hz, but inexpensive lasers operating at 30 Hz or higher could be used for real-time imaging. The photoacoustic contrast in the tissue studies demonstrated that at 1064 nm, metal was more highly absorbing than the surrounding tissue; therefore showing that 1064 nm is an effective wavelength choice for imaging metal in the body.

Though the first photoacoustic imaging experiment in this study was conducted at 1064 nm, the second experiment was conducted at 800 nm, suggesting that multiple wavelengths could be used for spectroscopic photoacoustic imaging which could be utilized to further differentiate between metal and tissue [16]. Since the photoacoustic effect is directly related to optical absorption, photoacoustic data from multiple wavelengths could be used to calculate absorption spectra in the resulting image. Tissue

constituents, having a unique optical absorption spectrum from metal, could then be differentiated from the metal, identifying both the composition of tissue with respect to the location of metal implants.

Our previous work has shown that photoacoustic imaging of needles is not limited to needles. A host of metal devices are used in the human body, either temporarily or permanently, many of which must be identified or monitored [17, 18]. Combined intravascular ultrasound (IVUS) and photoacoustic imaging (IVPA) has been shown to image arterial stents and their positioning within the arterial wall [16]. The combination of IVUS and IVPA was found to give complementary information as the ultrasound image gave structural/morphological information of the arterial wall, while the IVPA image could hypothetically show the location of the stent, its position within the wall, and also the location of arterial plaques. It has also been proposed that this combined ultrasound and photoacoustic imaging could be used to image brachytherapy seeds during and after implantation into the body. Brachytherapy seeds are implanted to locally treat prostate cancer. However, the seeds have been found to migrate throughout the body which can cause problems as they lodge themselves in other areas of the body such as the lungs [19]. Photoacoustic imaging could be used to detect the location of the seeds as they shift around in the prostate. The imaging could be performed tomographically, reconstructing multiple slices of ultrasound and photoacoustic data to create a three-dimensional image of a localized region.

It can also be possible to treat metal with substances that have strong absorption peaks at specific wavelengths. This would allow the metal absorption peaks to be tuned towards or away from wavelengths where tissue shows strong photoacoustic signal, making the metal components easier to identify alongside other tissue constituents such as cancerous lesions. These coatings could be used concurrently with multi-wavelength photoacoustic imaging [13, 20] to differentiate implants from tissue as unique absorption peaks can be expected from the coated metal. Currently, there exist echogenic needle polymer coatings which make the needle tip and shaft highly visible under ultrasound [21]. Similar coatings with optically absorbing properties could also be coated onto the metal to make metal implants even more visible at other wavelengths in photoacoustic imaging. Various molecular-sensitive coatings could also be used so that the absorption properties of the coated metal would change depending on the tissue background in contact with the metal. These metals could possibly also be used for specific tissue detection based on environment-dependencies of the photoacoustic signal.

Identification of metal in the body requires the visualization of landmarks in the body. The combination of ultrasound and photoacoustic imaging offers the high contrast of metal implants in PA imaging, with the co-registered anatomical positioning of ultrasound. Used in real-time, this combination can offer a very powerful tool not only for identifying metal implants, but also for identifying their relative location to other structures in the body such as tumors and plaques. The ability to identify metal implants and surroundings is highly necessary in image-guided therapy.

3.5 REFERENCES

1. Charboneau, J.W., C.C. Reading, and T.J. Welch, *CT and sonographically guided needle biopsy: current techniques and new innovations.* AJR Am J Roentgenol, 1990. **154**(1): p. 1-10.

2. Chapman, G.A., D. Johnson, and A.R. Bodenham, *Visualisation of needle position using ultrasonography.* Anaesthesia, 2006. **61**(2): p. 148-58.

3. Chin, K.J., A. Perlas, V.W. Chan, and R. Brull, *Needle visualization in ultrasound-guided regional anesthesia: challenges and solutions.* Reg Anesth Pain Med, 2008. **33**(6): p. 532-44.

4. Abolhassani, N., R.V. Patel, and F. Ayazi, *Minimization of needle deflection in robot-assisted percutaneous therapy.* Int J Med Robot, 2007. **3**(2): p. 140-8.

5. Nath, S., Z. Chen, N. Yue, S. Trumpore, and R. Peschel, *Dosimetric effects of needle divergence in prostate seed implant using 125I and 103Pd radioactive seeds.* Med Phys, 2000. **27**(5): p. 1058-66.

6. Schafhalter-Zoppoth, I., C.E. McCulloch, and A.T. Gray, *Ultrasound visibility of needles used for regional nerve block: an in vitro study.* Reg Anesth Pain Med, 2004. **29**(5): p. 480-8.

7. Hatada, T., H. Ishii, S. Ichii, K. Okada, and T. Yamamura, *Ultrasound-guided fine-needle aspiration biopsy for breast tumors: needle guide versus freehand technique.* Tumori, 1999. **85**(1): p. 12-4.

8. Phal, P.M., D.M. Brooks, and R. Wolfe, *Sonographically guided biopsy of focal lesions: a comparison of freehand and probe-guided techniques using a phantom.* AJR Am J Roentgenol, 2005. **184**(5): p. 1652-6.

9. Ziskin, M.C., D.I. Thickman, N.J. Goldenberg, M.S. Lapayowker, and J.M. Becker, *The comet tail artifact.* J Ultrasound Med, 1982. **1**(1): p. 1-7.

10. Gronningsaeter, A., T. Lie, K. Bolz, and A. Heimdal, *Ultrasonographic stent-imaging artifacts.* Journal of Vascular Investigation, 1995. **3**: p. 140-149.

11. Finet, G., C. Cachard, P. Delachartre, E. Maurincomme, and J. Beaune, *Artifacts in intravascular ultrasound imaging during coronary artery stent implantation.* Ultrasound Med Biol, 1998. **24**(6): p. 793-802.

12. Homan, K., J. Shah, S. Gomez, H. Gensler, A.B. Karpiouk, L. Brannon-Peppas, and S.Y. Emelianov. *Combined Ultrasound and Photoacoustic Imaging of Pancreatic Cancer Using Nanocage Contrast Agents*. in *Proceedings of the 2009 SPIE Photonics West Symposium: Photons Plus Ultrasound: Imaging and Sensing*. 2009.

13. Mallidi, S., T. Larson, J. Tam, P.P. Joshi, A. Karpiouk, K. Sokolov, and S. Emelianov, *Multiwavelength photoacoustic imaging and plasmon resonance coupling of gold nanoparticles for selective detection of cancer.* Nano Lett, 2009. **9**(8): p. 2825-31.

14. Park, S., S.R. Aglyamov, W.G. Scott, and S.Y. Emelianov, *Strain imaging using conventional and ultrafast ultrasound imaging: numerical analysis.* IEEE Trans Ultrason Ferroelectr Freq Control, 2007. **54**(5): p. 987-95.

15. Varghese, T. and J. Ophir, *An analysis of elastographic contrast-to-noise ratio.* Ultrasound Med Biol, 1998. **24**(6): p. 915-24.

16. Su, J.L., B. Wang, and S.Y. Emelianov, *Photoacoustic imaging of coronary artery stents.* Opt Express, 2009. **17**(22): p. 19894-901.

17. Butany, J., K. Carmichael, S.W. Leong, and M.J. Collins, *Coronary artery stents: identification and evaluation.* J Clin Pathol, 2005. **58**(8): p. 795-804.

18. Wei, Z., M. Ding, D. Downey, and A. Fenster, *3D TRUS guided robot assisted prostate brachytherapy.* Med Image Comput Comput Assist Interv Int Conf Med Image Comput Comput Assist Interv, 2005. **8**(Pt 2): p. 17-24.

19. Morooka, M., K. Kubota, Y. Kono, K. Ito, K. Kurihara, T. Mitsumoto, T. Sato, Y. Oshiro, T. Aruga, K. Hasuo, M. Kanemura, and S. Minowada, *Scintigraphic detection of I-125 seeds migration after permanent brachytherapy for prostate cancer: how far do seeds travel?* Clin Nucl Med, 2009. **34**(7): p. 466-9.

20. Sethuraman, S., J.H. Amirian, S.H. Litovsky, R.W. Smalling, and S.Y. Emelianov, *Spectroscopic intravascular photoacoustic imaging to differentiate atherosclerotic plaques.* Opt Express, 2008. **16**(5): p. 3362-7.

21. Tavakoli, M., E.J. Kellar, D. Nassiri, and A.E. Joseph, *A novel polymeric coating for enhanced ultrasound visibility of medical devices.* Med Device Technol, 2006. **17**(2): p. 8-10, 12.

Chapter 4: Photoacoustic detection of brachytherapy seeds used in prostate cancer therapy

4.1 INTRODUCTION

In 2010, prostate cancer was the second most common cancer among men, with 217,730 cases that year alone [1]. The use of brachytherapy seeds, metal implants which deliver localized radiation therapy, is becoming a common treatment option for prostate cancer [2]. Brachytherapy seeds are typically minute (0.8 x 4.5 mm) capsules of stainless steel or titanium that are filled with a radioisotope, most commonly iodine-125 or palladium-103. Implantation is achieved by injecting the seeds (typically, 70-150 of them) into a cancerous prostate by way of metal guide needles that are inserted through a patient's perineum according to a pre-established treatment plan. Currently, the standard of care for the guidance of brachytherapy seed implantation is transrectal ultrasound (TRUS) [3], which can gain imaging access to the prostate given the gland's adjacency to the rectal wall and its modest size, with a mean±SD diameter (i.e., height or width dimension), according to a study by Hricak *et al.*, of 4.3±1.0 cm for men (n = 15) aged 52-67 years [4]. Since visualization of the small seeds can be difficult, the ultrasound-derived position of the needles - and not the seeds themselves - is often relied upon to infer seed placement [5]. Acoustic shadowing from microcalcifications, off-axis seed placement (i.e., where the ultrasound beam widens), and placement in specific regions of the prostate (e.g., in the periprostatic region, which can have a similar echogenicity to the seeds) can make visualization of seeds with TRUS difficult [6]. Additionally, the acoustic

signal generated by a seed is highly dependent on its orientation, with seeds oriented with their long axis perpendicular to the beam more apt to being detected [7]. Given the difficulty in accurately visualizing seeds with TRUS, CT imaging is typically utilized for post-implant dosimetric evaluations [8]. Seed placement that deviates from the dosimetric treatment plan can result in underdosed cancerous regions, requiring postoperative dose corrections through external-beam radiation therapy [3]. Needle deflections of only 5° from the insertion angle decrease the minimum target dose by 10%, thus increasing the tumor-cell survival rate by a factor of 200 [9].

Photoacoustic (PA) imaging is an imaging technique in which tissue is irradiated with nanosecond pulses of low-energy laser light [10]. Through the processes of optical absorption followed by thermoelastic expansion, broadband ultrasonic (US) acoustic waves are generated within the irradiated volume. Using an ultrasound transducer, acoustic waves can be detected and spatially resolved to provide an image that is related to the local optical absorption of tissue constituents. Metals experience an optical absorption that is orders of magnitude greater than that experienced by soft tissue (Fig. 1.1), and thus PA imaging provides excellent contrast of metals embedded in soft tissue. Relying on this phenomenon, PA imaging has already been demonstrated to improve the image contrast of clinical metal needles in excised tissue specimens [11]. Generally, PA imaging cannot offer the soft tissue contrast afforded by US imaging. Since an ultrasound transducer is used in PA imaging, however, it is possible to obtain co-registered PA and US images. Consequently, a combined PA and US (PAUS) imaging approach will not

only improve needle visualization during a seed implantation procedure, but it also promises to allow for the reliable visualization of the conventional, non-modified seeds themselves. Such a capability would improve adherence to a patient's dosimetric treatment plan, may allow for intraoperative dynamic dose optimization, and could obviate the need for costly and ionizing CT-based post-implant evaluations and external-beam radiation corrections [12, 13].

4.2 Materials and Methods

To test the feasibility of using PAUS to image brachytherapy seeds, several imaging studies were conducted using non-reactive, stainless steel, iodine-125 brachytherapy seeds (IsoAid LLC, Port Richey, FL). PAUS imaging studies were performed using a Cortex ultrasound imaging system (Winprobe Corp., North Palm Beach, FL) that was interfaced with a 7-MHz center frequency, 14-mm-wide, 128-element linear array transducer (L7, Acuson Corp., Mountain View, CA). An Nd:YAG pump laser (Quanta-Ray PRO-290-10, Newport Corp., Irvine, CA) with OPO laser output (premiScan/BB 650 OPO, Newport Corp., Irvine, CA) and a nominal pulse width of 5 ns was synchronized to the ultrasound acquisition system to optically illuminate the sample in which the seed was embedded. The imaging system was capable of acquiring co-registered PA and US images to facilitate PAUS imaging.

In the first experiment (i.e., the “angular dependence experiment”), the angular dependence of the US and PA signals on seed orientation was investigated. A non-reactive brachytherapy seed was embedded in 8% gelatin at 45° relative to the horizontal

("Side View" of Fig. 4.1). In an effort to evaluate the seed independently from background influences, acoustic/optical scatterers were not added to the gelatin phantom. A mechanical stage was configured to rotate the transducer from 45° to 135° (relative to the same horizontal reference) in 15° increments. This allowed the long axis of the seed to be imaged at angles from 0° to 90° relative to the transducer face. Both the gelatin phantom and the transducer face were immersed in deionized water to provide acoustic coupling. The seed was placed at the fulcrum of the transducer's rotation to ensure that the seed remained in approximately the same location in the transducer's field of view through the 90° rotation. The laser was operated at 800 nm for PA imaging and was delivered to the sample using a single optical fiber; the fiber had a diameter of 1.5 mm, an NA of 0.39, and was positioned at an oblique angle to the US beam axis ("Front View" of Fig. 4.1). During the experiment, the laser irradiation position was not altered - the optical fiber and seed were held fixed while only the transducer was rotated - in order to demonstrate that signal changes were due only to the positioning of the transducer relative to the seed.

In a second experiment (i.e., the "bare seed spectrum experiment"), the spectrum of a bare seed's PA signal was established. A non-reactive seed was embedded in a block of 8% gelatin and centered in the imaging plane with US imaging (using the aforementioned system/transducer). PA images of the seed were then obtained from 750 to 1090 nm in 20-nm increments, including 1064 nm. The extinction spectrum of the gelatin alone was analyzed using a UV-VIS-NIR spectrophotometer (UV-3600,

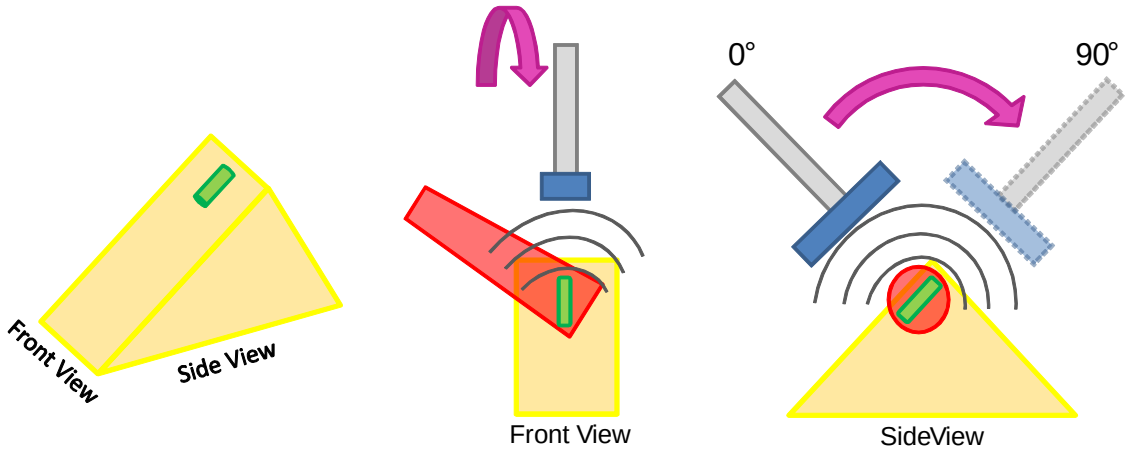

Figure 4.1: Schematic representation of 3D phantom (left) and front (center) and side (right) view of transducer rotation apparatus. Yellow triangle/rectangle represents gelatin background; green ellipsoid, seed; blue and gray rectangles, transducer and mount, respectively. Red-shaded regions denote laser irradiation, while black lines represent acoustic transmission, both of which are oversimplifications and included for illustration purposes only. Purple arrow indicates transducer rotation axis.

Shimadzu Corp., Kyoto, Japan) and found to not significantly influence multi-wavelength PA imaging within the spectrum utilized for testing.

A third experiment (i.e., the "prostate tissue experiment") was performed to examine PAUS imaging of brachytherapy seeds in a more realistic environment. In this experiment, five seeds were embedded into five excised bovine prostate samples, which were imaged within 24 hours of each animal's sacrifice, were never frozen, and were cut to be cubical in shape. The proximal tip of each seed was buried approximately 1 mm below the surface of the tissue at varied distances away from each sample's edge (see white scale in Fig. 4.2a). Each prostate sample was then cast in gelatin to prevent tissue discoloration or deterioration due to water immersion. The first of the five samples was oriented so that the seed's long axis was perpendicular to the US transducer face ("Short-axis Orientation" in Fig. 4.2b). This orientation was chosen to provide a minimum irradiation path through the prostate tissue of 1 mm, a depth that was too shallow to achieve in the long-axis orientation. For this comparison, multi-wavelength PA imaging, from 750 to 1090 nm, was performed. The other four samples were then oriented so that the seed's long axis was positioned parallel to the US transducer face ("Long-axis Orientation" in Fig. 4.2b). Using US visualization, the depth of each seed from the sample's edge was determined. Four irradiation path lengths were investigated - 4, 10, 13, and 17 mm - while PA images were acquired from 750 to 1090 nm in 40-nm increments, including 1064 nm. Note that PA and US beams were orthogonal to one another and were made to penetrate comparable depths into the tissue (i.e., when the irradiation path was

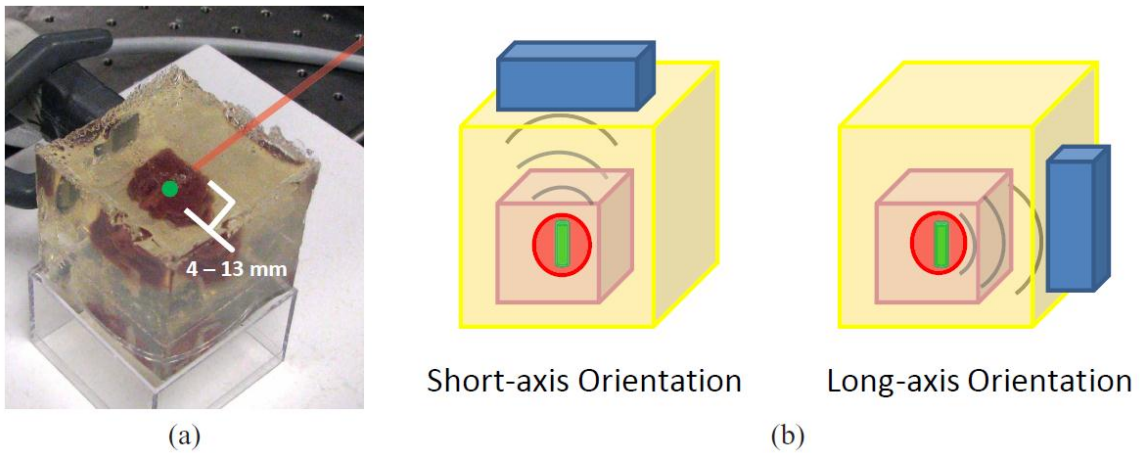

Figure 4.2: Picture of prostate sample cast in gelatin (a) and schematic views of imaging orientations (b). In picture of sample (a), green dot denotes approximate placement of seed (long-axis perpendicular to table), red line indicates example irradiation path, while US transducer is visible in upper-left portion of image (with aperture oriented perpendicular to table). White scale indicates varied distance of seed from front-most sample edge. In schematic depictions (b), short- (left) and long-axis (right) orientations are offered. Peach cube depicts embedded prostate sample; other conventions are same as used in Fig. 4.1.

increased, the US propagation path was increased accordingly).

For the second and third experiments, laser irradiation was delivered using an air beam directed at the seed. In all experimentation, laser fluences were measured for each imaging trial, and the mean (n = 500 pulses) energy was used to normalize the PA amplitude. Standard deviation of the laser fluence was also used to calculate standard error in the PA amplitude at each wavelength.

For quantitative analysis, PA signal energies were calculated using a kernel surrounding the maximum signal from the seed. The kernel was determined by choosing a region of interest (ROI) with pixel values above a certain threshold in the B-mode image, which corresponded to the location of the seed. This region could be visually verified as the location of the seed due to the presence of the comet-tail artifact, which is present in US imaging of metals, that was located distally from the aforementioned ROI. Data points within the kernel were averaged and normalized according to the mean laser fluence obtained during each trial. For contrast calculations, data kernels (0.6 x 0.4 mm) for the signal and background ROIs were chosen in order to obtain kernels containing only the respective signal and background measurements. The size of the kernel did not significantly affect contrast calculations as long as each kernel only contained these signal or background measurements. Several contrast values were obtained by translating the position of the signal kernel through the region of the seed (identified by the US image); a corresponding background kernel was similarly translated through an adjacent tissue region located outside the region of the seed. These values were then averaged

together to obtain a single reported contrast value in US imaging and at each imaging wavelength in PA imaging. Contrast was calculated using:

$$Contrast = \frac{\overline{S_S} - \overline{S_b}}{\overline{S_b}} \qquad (Eq.\ 4.1)$$

where S_s and S_b are the mean signals from a region within the seed and adjacent background, respectively .

4.3 RESULTS

In the angular dependence experiment, PAUS images of the brachytherapy seed were acquired from 0° to 90°, in 15° increments. In both the PA and US images, the seed remained visible as the transducer was rotated. In the US images (grayscale images in Fig. 4.3), when the seed was oriented at 0° relative to the horizontal, the entire seed was visible. A large comet-tail artifact was also visible due to reverberation of the acoustic signal within the seed. As the transducer was rotated, the acoustic signal weakened from the midsection of the seed, while the distal and proximal tips of the seed remained apparent. Through the full rotation, the peak US signal decreased by 13%, with the majority of that decrease occurring between 0° and 30°.

Similar results were observed in the PA images of the seed (yellow-red colormap images in Fig. 4.3), where the 0° orientation offered the best visualization of the full seed. The body of the seed was still visible when rotated to an angle of 15° from the transducer; however, the signal diminished dramatically after that, as seen in rotation angles of 30° and greater. Much like the US images, comet-tail artifacts are present in the PA images. Unlike the US imaging results, however, only the proximal tip of the seed

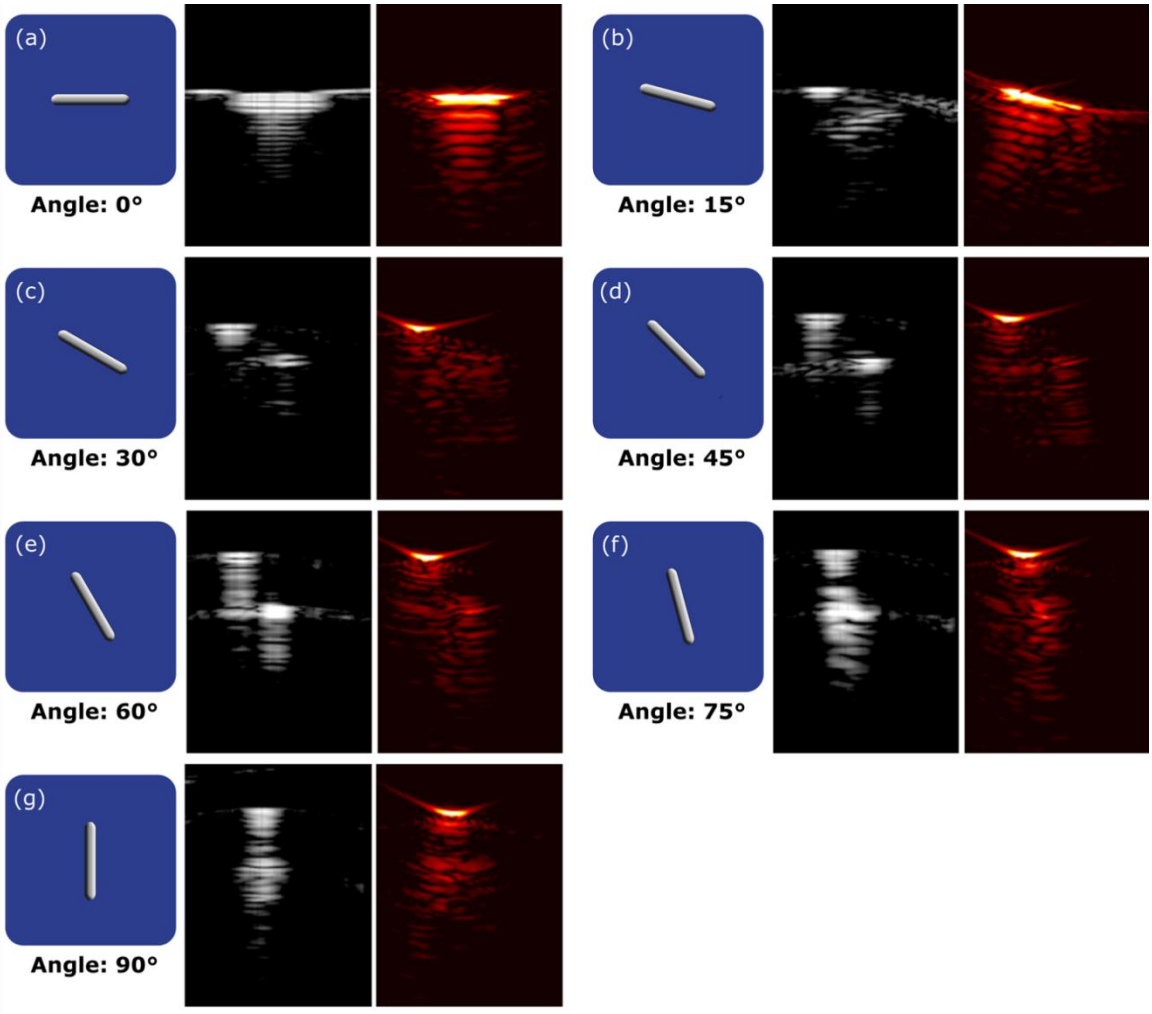

Figure 4.3: US and PA images of brachytherapy seeds at different rotation angles relative to transducer face. Seed schematics (blue background) denote orientation, while first image immediately right offers US B-mode depiction (grayscale) and second image offers PA imaging depiction (yellow-red colormap). PA and US images are displayed with a 30-dB dynamic range, while all images (including schematic) are presented with same scale (i.e., seed is 0.8 x 4.5 mm) and co-registered orientations/positions. Transducer face is located/aligned with top margin of schematic.

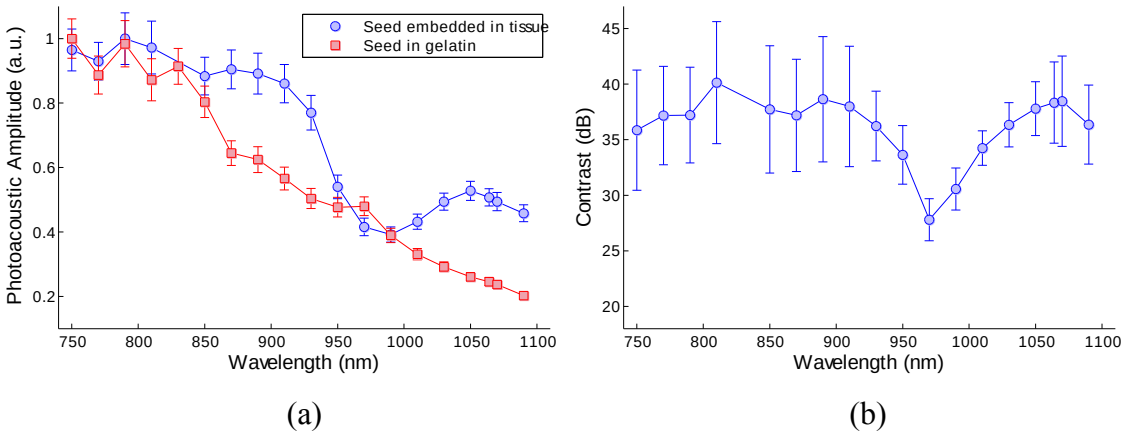

(a) (b)

Figure 4.4: Normalized PA signal of seed embedded in gelatin (a - red square) and embedded in excised bovine prostate (a - blue circle) and contrast spectrum of seed embedded in prostate sample (b). Proximal end of seed is embedded approximately 1 mm from prostate tissue surface (in direction of laser source). Note for the prostate tissue experiment (i.e., blue circle), data file obtained at 830 nm was corrupt and was thus omitted from analysis.

was clearly apparent through the full rotation of the transducer. Through the full rotation, the peak PA signal decreased by 46%, with the majority of that decrease occurring between 15° and 30°.

In the bare seed spectrum experiment, a seed embedded in pure gelatin was imaged with multi-wavelength PA imaging in order to determine the PA spectrum of the seed alone (red square in Fig. 4.4a). The normalized PA signal was plotted with respect to wavelength. The calculated spectrum presented a monotonically decreasing PA signal with increased laser wavelength, with an approximately 80\% reduction in PA signal from 750 to 1090 nm.

The third experiment involved inserting non-reactive seeds into excised bovine prostate tissue. Figure 4.4a (blue circle) offers the PA spectrum of the seed shallowly embedded (short-axis orientation) in prostate tissue. Although the normalized PA signal tends to decrease with wavelength much like the bare seed (red square in Fig. 4.4a), local minima in signal are observed from 950 to 1010 nm, while a local maximum is observed at 1050 nm. Figure 4.4b shows the contrast spectrum for this seed in the short-axis orientation, with a peak (average) PA contrast of 40.1 dB (at 810 nm) compared to an average US contrast of 14.3 dB. Figure 4.5 shows the PAUS images obtained in the long-axis orientation from the 4-mm imaging depth. In the US image (Fig. 4.5a), background speckle is visible throughout the prostate tissue, with the proximal tissue-gelatin boundary clearly visible at 1.2-1.5 cm axially and the sample's edge visible at the 4-mm lateral position. Although a hyperechoic region is visible at the seed location (i.e., 2.4

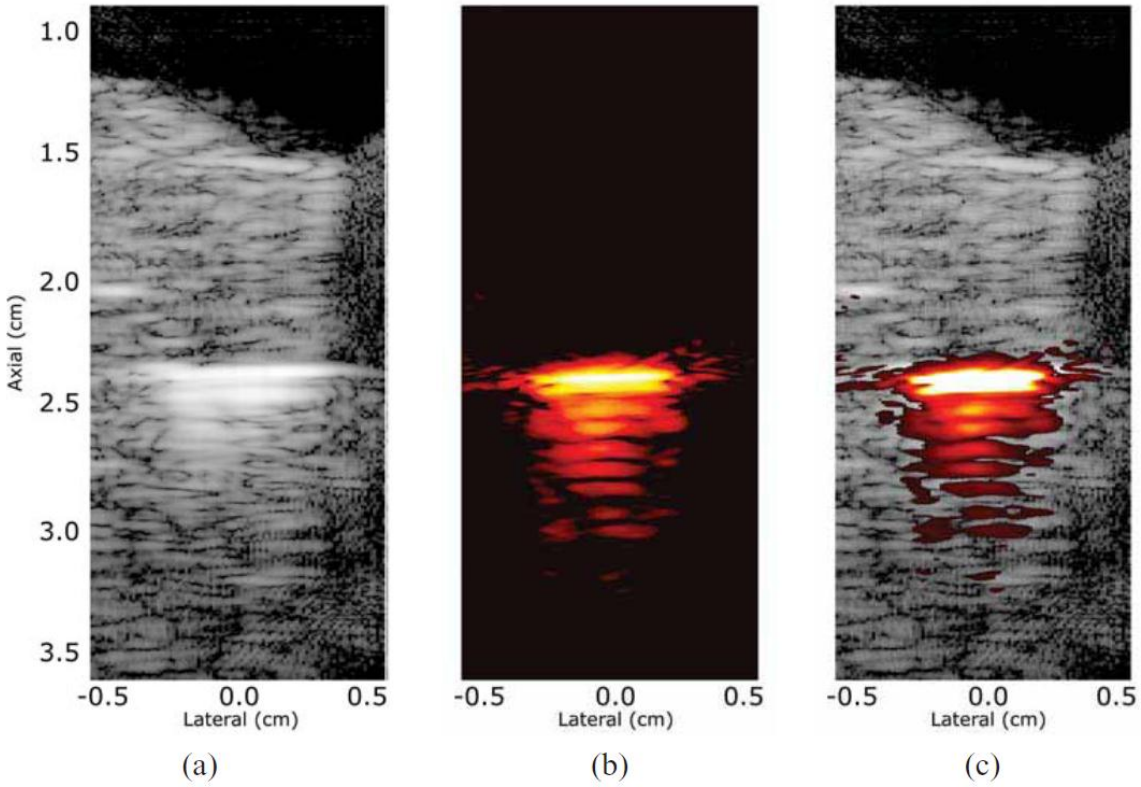

Figure 4.5: US B-mode (a), PA (b), and combined PAUS (c) images of a seed embedded in a bovine prostate sample in the long-axis orientation. PA image was acquired at 870 nm and is displayed with 35-dB dynamic range; B-mode image is displayed with 55-dB range.

cm), the speckle signal from the surrounding tissue reduces overall contrast. A PA image (Fig. 4.5b) obtained at the same position presents a strong acoustic signal from the seed location, but little acoustic signal is present in the surrounding tissue, resulting in a significant improvement in contrast. By combining Figs. 4.5a and 4.5b, the co-registered images (Fig. 4.5c) are able to more clearly display the presence of the brachytherapy seed within the tissue background.

Lastly, the seed was successfully imaged with three different irradiation path lengths, and the PA signal spectrum of each was calculated at nine wavelengths (Fig. 4.6a-c). Note that the seed could not be visualized at 17 mm with the utilized fluences, which were similar to those used for imaging at the three shallower depths. For the other three depths (i.e., 4, 10, and 13 mm), a local maximum of the normalized PA signal exists at 1064 nm, while a local minimum can be observed at 990 nm. PA amplitudes for the 10-mm (b) and 13-mm (c) acquisitions decreased, on average, by 93% and 94%, respectively, when compared to the average PA amplitude of the 4-mm (a) acquisition. Figure 4.6d-f presents the contrast values across the acquired spectrum for the three imaging depths. Peak (average) PA contrasts were 50.6 dB (at 870 nm), 30.3 dB (at 830 nm), and 28.2 dB (at 1064 nm), while average US contrasts were 22.7 dB, 24.7 dB, and 25.5 dB for the 4-mm, 10-mm, and 13-mm acquisitions, respectively. Surface fluences were measured (mean±SD) across the acquired spectrum to be 21.7±2.3, 23.6±3.1, and 22.5±5.1 mJ/cm^2 for the 4-mm, 10-mm, and 13-mm acquisitions, respectively; fluences tended to decrease with increased wavelength. Specifically, at a wavelength of 1064 nm,

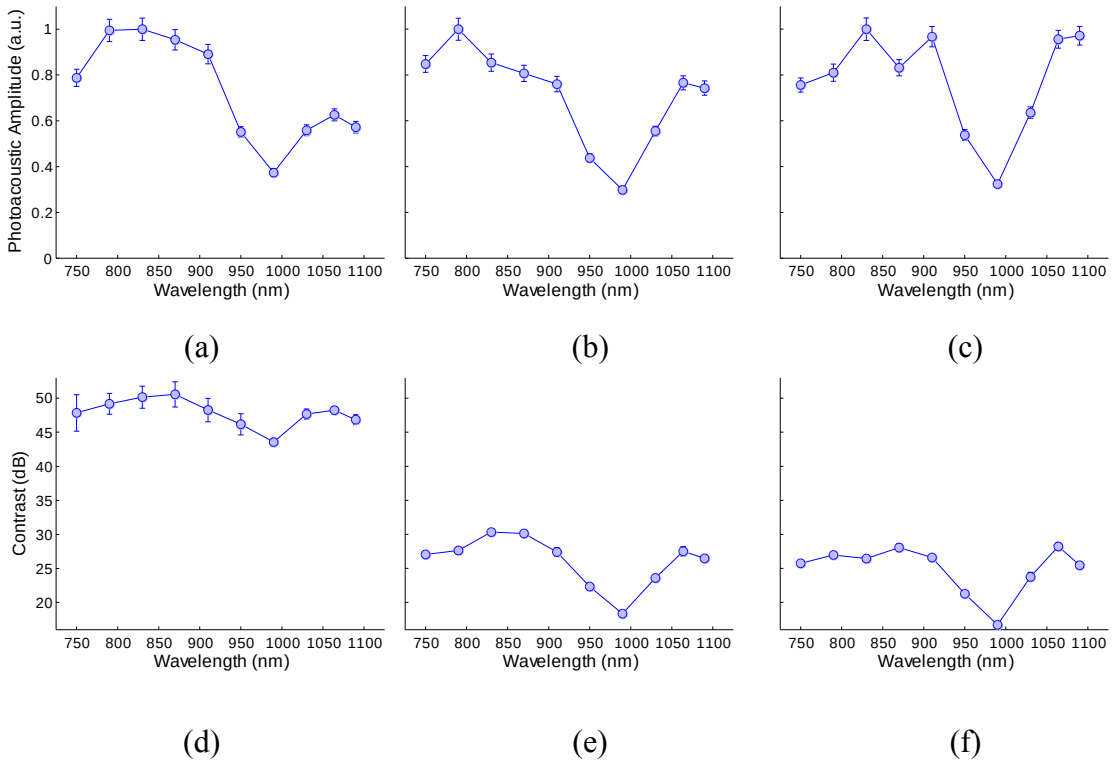

Figure 4.6: Normalized PA spectra and contrast of brachytherapy seed embedded in bovine prostate at three laser irradiation depths: 4 mm (a,d), 10 mm (b,e), and 13 mm (c,f).

surface fluences were measured to be 19.7±0.9, 21.3±0.9, and 20.1±0.8 mJ/cm^2 for the aforementioned acquisition depths, respectively.

4.4 DISCUSSION

PA imaging of brachytherapy seeds embedded in prostate tissue yielded an improvement of at most 27.9 dB in contrast over conventional US imaging, while seeds were successfully visualized at depths of up to 13 mm. Much like US imaging, PA imaging results were dependent on seed orientation. As the PA images provided no anatomical context due to their inherently poor soft tissue contrast, a combined PAUS imaging technique appears necessary for future clinical application.

In the angular dependence experiment, US imaging results are similar to those observed by Davis *et al.*, with the 0° orientation affording the greatest and most uniform acoustic signal [7]. This orientation maximizes the seed's surface area that is perpendicular to and within the path of the acoustic wave transmission, which maximizes backscattered energy. Because the seed becomes an acoustic source when excited by the PA effect, PA imaging yielded very similar rotation results. Due to the seed's capsular geometry, the directivity pattern of the acoustic energy emanating from the seed yields the greatest energy at points normal to the seed's cylindrical midsection. If evenly irradiated, acoustic energy will radiate outward from the seed body. This explains why only the proximal tip of the seed is well visualized in PA imaging as the distal tip, which is rotated away from the transducer face, will tend to transmit energy in the opposing direction.

In the bare seed spectrum experiment, the PA signal spectrum of a bare seed was found to monotonically decrease with increasing laser wavelength. Although the tested wavelength range extended beyond that covered in Fig. 1.1, the general trend of decreased absorption with increased wavelength observed in the spectrum for chromium-oxide (solid turquoise line) is consistent with the similar decrease in PA signal - which is proportional to optical absorption - observed in this study. When the seed was shallowly embedded in prostate tissue, however, the generated PA signal spectrum has local minima from 950 to 1010 nm. The phenomenon seen here is likely related to the "environmental" effect of the surrounding tissue (optical) properties on the seed's PA signal. Though the PA signal amplitude is directly related to the optical absorption coefficient of the metallic seed, local fluence is also dependent on the optical absorption and scattering coefficients of the surrounding tissue, resulting in a nonlinear dependence of the PA signal on tissue properties.

In the depth dependence results, contrast plots (Fig. 4.6d-f) were found to have local maxima at 1064 nm, with the deepest acquisition (13 mm) having its absolute maximum at this wavelength as well. Such a result is counter to what the results in the bare seed spectrum experiment might suggest should occur (i.e., given that the PA signal was greatest at 750 nm for the bare seed). In studies of human prostate, scattering has been identified as the dominant loss mechanism and has been found to decrease with increasing irradiation wavelength; this is typical for most soft tissues [14]. Though the optical absorption of metal also decreases with increasing wavelength, the reduction of

this absorption with increased wavelength is likely more modest than the decrease in local fluence that results from scattering at lower wavelengths. Given that the obtained PA signal is directly proportional to both optical absorption and local fluence, increasing imaging depth - which reduces local fluence but has no effect on optical absorption - appears to favor higher wavelengths. A local minimum in all of the spectra is observed at 990 nm, a phenomenon which is consistent with the more finely sampled spectrum (blue circle in Fig. 4.4a) acquired for the shallowly embedded seed and is likely a consequence of the trade-off between the absorption/scattering properties of the prostate tissue and the decreasing absorption of metal with increasing wavelength.

Contrast values obtained from the PA images of the seed in prostate tissue (Figs. 4.4b and 4.6d-f) highlight the importance of local fluence and seed orientation on seed visualization. Firstly, a significant decrease in contrast was observed from the 4-mm imaging depth (50.6 dB) to the 10-mm and 13-mm imaging depths (30.3 dB and 28.2 dB, respectively). This decrease is likely due to the drastic reduction in local fluence that results from increased scattering occurring through deeper interrogation regions; this notion is supported by over 90% reductions in PA signals for these deeper interrogations despite surface fluences that were comparable to those used for the shallower, 4-mm interrogation. Additionally, contrast appears to be affected by seed orientation. For the shallowly embedded seed that was imaged in the short-axis orientation (Fig. 4.5b), a 10.5-dB reduction in peak contrast was observed between it and the 4-mm, long-axis orientation (Fig. 4.6d). This reduction is due in large part to the nearly 50% reduction in

PA signal experienced with the rotation of the brachytherapy seed. Such a signal reduction - which also occurs but to a lesser extent for US imaging - would have resulted in US imaging slightly outperforming PA imaging (i.e., with theoretical contrasts of 24.3 dB and 22.9 dB, respectively) for the 13-mm acquisition had the seed been imaged in the short-axis orientation. For the 4-mm acquisition, theoretical contrast calculations suggest that PA imaging would have still outperformed US imaging had the seed been imaged in the short-axis orientation, with a slightly reduced contrast improvement (i.e., PA imaging over US imaging) of 24.4 dB (compared to a 27.9-dB improvement) being realized in this case. A study by Corbett *et al.* found, however, that the majority of seeds are placed approximately parallel (i.e., ±16°) to the transducer face during a clinical procedure [15]. Thus, although the case of short-axis imaging is an important one to consider, seeds tend to be oriented for optimal PA imaging. Ultimately, to obtain an appreciable contrast gain in any orientation and fully realize PA imaging's potential in this application, adequate local fluence at the seed location must be achieved.

As previously noted, it was not possible to image a brachytherapy seed at a depth of 17 mm in the prostate tissue sample due to insufficient local fluence. In an effort to increase local fluence in a clinical setting, a fiber optic-based light delivery system could be introduced through a patient's urethra. This would provide an additional irradiation source from within the tissue. With the urethra running through the prostate, maximum irradiation path lengths would be on the order of the prostate's radius (i.e., half the width or height dimension), which was found to have a mean of 21 mm in a study of men aged

52-67 years [4]. Consequently, as clinical application of this technology requires imaging beyond the 13 mm demonstrated herein, the use of higher energies and reduced tissue scattering at 1064 nm could be critical in an effort to achieve clinical utilization. In clinical settings, at 1064 nm the American National Standards Institute (ANSI) allows for maximum safe laser fluences of 100 mJ/cm^2 compared to 20 mJ/cm^2 at $\leq$700 nm when imaging through skin [16]. Although there is not currently a specific fluence regulation for irradiation through either the rectal or urethral wall, the aforementioned ANSI limit for skin is likely a conservative estimate for what would be allowed for this application given the relatively high absorption of skin (see Fig. 1.1). Based on this limit, a five-fold increase in surface fluence would be allowed in this study. Additionally, it might also be possible to increase local fluence by increasing the laser's pulse width. From a practical standpoint, the primary wavelength of an Nd:YAG laser is 1064 nm, making systems capable of imaging at this wavelength readily available and relatively inexpensive. The use of 1064 nm for molecular PA imaging is being pursued for similar reasons [17].

The rotation results from the first experiment demonstrate that PA imaging typically does not improve visualization of the full seed. When the seed is not approximately parallel to the transducer face, only the distal tip of the seed can be visualized with PA imaging, while both tips can be visualized with US imaging. The true improvement offered by PA imaging is in detecting and locating the seed, as evidenced by as much as a 27.9-dB increase in contrast. In a study by Corbett *et al.*, it was found that when multiple seeds are implanted, the placement of each seed is important in

achieving the intended radiation dose distribution while the orientation is not [15]. Thus, PA imaging's enhanced capability of visualizing the location of seeds could improve a clinician's ability to implement a specific treatment plan.

One source of experimental error from this study could have resulted from the irradiation source. The assumption was made that the surface area of the seed facing the ultrasound transducer was irradiated evenly. This was difficult to achieve for two reasons. Firstly, due to the experimental setup, the irradiation source was placed off-axis, which is not optimal for irradiation alignment with the obliquely positioned transducer face. Secondly, generation of a homogeneous beam profile across the seed surface is difficult when relatively high fluences must be maintained. These experimental issues would have been exacerbated in the experiments utilizing pure gelatin as a background material, while the turbid environment of prostate tissue would have mitigated these effects. A second source of error could have resulted from the use of five different prostate samples. Although the use of different samples lends more significance to certain multi-wavelength results (i.e., the existence of local minima and maxima at approximately 990 nm and 1064 nm, respectively), it could have also resulted in different depth-dependent scattering between samples.

4.5 CONCLUSION

PA imaging promises improved contrast of brachytherapy seeds in tissue, yielding improvements ranging from 2.7 to 27.9 dB in contrast over US imaging alone for seeds in the long-axis orientation and for imaging depths ranging from 4 to 13 mm. Even more

drastic than in US imaging, there is an angular dependence of a seed's PA signal, with the orientation having the greatest surface area normal to the acoustic beam direction resulting in the greatest PA signal. To achieve significant contrast improvements in a clinical application, which would call for imaging depths around 20 mm if a dual transurethral-transrectal irradiation source were implemented, greater laser energies at increased wavelengths (e.g., 1064 nm) will likely need to be utilized to obtain adequate local fluences. Nonetheless, combined PAUS imaging shows strong promise in accurately visualizing the seed and surrounding tissue anatomy during brachytherapy seed placement procedures.

4.6 REFERENCES

1. Jemal, A., R. Siegel, J. Xu, and E. Ward, *Cancer statistics, 2010.* CA: a cancer journal for clinicians, 2010. **60**(5): p. 277-300.

2. Nag, S., D. Beyer, J. Friedland, P. Grimm, and R. Nath, *American Brachytherapy Society (ABS) recommendations for transperineal permanent brachytherapy of prostate cancer.* International journal of radiation oncology, biology, physics, 1999. **44**(4): p. 789-99.

3. Wei, Z., M. Ding, D. Downey, and A. Fenster, *3D TRUS guided robot assisted prostate brachytherapy.* Medical image computing and computer-assisted intervention : MICCAI ... International Conference on Medical Image Computing and Computer-Assisted Intervention, 2005. **8**(Pt 2): p. 17-24.

4. Hricak, H., R.B. Jeffrey, G.C. Dooms, and E.A. Tanagho, *Evaluation of prostate size: a comparison of ultrasound and magnetic resonance imaging.* Urologic radiology, 1987. **9**(1): p. 1-8.

5. Van Gellekom, M.P., M.A. Moerland, J.J. Battermann, and J.J. Lagendijk, *MRI-guided prostate brachytherapy with single needle method--a planning study.* Radiotherapy and oncology : journal of the European Society for Therapeutic Radiology and Oncology, 2004. **71**(3): p. 327-32.

6. Xue, J., F. Waterman, J. Handler, and E. Gressen, *Localization of linked 125I seeds in postimplant TRUS images for prostate brachytherapy dosimetry.* International journal of radiation oncology, biology, physics, 2005. **62**(3): p. 912-9.

7. Davis, B.J., R.R. Kinnick, M. Fatemi, E.P. Lief, R.A. Robb, and J.F. Greenleaf, *Measurement of the ultrasound backscatter signal from three seed types as a function of incidence angle: application to permanent prostate brachytherapy.* International journal of radiation oncology, biology, physics, 2003. **57**(4): p. 1174-82.

8. Han, B.H., K. Wallner, G. Merrick, W. Butler, S. Sutlief, and J. Sylvester, *Prostate brachytherapy seed identification on post-implant TRUS images.* Medical physics, 2003. **30**(5): p. 898-900.

9. Nath, S., Z. Chen, N. Yue, S. Trumpore, and R. Peschel, *Dosimetric effects of needle divergence in prostate seed implant using 125I and 103Pd radioactive seeds.* Medical physics, 2000. **27**(5): p. 1058-66.

10. Xu, M. and L.V. Wang, *Photoacoustic imaging in biomedicine.* Review of Scientific Instruments, 2006. **77**(4): p. 041101-22.

11. Su, J.L., A.B. Karpiouk, B. Wang, and S.Y. Emelianov, *Photoacoustic imaging of clinical metal needles in tissue.* Journal of Biomedical Optics, 2010. **15**(2): p. 021309-6.

12. Nag, S., J.P. Ciezki, R. Cormack, S. Doggett, K. DeWyngaert, G.K. Edmundson, R.G. Stock, N.N. Stone, Y. Yu, and M.J. Zelefsky, *Intraoperative planning and evaluation of permanent prostate brachytherapy: report of the American Brachytherapy Society.* International journal of radiation oncology, biology, physics, 2001. **51**(5): p. 1422-30.

13. Lee, E.K. and M. Zaider, *Intraoperative dynamic dose optimization in permanent prostate implants.* International journal of radiation oncology, biology, physics, 2003. **56**(3): p. 854-61.

14. Svensson, T., E. Alerstam, M. Einarsdottir, K. Svanberg, and S. Andersson-Engels, *Towards accurate in vivo spectroscopy of the human prostate.* Journal of biophotonics, 2008. **1**(3): p. 200-3.

15. Corbett, J.F., J.J. Jezioranski, J. Crook, T. Tran, and I.W. Yeung, *The effect of seed orientation deviations on the quality of 125I prostate implants.* Physics in medicine and biology, 2001. **46**(11): p. 2785-800.

16. American National Standards Institute *ANSI Z136.1-2007 American national standards for safe use of lasers*. 2007.

17. Homan, K., S. Kim, Y.S. Chen, B. Wang, S. Mallidi, and S. Emelianov, *Prospects of molecular photoacoustic imaging at 1064 nm wavelength.* Optics letters, 2010. **35**(15): p. 2663-5.

Chapter 5: Photoacoustic Imaging of Coronary Arterial Stents

5.1 Clinical Relevance

Coronary stents are currently the most widely used coronary intervention in the United States. While the procedure is more than 95% successful [1], stents have brought along several unique issues including restenosis, hyperplasia and stent drift. The ability to visualize stents both during the stenting procedure and during post-surgery follow-up is important in order to correctly assess the stent with respect to the plaques and vessel, and also identify its apposition within the vessel wall. Immediately following a stenting procedure, it is important to determine the relation of the stent struts to the vessel wall. Ideally, the stent is deployed in contact with the lumen wall; however, malapposition can occur resulting in the stent detaching itself from the wall. This detachment can cause turbulent eddies to form in the vessel which can lead to thrombosis in the area of the stent. It is important when monitoring the stent to determine how much restenosis has formed around the stent struts. The distance that the stent struts are embedded into the vessel wall must be determined to assess stent viability. Currently, the most common method for assessing stent position is x-ray coronary angiography/fluoroscopy [2]. However, this procedure is problematic due to its use of ionizing radiation and possible complications in using iodinated contrast agents. Furthermore, x-ray fluoroscopy can only depict a two-dimensional projection which can lead to an underestimation of lumen diameter and the stent apposition within the lumen.

Magnetic resonance imaging has been used to image stents due to its avoidance of radiation exposure and iodine contrast agents; however, the metallic composition of stents can cause susceptibility artifacts which can obscure the stent lumen and make it very difficult to visualize the relation between the stent and the vessel wall [1, 3]. Long scan times and low resolution also remain a major limitation. Multi-slice computed tomographic angiography (MSCTA) has been shown to image much faster than MRI; however, its low resolution and artifacts in metallic stents make assessing the surrounding vessel difficult [4].

Both intravascular ultrasound (IVUS) and optical coherence tomography (OCT) have reached widespread usage in catheterization labs. IVUS can detect signal reflections from the stent struts, but has insufficient contrast to determine the struts' position against the vessel wall [5]. Ultrasound contrast of stents is affected by the background tissue environment, which is also acoustically scattering. In addition, extraneous beams of ultrasound generated by the ultrasound transmit pulse and then scattered by the metallic stents will obscure the edges of the stent borders [6]. These blurred edges are image artifacts that can reduce the spatial registration of the imaged stent. OCT directly competes with these disadvantages with a resolution of 10-20 μm but has severe depth limitations, allowing only a penetration depth of about 2 mm [7, 8]. The presence of blood flowing through the vessel limits this depth even further, requiring clinicians to flush the vessel during the imaging procedure [5, 9]. Furthermore, the tissue behind the

stent strut becomes hidden due to scattering shadows in OCT, which prevents complete diagnosis of the stent's relation to the vessel lumen [5].

To counteract these disadvantages, we introduce a combined intravascular photoacoustic and intravascular ultrasound (IVPA/IVUS) based method for imaging clinical off-the-shelf stents with sufficient contrast, resolution, and depth penetration to visualize the stent and surrounding tissue [10]. In photoacoustic imaging the tissue is irradiated by a short laser pulse to produce a small thermal expansion and acoustic response. The light absorbed in a specific local region is converted into heat, and then converted into pressure due to the thermoelastic expansion of the tissue. An ultrasound transducer detects the produced pressure, which is linearly related to the optical absorption coefficient and the localized laser fluence. Therefore, photoacoustic imaging – a technology for remote assessment of optical absorption at sufficient depth, has all the prerequisites to become a diagnostic tool capable of providing morphological and functional information of the blood vessel [11]. Moreover, spectroscopic IVPA/IVUS imaging has shown its potential to differentiate the tissue composition in atherosclerotic plaques [12]. Thus, besides imaging stents, the same technology may be used to assess the type of tissue near the stent.

In this paper, we demonstrate the ability of IVUS and IVPA to image deployed coronary stents. Experiments were performed using commercial stents embedded into vessel-mimicking phantoms. The off-the-shelf stents were visualized quantitatively allowing for accurate measurements of stent position within the vessel. The accuracy of

these measurements suggests that photoacoustic imaging of various types of metal implants embedded into tissue is possible.

5.2 MATERIALS/METHODS

To test the feasibility of IVUS/IVPA to image stents, imaging studies were performed using 33 mm length, BX Velocity™ stents (Cordis) [13] deployed in two vessel phantoms mimicking both acoustic and optical scattering properties of tissue. Both phantoms were about 25 mm long with 10 mm outer diameter made of 8% polyvinyl alcohol (PVA). As prepared, PVA is an optically scattering material. For acoustic contrast, 0.1% by weight silica particles of 5 μm size were added to the phantom material to act as ultrasound scatterers.

The first phantom simulated an atherosclerotic vessel with a 3 mm inner diameter. The BX Velocity™ stent was embedded 1 mm into the inner lumen of the vessel, completely encased within the lumen wall (Fig. 5.1). Eight millimeters of the stent protruded from one end of the phantom.

The second vessel phantom consisted of three different regions where the stent, relative to the inner lumen, was embedded, deployed (adjacent to the vessel wall), and malapposed (detached from the vessel wall) (Fig. 5.2). In this phantom, the stent was embedded approximately 1.0 mm within the vessel wall, directly adjacent to the wall, and approximately 1.0 mm malapposed from the vessel wall in the lumen in the different regions, respectively. The malapposed region was formed by separating the stent from the PVA with a plastic mold. Although the stent was separated from the PVA vessel, the

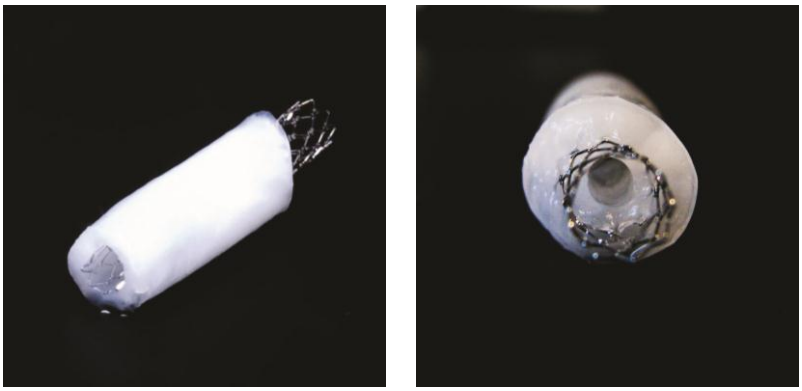

Figure 5.1: Photographs of the first vessel mimicking phantom with a stent embedded in the lumen wall. A 5.0 mm inner diameter stainless steel stent was molded 1 mm deep within the vessel wall from the lumen. An 8 mm long region of the stent was left bare outside of the phantom vessel, which was constructed from 8% cross-linked polyvinyl alcohol (PVA).

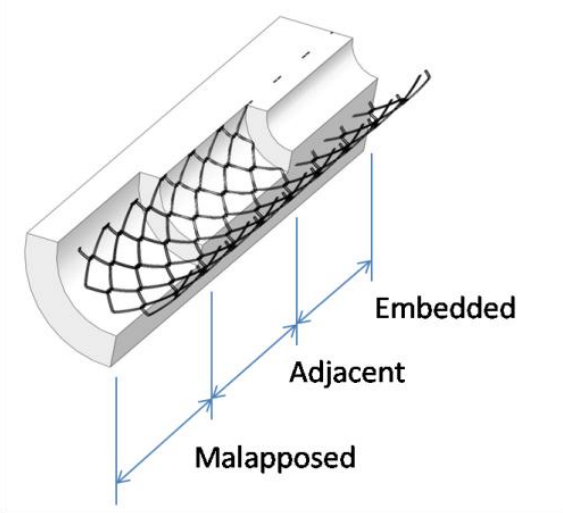

Figure 5.2: Cut-away diagram of the second vessel phantom consisting of three regions of varying distances between the stent and the vessel wall to model embedded (within the vessel wall), deployed (adjacent to the vessel wall), and malapposed (separate from the vessel wall) stents.

stent itself was covered with a thin film of PVA due to the molding process during the phantom preparation.

The laboratory prototype of the IVUS/IVPA imaging setup is shown in Fig. 5.3. Briefly, a tunable pulsed Nd:YAG pumped optical parametric oscillator laser system (Vibrant B, Opotek, Inc.) was used at 800 nm wavelength to optically illuminate the vessel phantom (Fig. 3a). The photoacoustic signal was detected by a 40 MHz IVUS imaging catheter (2.5 French, Atlantis™ SR Plus, Boston Scientific, Inc) which was placed within the lumen of the PVA phantom. The laser beam and the IVUS sensing element were first aligned prior to the experiment to ensure detectibility of the photoacoustic response from the phantom. In addition to collecting photoacoustic signals, ultrasound pulse-echo signals were also collected using the IVUS imaging catheter connected to an ultrasound pulser/receiver. The cross-sectional IVUS and IVPA images were obtained by rotating the vessel and acquiring 256 photoacoustic/ultrasound A-lines. By longitudinally incrementing the phantom 248 μm each frame, a series of 100 cross-sectional images was collected to reconstruct a three dimensional image of the phantom.

In this ex-vivo prototype imaging setup, external light delivery is unrealistic for in-vivo imaging (Fig. 5.3b). During an in-vivo IVPA imaging procedure using the integrated IVUS/IVPA imaging catheter [14], light would be fed into the vessel using a fiber optical delivery system (Fig. 5.3c) where optical absorption and scattering of blood will diminish the incident laser fluence on the vessel lumen and stent. Therefore, to maximize light penetration at a given fluence and obtain sufficient image contrast, we

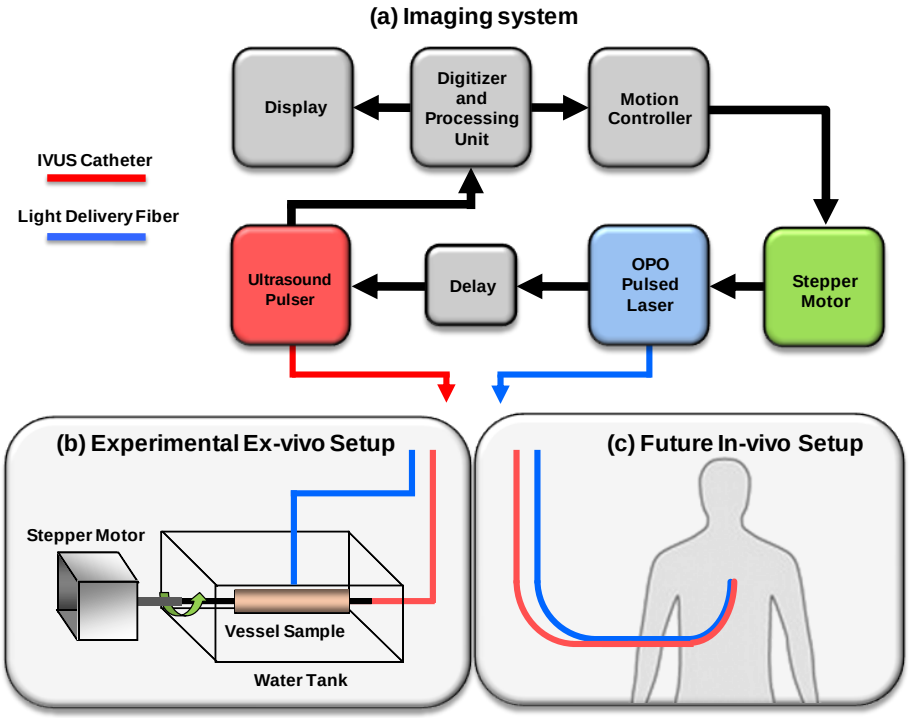

Figure 5.3: (a) Overall IVUS/IVPA imaging system. (b) Ex-vivo prototype photoacoustic imaging setup: the vessel was placed in a water tank and externally illuminated using an optical fiber. The ultrasound imaging catheter is placed inside the lumen and the vessel was rotated incrementally as IVUS/IVPA A-lines were collected. (c) Diagram of the integrated IVUS/IVPA imaging catheter where the IVUS probe and fiber-optical light delivery system are combined for in-vivo intravascular imaging.

used light at 800 nm wavelength. At this range, blood is more optically scattering than it is optically absorbing [15]. To mimic this scattering media, milk was substituted for the 30 cm^{-1} scattering coefficient of oxygenated blood at 800 nm. The tip of the optical fiber was placed 5 mm away from the surface of the vessel to simulate the in-vivo IVUS/IVPA imaging where light would travel through blood (scattering environment) before reaching the vessel wall. Therefore, it is conjectured that photoacoustic images of the phantom submersed into milk will be affected by light scattering similar to in-vivo imaging.

A third experiment was conducted to test the imaging and detection of stent in a more realistic environment. An excised aorta from a rabbit model of atherosclerosis was used. In particular, a New Zealand white rabbit was kept under a low 0.2% cholesterol diet for 12 months. Rabbits under these dietary situations can develop severe atherosclerotic lesions in the aorta [16]. The rabbit was sacrificed and the aorta was excised. A 4.5 mm inner diameter BX Velocity™ stent (Cordis) was deployed into the excised aorta according to the manufacturer recommended pressure rating. The stent was inflated to a pressure of approximately 12-14 atm, which resulted in an inflated diameter of approximately 4.64 - 4.76 mm. Combined US and PA imaging was performed with a custom designed integrated catheter [17] inserted into the lumen of the excised artery in a water tank. Spectroscopic PA imaging was performed from 650-710 nm and from 750-900 nm, in increments of 10 nm. Laser fluence was measured at each pulse and used to normalize the PA signal in post-processing.

Images were processed using custom Matlab code written to process and display

the scan-converted IVUS/IVPA images. For quantitative analysis, the PA signal was taken from a small kernel corresponding to an area where one stent strut located, and confirmed based on the B-mode image. Data within this kernel was averaged to obtain a signal value for the center pixel. Data values were recorded across all wavelengths to obtain a rough optical spectrum from 650 to 900 nm. This spectrum was then correlated to all other pixels in the image, taking into account the PA data obtained across all the wavelengths. Correlation values for each pixel were then overlaid in an image over the original PA image.

5.3 RESULTS

The cross-sectional ultrasound image (40 dB display dynamic range) and photoacoustic image (15 dB range) of the first vessel phantom with the stent are shown in Fig. 5.4. The photoacoustic image shows very high contrast between the stent and the background. Indeed, photoacoustic signal from the stent struts is very strong due to the high optical absorption of metal compared to the vessel which has little to no photoacoustic response. By comparison, the ultrasound image visualizes the complete cross-section of the vessel including the structure and thickness variation of the vessel wall. Since the ultrasound and photoacoustic images are already spatially co-registered, combining the two images shows complementary information. The location of the stent (IVPA image) is given in relation to the vessel (IVUS image). Quantitatively, the radial distance from individual struts to the lumen wall, measured from the IVUS/IVPA image, varied between 0.7 to 1.2 mm. These measurements are in agreement with the design of

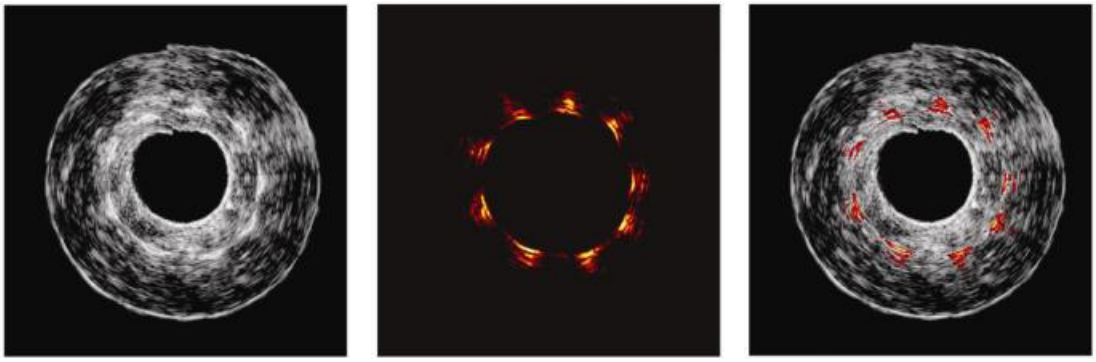

Figure 5.4: (a) Ultrasound (IVUS) and (b) photoacoustic (IVPA) cross-sectional images of the stent deployed within the vessel phantom. (c) Overlay of the two images together shows the position of the stent struts with respect to the thickness of the vessel wall.

the phantom – the phantom mold was milled to separate the lumen wall from the stent by approximately 1.0 mm. To visualize the entire vessel wall and the stent, a three-dimensional (3D) image of the phantom was produced (Fig. 5.5). To visualize the structure of the stent in the context of the structure of the phantom, the transparency of the ultrasound image was modified such that the photoacoustic signal can be seen, showing the structure of the stent.

The intravascular ultrasound, photoacoustic and combined IVUS/IVPA images of the second vessel phantom are shown in Fig. 5.6. By imaging at various locations along the length of the vessel, the distance between the stent and the lumen wall was assessed. In the region of the embedded stent (Fig. 5.6a), the distance of the stent struts to the lumen wall was measured to range from 0.7 to 1.0 mm. In the region where the stent was merely adjacent to the vessel wall (Fig. 5.6b), the image visualized the correct position of the stent struts relative to the vessel wall. Finally, in the malapposed region (Fig. 5.6c) the stent struts were measured to be 0.8 to 1.1 mm away from the wall. The position of the stent struts varied due to preparation of the PVA phantom mold. However, the diameter of the stent was measured to be a constant 5.0 mm throughout the entire stent, in agreement with the specification set out by the manufacturer. Due to the molding process used in fabricating the malapposed section (Fig. 5.6c), a thin layer of PVA was formed on the surface of the stent. The presence of this PVA film explains the additional inner ring where the stent is located. Nevertheless, IVPA imaging was unaffected. The images in

Fig. 5.6c demonstrate that far more complex geometries and positioning of stents within the vessel can be imaged using IVUS/IVPA imaging.

Similar to the first phantom, a set of 80 cross-sectional images were combined to produce a 3D image of the vessel and stent (Fig. 5.7). By displaying the cut-away of the 3D reconstruction, the shape and position of the stent within the vessel is easily assessed (Fig. 5.7d). Again, the photoacoustic image was able to visualize the stent (Fig. 5.7b) and to correctly measure the inner diameter of the stent to be exactly 5.0 mm, the reported diameter for the stent. Furthermore, the stent could be visualized in the context of the vessel geometry (Fig. 5.7c) to identify the regions of embedded, deployed, and malapposed stent (Fig. 5.7d).

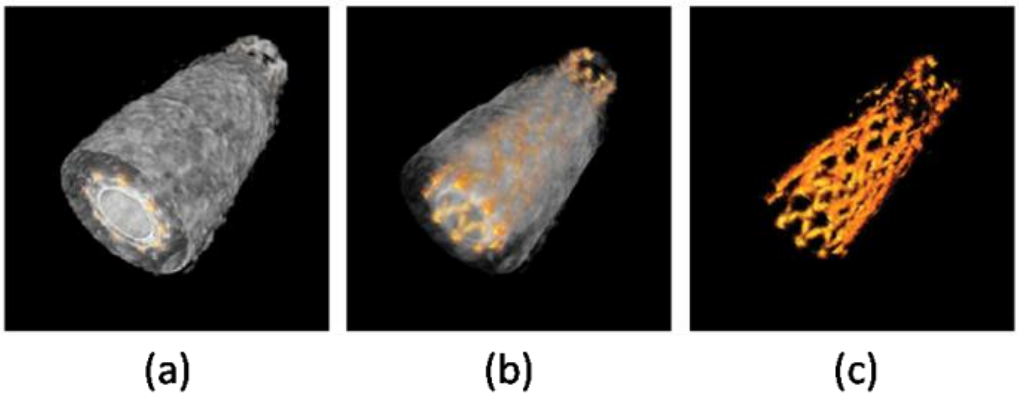

Figure 5.5: Three-dimensional (3D) reconstruction of the vessel and stent. The 3D image was created by acquiring a stack of cross-sectional images and combining them together. The ultrasound and photoacoustic signals can be displayed with different transparency in the reconstructed image to show the position and shape of the stent within the vessel.

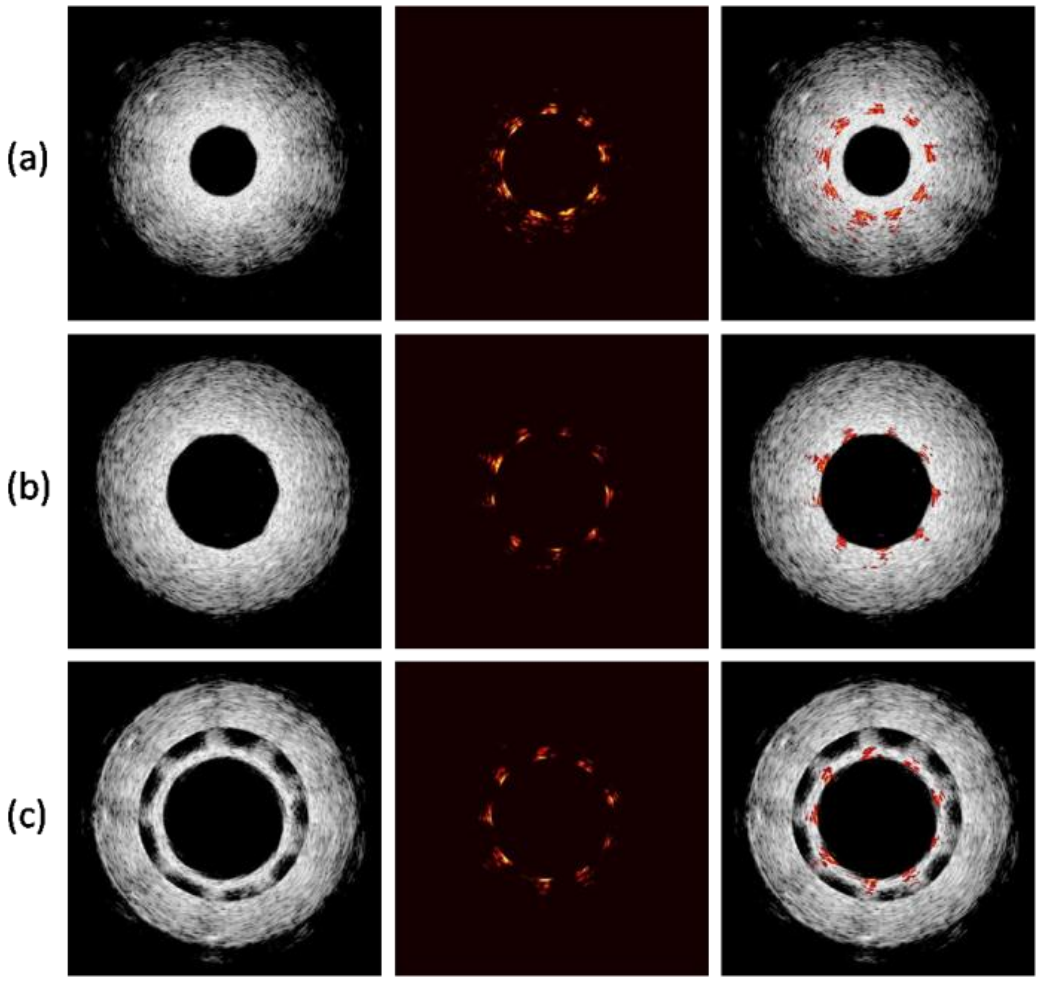

Figure 5.6: Intravascular ultrasound and photoacoustic and combined IVUS/IVPA images from the three different regions in the stented vessel. (a) Stent embedded within the vessel. (b) Stent adjacent to lumen wall. (c) Stent detached from lumen wall.

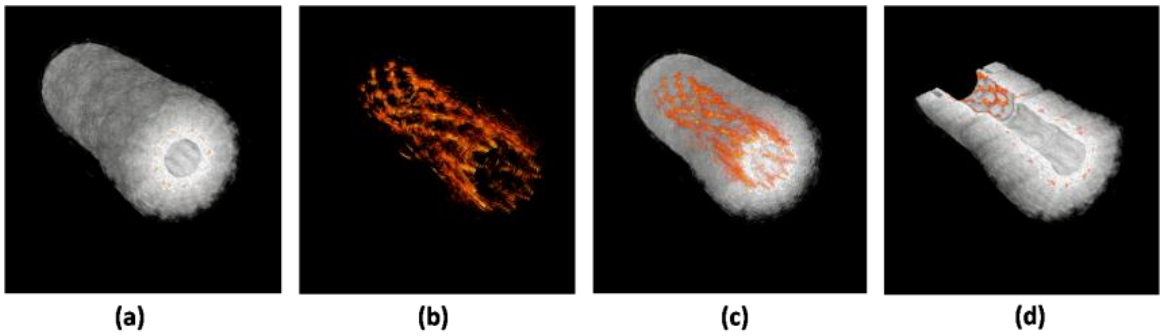

Figure 5.7: 3D-reconstruction of the tri-sectional phantom. Individual cross sections can show the position of the stent within the vessel. (a) Ultrasound 3D reconstruction of the phantom showing the structure of the vessel. (b) Photoacoustic reconstruction of the stent structure which can be used to assess the condition of the stent. (c) Photoacoustic image of the stent overlaid with the ultrasound image of the vessel can show the position of both. (d) Cut-away image of the reconstruction, allowing for accurate assessment of the stent within the vessel.

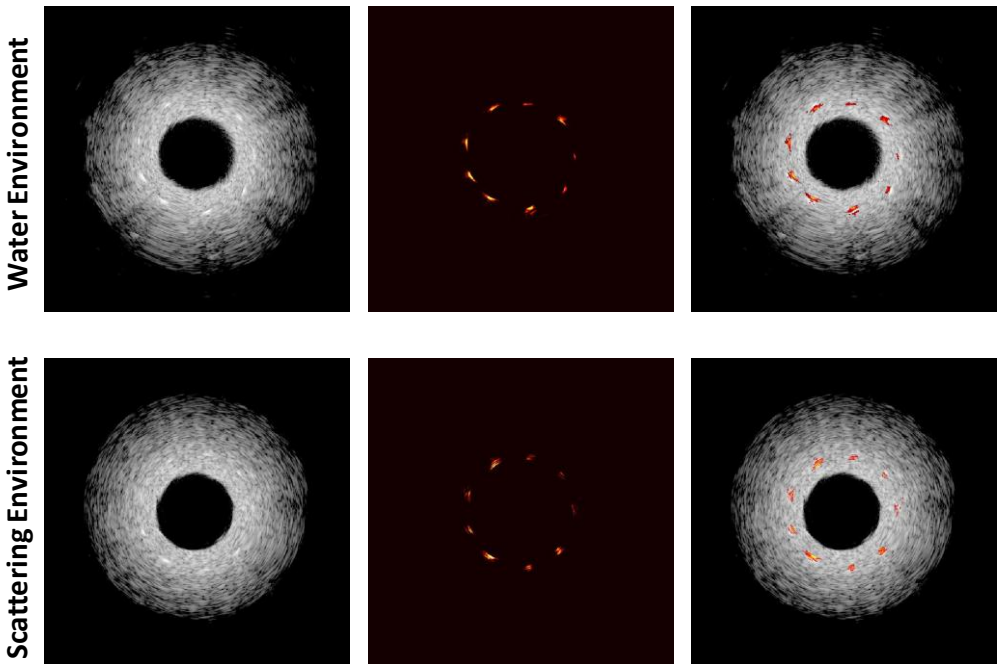

Figure 5.8: IVUS/IVPA imaging of vessel-mimicking phantom in transparent (i.e. non-scattering) and scattering medium. Ultrasound images displayed at 55 dB. Photoacoustic images in water and scattering medium displayed at 15 dB and 10 dB, respectively.

The experiments were also performed to identify the influence of luminal blood on the quality of photoacoustic imaging. The comparison between the blood-simulating environment and the water environment showed virtually no difference in either the ultrasound or photoacoustic images (Fig. 5.8). As expected, photoacoustic signal intensity showed a small reduction in the peak signal intensity from the stent due to the optical scattering properties of the milk. Nevertheless, image quality was not significantly reduced – the stent within the vessel wall was clearly visualized in both images.

Finally, images were acquired from the experiment using a combined IVUS/IVPA catheter to image a stent deployed in an excised rabbit aorta (Fig. 5.9). Similar to the previous phantom studies, the stent struts appeared with high contrast in the PA images (Fig. 5.9b). The combined US and PA image showed good co-registration regarding the presence and location of the stent struts for half of the cross-section. The stent struts in the image from the 6 o'clock to 11 o'clock position were less visible in the image, but the comet-tail artifacts from each stent strut could still be seen.

Spectroscopic analysis was also able to identify the presence of the stent based on the unique multi-wavelength PA signal of the metal (Fig 5.10). The location of the stent struts as seen in the PA images showed good correlation with the spectrum of the original selected kernel. Each pixel was displayed according to a colorbar (Fig 5.10a), with high correlation pixels displayed in red, and low correlation in blue. It was observed that the comet-tail artifacts that appeared distal to each stent strut did not correlate well with the

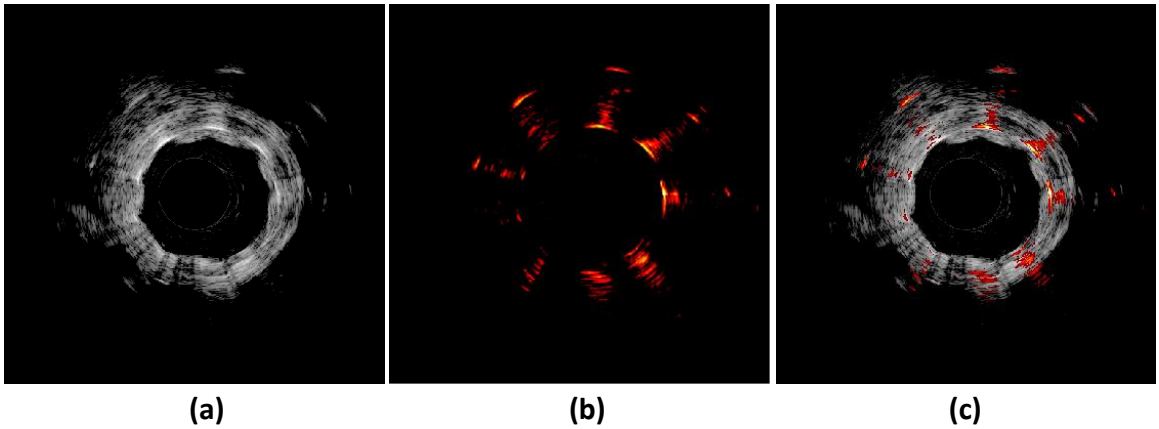

Figure 5.9: (a) Ultrasound (IVUS) and (b) photoacoustic (IVPA) cross-sectional images of the stent deployed within an excised rabbit artery. (c) Overlay of the two images together shows the position of the stent struts with respect to the thickness of the vessel wall. US and PA images are displayed at 55dB and 25 dB, respectively.

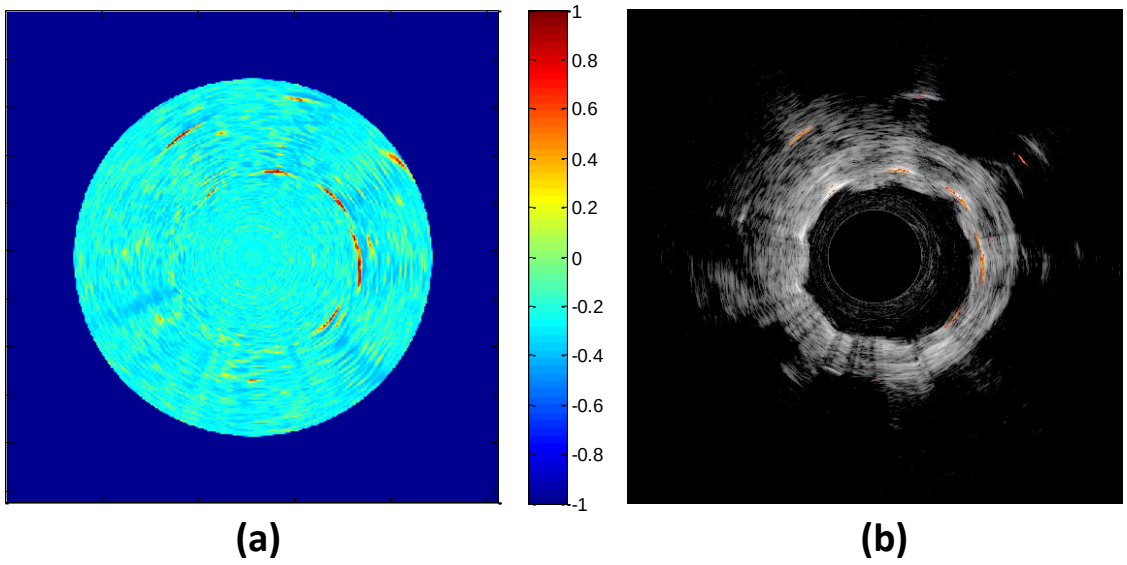

Figure 5.10: (a) Correlation colormap based on multi-wavelength PA data obtained across multiple wavelengths. (b) Correlation coefficients greater than 80% are then displayed overlaid on the US cross-sectional image.

original kernel. Finally, pixels that showed a correlation coefficient greater than 80% were overlaid on the US image (Fig 5.10b).

5.4 Discussion and Conclusions

The combined IVUS and IVPA imaging system was able to image several millimeters deep which is necessary for the intravascular imaging of coronary arteries. The high-frequency 40 MHz IVUS catheter allowed for an axial resolution of several tens of micrometers in both IVUS and IVPA images [10]. The resolution of IVUS/IVPA imaging is slightly worse compared to OCT imaging, but the larger imaging depth allowed for complete viewing of the 10 mm diameter vessel. Furthermore, the full structure of the phantom is visible, unobscured behind the stent struts, thus allowing the position of the stent within the vessel wall to be visible, whether or not the stent was hidden from view.

Overall, the diameter of the stent was correctly measured throughout the stent according to the specification set out by the manufacturer. An in-vivo environment can cause implanted stents to be crushed or deformed which can lead to problems such as thrombosis or stent drift. Photoacoustic imaging allows for accurate assessment of not only the size of the stent but also the stent shape in relation to the implanted environment.

The stent struts were always fully visible in the photoacoustic image, but at best only partially visible in the ultrasound images. In these regions visible in ultrasound, the phantom background is hypoechoic and therefore the stent appears in the ultrasound image with sufficient contrast against this background. In the phantoms used in this experiment, silica particles were added to provide acoustic scattering. Regions that did

not contain uniformly mixed silica particles appeared hypoechoic under ultrasound. However, under conditions where the local background regions were highly acoustically scattering, the stent was difficult to visualize under ultrasound alone. Even in the malapposed region of the phantom (Fig. 5.6c) where traces of the stent struts can be seen, the presence of the PVA film reduced the ability to locate the struts using ultrasound alone. In the photoacoustic image, conversely, the contrast is determined by optical absorption. Since metal struts of the stent are strong light absorbers, the photoacoustic image revealed the precise location of the metal struts. Since IVPA imaging is based on the same hardware as IVUS, it is understandable that photoacoustic imaging of stents may be susceptible to similar artifacts seen in IVUS. These include artifacts due to off-centered positioning of the transducer within the lumen and acoustic reverberation artifacts within the metal stent implant. IVPA can also bring its own issues, including light delivery through tissue or through other optically attenuating materials.

The optical attenuation of light in blood should not detrimentally affect imaging of stents in-vivo. In our experiment, the optic fiber was placed at a greater distance from the vessel surface than it would be from the inner boundary of the vessel wall in in-vivo imaging. In other words, in in-vivo experiments the light would travel a smaller distance and be attenuated less. Therefore, the resulting images in-vivo should be able to assess stent viability. Furthermore, laser pulse energies in our experiments, measured at the fiber output, were approximately 1.75 mJ. Due to the high optical absorption properties of metals, the energy used to obtain a photoacoustic response can be decreased. For IVPA imaging in real-time, necessary in the clinical environment, lower energies may be

required to increase the laser pulse repetition rates. For these applications, a tunable OPO laser system may not be a suitable choice. However, pulsed Nd:YAG lasers operating at 1064 nm could be considered as these lasers can have pulse repetition rates from 1-10 kHz. While the pulse energy of these lasers is only upwards of 100 μJ, fluences similar to this experiment could be obtained by decreasing the fiber size or focusing the laser beam to a smaller diameter. It should be noted that smaller fiber sizes will undoubtedly be required in a clinical IVUS/IVPA system in order to meet lumen clearance diameters for the combined imaging catheter containing the IVUS transducer and IVPA optical fiber.

From the ex-vivo tissue images, the stent struts were highly visible in the PA images. Each strut from the 12 o'clock to 6 o'clock position produced a strong PA signal, but also a trailing comet-tail artifact similar to those seen in needles [18, 19]. Spectroscopic PA imaging demonstrated the ability to isolate the signal from the metal stent strut from its associated comet-tail artifact. This procedure shows that the amplitude of the comet-tail artifact produced is not linearly proportional to the optical absorption of metal. Multi-wavelength PA imaging could possibly be used as a process to filter out the comet-tail artifact, therefore isolating only the PA signal from the stent strut.

However, the absence of strong PA signals from the 6 o'clock to 11 o'clock positions in Fig 5.9b, highlight an instrumentation issue rather than a fundamental limitation. For the combined IVUS/IVPA catheter used here, the optical and acoustic beams were only overlapped at a certain imaging depth, due to the construction of the catheter. Therefore, tissue/struts that were not located at this imaging depth did not produce good photoacoustic signal. Future improvements of combined IVUS/IVPA

catheters should characterize this imaging depth better, in order to better visualize the entire cross-section of the coronary artery.

The use of IVUS and IVPA for imaging stents is a natural progression since IVUS/IVPA has been shown to detect and differentiate fatty plaques in atherosclerotic coronary arteries. Coronary stents are commonly used to treat blood vessels that have narrowed due to the presence of vulnerable plaques. Recent studies have shown that stent positioning can drift over time, leading to the need to detect stent shape and location with respect to the site of atherosclerosis while also determining the progression of plaque vulnerability. This makes the combined IVUS/IVPA imaging a natural and feasible method in the diagnosis and treatment of atherosclerosis. This initial study shows that IVUS/IVPA is a promising modality to image stents in vivo.

5.5 REFERENCES

1. Maintz, D., R.M. Botnar, R. Fischbach, W. Heindel, W.J. Manning, and M. Stuber, *Coronary magnetic resonance angiography for assessment of the stent lumen: a phantom study.* J Cardiovasc Magn Reson, 2002. **4**(3): p. 359-67.

2. Elgort, D.R., C.M. Hillenbrand, S. Zhang, E.Y. Wong, S. Rafie, J.S. Lewin, and J.L. Duerk, *Image-guided and -monitored renal artery stenting using only MRI.* J Magn Reson Imaging, 2006. **23**(5): p. 619-27.

3. Hug, J., E. Nagel, A. Bornstedt, B. Schnackenburg, H. Oswald, and E. Fleck, *Coronary arterial stents: safety and artifacts during MR imaging.* Radiology, 2000. **216**(3): p. 781-7.

4. Maintz, D., K.U. Juergens, T. Wichter, M. Grude, W. Heindel, and R. Fischbach, *Imaging of coronary artery stents using multislice computed tomography: in vitro evaluation.* Eur Radiol, 2003. **13**(4): p. 830-5.

5. Kawase, Y., K. Hoshino, R. Yoneyama, J. McGregor, R.J. Hajjar, I.K. Jang, and M. Hayase, *In vivo volumetric analysis of coronary stent using optical coherence tomography with a novel balloon occlusion-flushing catheter: a comparison with intravascular ultrasound.* Ultrasound Med Biol, 2005. **31**(10): p. 1343-9.

6. Mintz, G.S., S.E. Nissen, W.D. Anderson, S.R. Bailey, R. Erbel, P.J. Fitzgerald, F.J. Pinto, K. Rosenfield, R.J. Siegel, E.M. Tuzcu, and P.G. Yock, *American College of Cardiology Clinical Expert Consensus Document on Standards for Acquisition, Measurement and Reporting of Intravascular Ultrasound Studies (IVUS). A report of the American College of Cardiology Task Force on Clinical Expert Consensus Documents.* J Am Coll Cardiol, 2001. **37**(5): p. 1478-92.

7. Barlis, P., K. Dimopoulos, J. Tanigawa, E. Dzielicka, G. Ferrante, F. Del Furia, and C. Di Mario, *Quantitative analysis of intracoronary optical coherence tomography measurements of stent strut apposition and tissue coverage.* Int J Cardiol, 2009.

8. Slottow, T.L., R. Pakala, T. Okabe, D. Hellinga, R.J. Lovec, F.O. Tio, A.B. Bui, and R. Waksman, *Optical coherence tomography and intravascular ultrasound imaging of bioabsorbable magnesium stent degradation in porcine coronary arteries.* Cardiovasc Revasc Med, 2008. **9**(4): p. 248-54.

9. Jang, I.K., B.E. Bouma, D.H. Kang, S.J. Park, S.W. Park, K.B. Seung, K.B. Choi, M. Shishkov, K. Schlendorf, E. Pomerantsev, S.L. Houser, H.T. Aretz, and G.J. Tearney, *Visualization of coronary atherosclerotic plaques in patients using*

optical coherence tomography: comparison with intravascular ultrasound. J Am Coll Cardiol, 2002. **39**(4): p. 604-9.

10. Sethuraman, S., S.R. Aglyamov, J.H. Amirian, R.W. Smalling, and S.Y. Emelianov, *Intravascular photoacoustic imaging using an IVUS imaging catheter.* IEEE Trans Ultrason Ferroelectr Freq Control, 2007. **54**(5): p. 978-86.

11. Sethuraman, S., J.H. Amirian, S.H. Litovsky, R.W. Smalling, and S.Y. Emelianov, *Ex vivo Characterization of Atherosclerosis using Intravascular Photoacoustic Imaging.* Opt Express, 2007. **15**(25): p. 16657-66.

12. Sethuraman, S., J.H. Amirian, S.H. Litovsky, R.W. Smalling, and S.Y. Emelianov, *Spectroscopic intravascular photoacoustic imaging to differentiate atherosclerotic plaques.* Opt Express, 2008. **16**(5): p. 3362-7.

13. Butany, J., K. Carmichael, S.W. Leong, and M.J. Collins, *Coronary artery stents: identification and evaluation.* J Clin Pathol, 2005. **58**(8): p. 795-804.

14. Wang, B., A.B. Karpiouk, and S.Y. Emelianov, *Design of catheter for combined intravascular photoacoustic and ultrasound imaging.* Proceedings of the 2008 IEEE Ultrasonics Symposium, 2008: p. 1150-1153.

15. Faber, D.J., M.C. Aalders, E.G. Mik, B.A. Hooper, M.J. van Gemert, and T.G. van Leeuwen, *Oxygen saturation-dependent absorption and scattering of blood.* Phys Rev Lett, 2004. **93**(2): p. 028102.

16. Kolodgie, F.D., A.S. Katocs, Jr., E.E. Largis, S.M. Wrenn, J.F. Cornhill, E.E. Herderick, S.J. Lee, and R. Virmani, *Hypercholesterolemia in the rabbit induced by feeding graded amounts of low-level cholesterol. Methodological considerations regarding individual variability in response to dietary cholesterol and development of lesion type.* Arteriosclerosis, thrombosis, and vascular biology, 1996. **16**(12): p. 1454-64.

17. Karpiouk, A.B., B. Wang, and S.Y. Emelianov, *Development of a catheter for combined intravascular ultrasound and photoacoustic imaging.* The Review of scientific instruments, 2010. **81**(1): p. 014901.

18. Ziskin, M.C., D.I. Thickman, N.J. Goldenberg, M.S. Lapayowker, and J.M. Becker, *The comet tail artifact.* J Ultrasound Med, 1982. **1**(1): p. 1-7.

19. Su, J.L., A.B. Karpiouk, B. Wang, and S.Y. Emelianov, *Photoacoustic imaging of clinical metal needles in tissue.* Journal of Biomedical Optics, 2010. **15**(2): p. 021309-6.

Chapter 6: Future Work

In the previous chapters, three examples of clinical metal implants in need of image-guidance were described. Each example demonstrated that proper visualization of *both* the metal implant and the identification of the tissue characteristics must be accurately made to confirm optimum delivery of therapy. In response to the urgent clinical need for a robust metal and adjacent tissue imaging technique, the overall goal of this work was to design and develop a photoacoustic imaging technique for metal implants. Additional studies are needed to test the viability of this imaging technique in-vivo, as well as to meet the additional goal of characterizing tissue composition in order to more accurately guide and monitor these metal implants.

6.1 Detection of Surrounding Tissue Composition

Studies have shown that the amplitude of the received photoacoustic signal is affected by the surrounding environment of the absorber. This environmental dependence is seen in the dimensionless Grüneisen coefficient, Γ, as illustrated by Equation 1.1 and 1.2. Preliminary studies were conducted based on photoacoustic imaging of needles to determine whether or not significant amplitude changes could be seen based on tissue composition environment.

6.1.1 Materials and Methods

To examine how the environment contributes to the PA signal, a metal needle was inserted superficially along the surface of fresh porcine tissue. Three-dimensional

ultrasound images were used to verify that the needle was indeed completely embedded within the tissue but less than 1.0 mm below the surface of the tissue. The tissue sample contained distinct portions of fat and muscle, as see in Figure 6.1. Combined US and PA imaging was performed using a 21 MHz, 28.0 mm wide, array transducer coupled to a Vevo 2100 Imaging System (VisualSonics Inc., Toronto, CANADA). An Nd:YAG pump laser (Pro-Series, SpectraPhysics, Irvine, CA) coupled with an tunable OPO laser system (GWU PremiScan, GERMANY) operating at 1064 nm was used to optically illuminate the tissue phantom through an optical fiber bundle located adjacent to the ultrasound transducer. Laser fluence was recorded before and after the imaging trials. The needle inserted in the tissue sample was oriented transversely relative to the transducer. The transducer was then translated longitudinally along the length of the needle, acquiring 114 co-registered slices of both US and PA images. PA images normalized to the laser fluence were analyzed and co-registered to tissue position within the volume. A 3D volume model of the imaged sample was reconstructed using Amira software (Visage Imaging, San Diego, CA).

For quantitative analysis, PA signal energies were calculated using a small kernel surrounding the maximum signal from the cross-sectional PA image of the needle. The location of the kernel was verified by examining the location of the needle from the B-mode image which confirmed the presence of the needle. Data points in the kernel were averaged and normalized according to the mean laser fluence obtained during the trial. These values were obtained at each image cross-section which correlated to a specific cross-section within the tissue volume. These PA amplitude values were then plotted

Figure 6.1: Photograph of fresh healthy porcine sample with metal needle inserted superficially. Metal is inserted only 1 mm below the surface in distinct adipose tissue (left side) and muscle (right side) regions.

against the longitudinal position of the needle in order to determine the change in PA signal.

6.1.2 Preliminary Results

The three-dimensional scan was used to extract 114 cross-sectional two-dimensional US and PA images, which were necessary for further data processing. The image dimensions were 23.0 x 30.0 mm, in depth and lateral respectively. The US and PA images confirmed that the metal was located less than 1.0 mm from the surface, thereby diminishing any light attenuation effects from the tissue during the imaging (Fig. 6.2). The offline processed cross-sectional images were combined to produce a three-dimensional US and PA reconstruction of the tissue and needle (Fig. 6.3). In the PA image, a strong PA signal can be seen coming from the location of the metal. This high signal is confirmed in the B-mode image where a strong acoustic reflector is seen in the same position as in the PA image. The signal from each needle image slice was recorded and plotted against longitudinal position of the needle in the tissue (Fig. 6.4). The analysis of the PA images showed an increase in the PA signal amplitude of the needle when located in fat-based tissue versus water-based muscle tissue.

6.1.3 Additional Experimental Results

The results from Section 6.1.2 demonstrated that the PA signal of the needle is dependent on the surrounding tissue composition. Other parameters, which can affect PA signal amplitude, were evaluated. For example, since the metal needle was inserted proximal to the surface, the small distance could have provided enough optical extinction

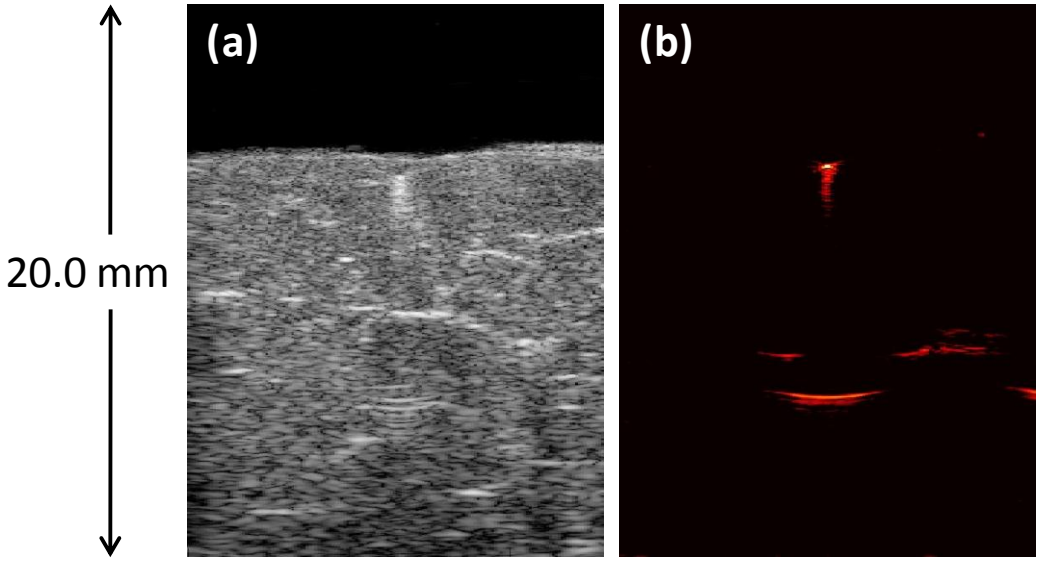

Figure 6.2: (a) US and (b) PA images of stainless steel metal piece inserted superficially below porcine tissue sample. Metal wire is visible in US and PA. Tissue composition is not easily differentiable in either US or PA image.

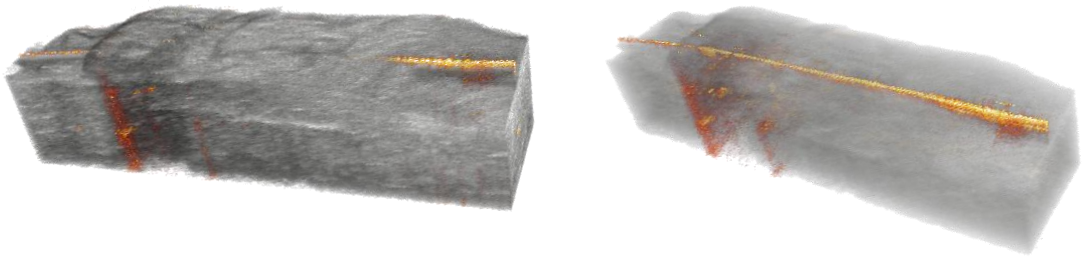

Figure 6.3: A three-dimensional reconstruction of the metal wire inserted into the porcine tissue sample. The reconstruction includes the co-registered combination of all 114 US and PA cross-sectional images as seen in Fig 6.2. The location of the metal needle as depicted by the PA signal, is red/yellow color coded. The porcine tissue is well visualized in the US signal, displayed in greyscale. The right image is a rotated perspective of the left image, displayed with the greyscale signal (US) slightly transparent to better visualize the presence of the wire inserted superficially through the tissue.

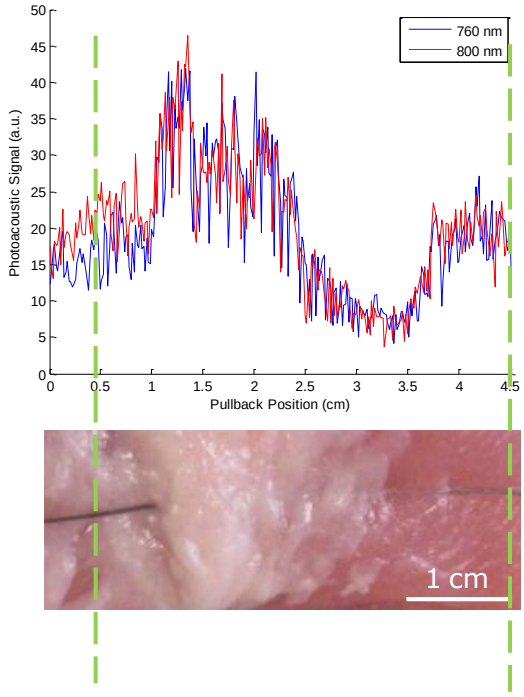

Figure 6.4: PA signal amplitude of wire in tissue is observed to fluctuate based on longitudinal position. Signal change is consistent with tissue composition of porcine sample (Fig 6.1, also shown here). Signal change correlates with % change between Grüneisen coefficient difference in porcine fat and muscle.

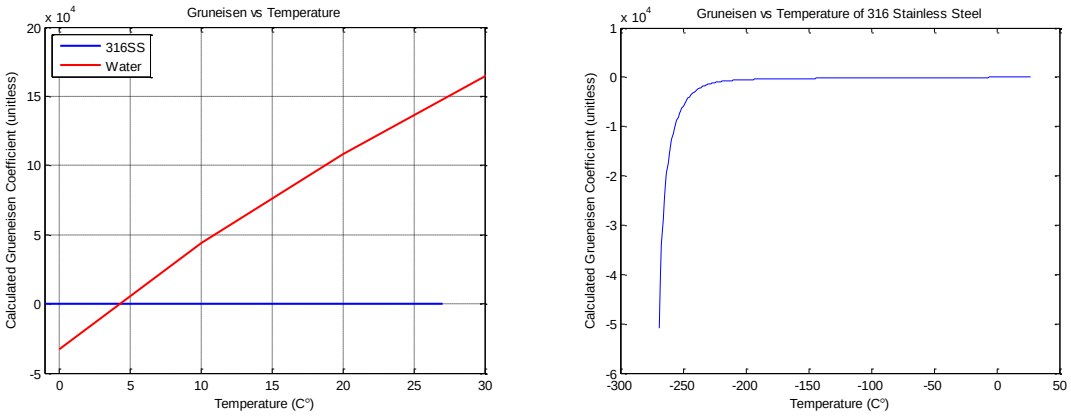

Figure 6.5: (Left) Grüneisen coefficient of water and 316L stainless steel vs. temperature. Gruneisen coefficient of water reaches zero at 4°C. (Right) Zoomed in graph of Grüneisen coefficient of 316L stainless steel.

to skew the results. That is, the portion of the metal located in the muscle region of the tissue could have come into contact with less local fluence due to much higher optical extinction than in fat. Furthermore, the fat tissue region may have provided more optical scattering to diffuse the light around the metal, providing a higher local fluence and more uniform laser irradiation to the metal. To better examine the effect of the environmental effects on PA intensity, a second experiment was conducted to more accurately quantify the contribution of various surrounding tissue types. Specifically, an experiment was required to determine which Grüneisen coefficient was actually influencing the PA results. First, an 18G needle was visualized with photoacoustic imaging at a laser wavelength of 800 nm in a water environment. The temperature of the water was gradually lowered from room temperature to 4°C. The hypothesis was that if the PA signal was dependent on the Grüneisen coefficient of the water, then the PA amplitude of the needle would approach zero at 4°C, where the Grüneisen coefficient is also zero (Fig. 6.5, left plot). On the contrary, if the PA signal was dependent on the Grüneisen coefficient of the metal, then the PA amplitude of the needle would remain somewhat constant as the temperature is varied (Fig. 6.5, right plot).

When the water temperature was reduced to 4°C, photoacoustic signal was still present from the metal, indicating that the environment of the water was not the only contributing factor to the photoacoustic signal from the metal (Fig. 6.6). However, the photoacoustic signal across the temperature range was not constant, indicating that a combination of Grüneisen coefficients from water and metal were contributing to the resultant photoacoustic signal, such as Eq. 6.1.

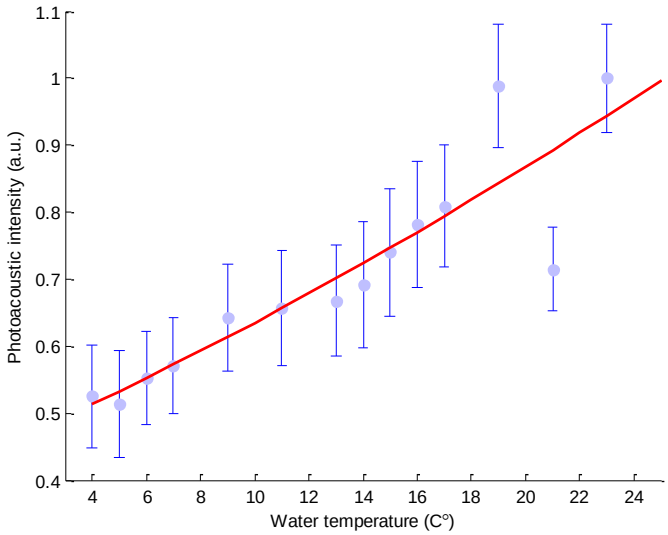

Figure 6.6: Photoacoustic signal amplitude vs. temperature of an 18G needle in water. At 4°C the signal amplitude is not zero indicating that the photoacoustic signal of the bulk metal is not absolutely dictated by the water environment.

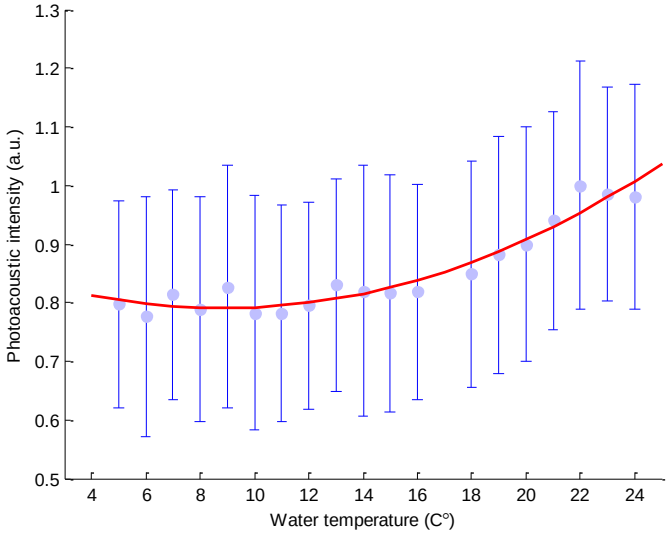

Figure 6.7: Photoacoustic signal amplitude vs. temperature of an 18G needle in mineral oil. The shape of the curve is dissimilar from Fig. 6.6 suggesting that the signal from the metal is still somewhat affected by environment.

$$P_0 = \mu_a \cdot \Phi \cdot (\alpha\Gamma_{water} + \beta\Gamma_{metal}) \qquad \textit{(Eq. 6.1)}$$

In Eq. 6.1, μ_a refers to the absorption coefficient of the metal, where Γ_{water} and Γ_{metal} represent the Grüneisen coefficients of water and metal, respectively. Each of the Grüneisen coefficients has a leading constant coefficient, α and β, indicating the relative contribution of the respective Grüneisen coefficient to the overall signal. To determine if the linear combination hypothesis was true, the previous experiment was repeated this time replacing the water environment with a mineral oil environment. The measured photoacoustic amplitude displayed a different variation with temperature (Fig. 6.7).

Using the data from Fig. 6.6, as well as the known Grüneisen coefficient of water, a linear set of equations could be solved which could determine the values of α and β in Eq. 6.1 for water and metal. The result was a value of α = 0.0001% and β = 99.999%. Despite the fact that β is several orders of magnitude higher than α, Fig. 6.5 shows that the Grüneisen coefficient of water is significantly higher than that of metal at higher temperatures. Therefore, these results suggest that for bulk metals, the photoacoustic signal produced from irradiating the metal surface is affected by both the metal properties itself and the properties of the surrounding environment.

Further work should be performed to determine the relationship between tissue environment and photoacoustic amplitude for a given metal. This type of lookup table could be valuable information applied to determining the accuracy of targeting metal implants or determining the effectiveness of therapy by monitoring the metal implants over time.

6.2 In-vivo Photoacoustic Imaging of Coronary Stents

6.2.1. Introduction

Recently, the first in-vivo intravascular photoacoustic imaging experiments were performed. The goal of the study was to determine the feasibility of using a combined ultrasound and photoacoustic catheter [1, 2] in an in-vivo rabbit environment. In-vivo environments differ from ex-vivo and phantom studies in several ways, including the addition of cardiac and respiratory motion, effects of blood circulation, and attenuation of signal from whole blood.

6.2.2 Materials and Methods

To test the feasibility of photoacoustic imaging in an in-vivo environment, a commercial off-the-shelf Liberté™ coronary stent (Boston Scientific Inc., Natick, MA) was deployed in an anesthetized New Zealand rabbit. The stent catheter was inserted through an 8F introducer that was placed through an incision made in the rabbit's thoracic aorta. The stent catheter was advanced to the 8^{th} rib space through X-ray guidance and the balloon stent was inflated to the rated burst pressure of 18.0 atm. According to the manufacturer, this pressure resulted in a stent inner diameter of 4.54 mm. Despite this size, the stent immediately migrated distally from the heart and lodged itself just below the rabbit's diaphragm. Confirmation of stent migration to below the diaphragm was made using standard IVUS pullback (Galaxy-2, Boston Scientific Inc., Natick, MA) and X-ray as read by the operating interventional cardiologist and the animal research associate on staff. The stent inflation balloon was removed from the

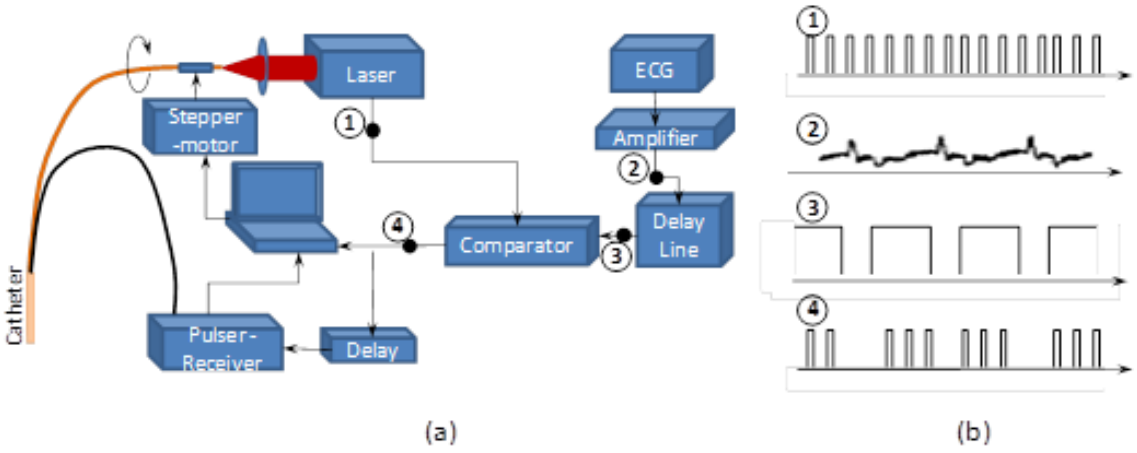

Figure 6.8: (a) Experimental setup and (b) electrical diagrams of the synchronization signals (1) 20 Hz laser P/R Signal. (2) Amplified ECG signal. (3) ECG gating. (4) P/R signal gating for data acquisition.

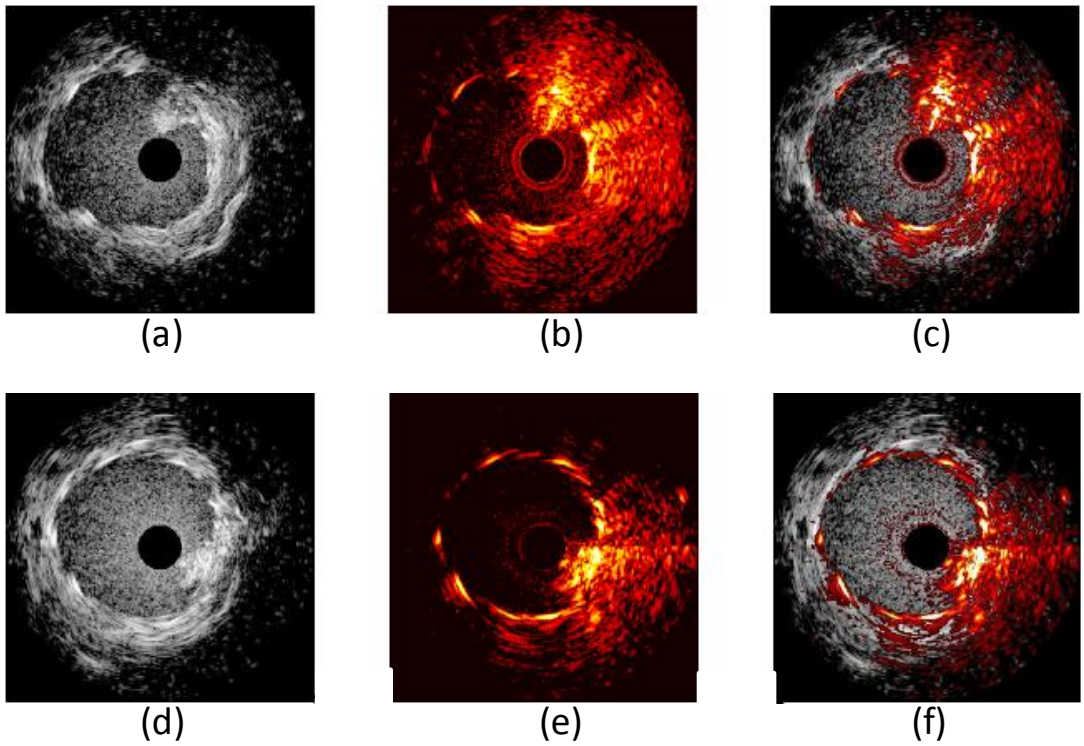

Figure 6.9: Ultrasound (left), photoacoustic (middle) and combined (right) images of rabbit's artery with freshly deployed stent. Upper and lower rows represent different cross-section of the artery.

introducer and replaced with the combined IVUS/IVPA catheter which rotated within the introducer through a custom bearing.

In brief, the experimental photoacoustic system comprised of a Q-switched Nd:YAG laser (Polaris II, New Wave Research, Inc., Portland, OR) laser operating at 1064 nm (Fig 6.8). The laser was coupled with an optical fiber to direct light to the catheter output. The distal portion of the imaging catheter consisted of an IVUS imaging transducer (Atlantis™ SR PLUS, Boston Scientific Inc., Natick, MA) and the optical fiber designed to direct light at 60° from the fiber output. Motion artifacts due to heart motion were diminished by using ECG triggering to control image acquisition. The amplified ECG signal was directed through a delay line to a custom-made comparator to avoid registration errors of experimental data due to heartbeat motion. US and PA data acquisition of a single A-line were obtained simultaneously, after which the catheter was rotated around the longitudinal axis to obtain 256 A-lines covering the full 360° cross section. Following the imaging experiment, the rabbit was sacrificed according to the approved animal care protocol.

6.2.3 Preliminary Results

The ultrasound, photoacoustic and combined images of two different cross-sections of the rabbit's artery with the stent are shown in Fig. 6.9. Ultrasound images shown in Fig. 6.9(a) and (d) are displayed in 35dB dynamic scale. The images indicate the location of blood and lumen as expected. However, the ultrasound contrast between soft tissue and metal struts is modest which makes it difficult to detect any stent shift or malapposition.

Photoacoustic images of the same cross-sections of the artery shown in Fig. 6.9(b) and (e) are displayed with 35 dB and 30 dB dynamic range, respectively. Decrease of the dynamic range results in a decrease of noise but can also mask the signal from the stent struts. For example, noise in Fig. 6.9(e) is lower than in Fig. 6.9(b) but the strut located at the 10 o'clock position was difficult to visualize in 6.9(e) compared with the image in Fig. 6.9(b). Overall, lower optical absorption in endogenous tissue constituents makes the image contrast between the stent and soft tissues significantly higher compared to ultrasound. In fact, soft tissue contrast is not visible in Fig. 6.9(b) and (e).

The combination of the ultrasound and photoacoustic images is shown in Fig. 6.9(c) and (f). Ultrasound images in grey scale depict the structure of the artery – lumen, arterial walls and blood are all visible. The photoacoustic signal (yellow-red tones) superimposed on the ultrasound images (grayscale) demonstrate the location of the stent with respect to the artery.

6.2.4 Conclusion

In conclusion, the first combined IVUS/IVPA imaging of a stents was successfully performed in an in-vivo animal model. The integrated IVUS/IVPA imaging catheter was demonstrated capable of intravascular imaging of both an artery with a stent in traditional ultrasound pulse-echo mode, as well as delivering laser pulses inside of the lumen to initiate photoacoustic response from stent struts. IVPA images of stent were obtained with high contrast.

In the future, the combined IVUS/IVPA imaging will be performed to differentiate lipids in atherosclerotic plaques. Such imaging will require the laser

irradiation to be performed at 1720 nm or 1210 nm wavelengths which can be provided by optical parametrical oscillators. In addition, the pulse energy should be increased to generate photoacoustic signals from lipids which have lower optical absorption coefficients, compared with metals. Further evaluation will include the development of a real-time combined IVUA/IVPA imaging system, smaller and more efficient integrated IVUS/IVPA imaging catheters and faster data processing algorithms. By performing in-vivo imaging of coronary stents, clinicians can assure proper placement of stents targeted to areas of high risk vulnerable plaques. Furthermore, imaging can also verify proper expansion of these stents, which can mitigate the risk of stent thrombosis and restenosis [3]. As the introduction of IVUS decreased the incidence of stent thrombosis from 2% to 0.7%, the introduction of IVPA may further decrease these numbers even further due to improved plaque and stent visualization.

6.3 REFERENCES

1. Karpiouk, A.B., B. Wang, and S.Y. Emelianov, *Development of a catheter for combined intravascular ultrasound and photoacoustic imaging.* The Review of scientific instruments, 2010. **81**(1): p. 014901.

2. Jansen, K., A.F. van der Steen, H.M. van Beusekom, J.W. Oosterhuis, and G. van Soest, *Intravascular photoacoustic imaging of human coronary atherosclerosis.* Optics letters, 2011. **36**(5): p. 597-9.

3. Maehara, A., G.S. Mintz, and N.J. Weissman, *Advances in intravascular imaging.* Circulation. Cardiovascular interventions, 2009. **2**(5): p. 482-90.

Chapter 7: Final Conclusions

7.1 MOTIVATION

Accurate insertion and monitoring of metal implants in-vivo is essential for clinical diagnosis and therapy of various diseases. Clinical studies and examples have demonstrated that the misplacement errors of these metal devices can have dramatic consequences. In this thesis, the research focused on three main metal devices that are in widespread use today: needles [1], coronary stents [2] and brachytherapy seeds [3]. Each application requires proper image-guidance for correct usage. For needles, image guidance is required to ensure correct local injection delivery or needle aspiration biopsy. Fine needle aspiration biopsies are performed in order to avoid major surgical excisions when obtaining tissue biopsy procedures. However, because of the small biopsy sample, the risk is that the sample is collected outside of the tumorigenic region, resulting in a false negative result. Implantation of stents requires that confirmation that proper stent apposition has been achieved due to balloon inflation. Furthermore, it is important to guide the stent to shield the vulnerable region of an atherosclerotic plaque. With prostate brachytherapy seeds, the ability to monitor seed placement is crucial because needle deflections or tissue deformation can result in seed misplacement errors, which decreases the efficiency of the pre-established treatment plan. Real-time monitoring allows for an adaptive treatment plan that can properly dose the suspect tumor regions. For the described applications and other possible clinical practices involving the use of metallic implants, an imaging technology that can accurately depict the location of the metal

objects, relative to their respective backgrounds, in real-time, is necessary to improve the safety and the efficacy of these procedures.

7.2 SUMMARY

This ensuing project successfully completed research on assembling a framework by which temporary and permanent metal implants could be more easily detected in-vivo. These metal implants are designed for the purpose of therapy treatment in the body, and require the precise and accurate placement in specific regions of interest. For clinical needles, image-guidance is required to direct the needle tip to a tissue region of interest for injections or for biopsy collection. Incorrect needle insertions can result in the misappropriation of therapy injections, or a possible false negative result for biopsy testing. Brachytherapy seeds require accurate guidance as the injection needle loaded with seeds must be imaged properly to ensure that the seeds are correctly placement within the prostate tumor(s). As previously stated in CHAPTER 4, needle deflections of only 5° from the insertion angle can decrease the minimum target dose by 10%, thus increasing the tumor-cell survival rate by a factor of 200 [4]. Seed placement that deviates from the dosimetric treatment plan can result in underdosed cancerous regions, requiring postoperative dose corrections through external-beam radiation therapy. For coronary stents, correct image guidance is necessary to guarantee that the stent is deployed in regions of plaque vulnerability and/or narrow stenosis.

Ultrasound is primarily used as the current standard of care for detecting needles stents and brachytherapy seeds. The use of ultrasound is beneficial because of its real-time capabilities, non-ionizing radiation, and soft tissue contrast. However, due to high

acoustic scattering from tissue, the contrast of metal implants can be low. Photoacoustic imaging can be used as an alternative, or complementary, imaging method to ultrasound for imaging metal. The optical absorption coefficient of metals is very high due to the electron cloud configuration within the metal which allows for individual electron absorption of a photon. Investigation of the imaging parameters for imaging specific metal implants reveals additional application considerations for photoacoustic imaging.

In summary, the current standard procedures for image guidance for needle insertions involves the use of handheld ultrasound array transducers with center frequencies around 5-12 MHz. Due to specular acoustic reflections from the surface of the needle, angled needle insertions of 15° or more resulted in a significant decrease of the ultrasound contrast relative to the acoustic speckle from the background tissue. This can then require the use of additional tools in order to ensure accurate positioning of the advancing needle tip. Photoacoustic imaging of metal needles allowed for penetration depths of a few centimeters. The actual penetration depth is dependent on the optical properties of the tissue background as well as the fluence provided to the region of interest. However, since the photoacoustic signal is generated in an omni-directional fashion from the surface of the needle, the detectability of the needle is far greater in photoacoustic compared to ultrasound imaging.

For detection of brachytherapy seeds, the need for a real-time imaging modality is necessary due to needle deflection and tissue deformation that can occur during the implantation procedure. Both needle deflection and tissue deformation can cause seeds to be implanted incorrectly away from the regions of interest determined by the pre-

established treatment plan. A real-time imaging modality could indicate to the physician that placement errors had occurred and allow for an adaptive treatment plan, correcting the dose so that tumor regions received the correct radiation exposure [5]. Current methods utilize CT or X-ray as an intermediate step during or after the procedure to evaluate seed location and then correct the implantation following imaging [6]. Photoacoustic imaging was shown to serve as an excellent candidate for visualizing seed positioning. Though seed orientation was not easily determined from the photoacoustic signal, the detectability of the seed's presence was far superior to ultrasound, resulting in a contrast improvement greater than 30 dB in the seed's signal to the prostate tissue background. The literature showed that due to the magnitude of seeds implanted at any given time, knowing the orientation of each individual seed is not important compared to the implantation distribution of the body of all the seeds as a whole [7]. The ability to visualize the presence of the seeds with high resolution in the context of the prostate tissue background can greatly benefit adaptive implantation procedures.

Coronary arterial stents have been demonstrated to be well-visualized using intravascular photoacoustic imaging. This new imaging method could improve current technologies, which are unable to accurately image the position of the stent struts relative to the lumen wall. Detection of stent struts is important in determining stent patency and malapposition. Imaging modalities such as x-ray and MRI can visualize the presence of the stent in the longitudinal direction of the vessel, but can suffer from artifacts that can hinder the accuracy of determining the cross-sectional orientation of the stent as it relates to the lumen wall. Photoacoustic imaging was demonstrated to give excellent contrast,

resolution and penetration depth for identifying the presence of the individual stent struts. Due to an increase in imaging contrast, clinicians should be able to better identify stents during both deployment and monitoring procedures. Studies have shown that the use of IVUS during stent implantation optimized the procedure, which led to a reduction in stent thrombosis both within the first month window, and from 1 to 12 months (from 2.0% stent thrombosis, down to 0.7%) [8]. However, other studies demonstrated that stent thrombosis was more likely to happen in areas with a small minimum stent area, and residual plaque formation at the edge of the stent [9]. Small minimum stent area could be caused either by stent underexpansion or a small blood vessel. The limitations of IVUS not being able to fully visualize stents and/or identify areas of plaque formation may play a role in explaining why stent thrombosis still remains a small but serious problem. IVPA may be able to reduce the incidence of stent thrombosis even further due to its high ability to identify stents with sufficient contrast [10], and visualize areas of vulnerable plaque [11]. The actual benefit of using combined IVPA and IVUS as opposed to IVUS alone can only be inferred at this point apart from a clinical trial. However, each intravascular imaging technology has its own unique advantages and disadvantages, that the use of multiple techniques would be more beneficial than the use of a single technique. Though the use of multiple techniques would not be practical for daily procedures, current trends have shown the shift towards combining multiple modalities into a single catheter device [8, 12-16].

7.3 LIMITATIONS

Each of the experiments in this study utilized imaging phantoms or ex-vivo tissue samples. Excised tissue samples are more realistic than gelatin or PVA phantoms for testing imaging technology; however, neither ex-vivo tissue nor PVA phantoms can match the true environment surroundings seen in-vivo. Many of the limitations in this study arise from the use of non in-vivo imaging samples. For example, previous research has shown that the optical properties of tissue can change due to excision and storage [17]. Delpy et. al. found an increase in light transmission through tissue after death [18]. Furthermore, temperature can have an effect on optical scattering through tissue [19]. Studies have indicated that proteins in tissue can cause a positive temperature coefficient for scattering; that is, increases in temperature can cause the scattering coefficient to increase. Lipids in tissue can cause an inverse relationship between temperature and scattering. For photoacoustic imaging, these changes in light transmission in ex-vivo studies can improve or worsen penetration depth for tissue samples.

The characterization of tissue optical properties becomes ever more important when performing spectroscopic imaging. Since the optical properties of tissue are largely unknown prior to imaging, laser fluence compensation for quantitative measurements can be very difficult or error-prone, at best [20, 21]. Monte-Carlo techniques have been used to estimate depth dependent laser fluence using average values [22, 23]. Though models for estimating photon propagation using Monte-Carlo are good at estimating small depths, the non-uniform depths used in ultrasound and photoacoustic imaging can introduce large errors during the inversion process [24].

The presence of blood in-vivo can also introduce light attenuation not present in ex-vivo studies. Both oxygenated and deoxygenated hemoglobin have strong optical absorption and can affect laser fluence, as well as contrast-to-noise when imaging inclusions with optical absorptions similar to blood. The presence of blood was partly examined in CHAPTER 5, which described deployment of stents in coronary arteries. Though stents were imaged using a highly scattering environment in place of water, the total extinction coefficient of the environment was not as high as blood. Furthermore, in an in-vivo environment, blood flow would also add another parameter of cardiac motion and acoustic speckle into the imaging equation. Acoustic speckle would occur when using higher frequency intravascular transducers such as 40 MHz, but not at 20 MHz.

The experiment involving imaging of brachytherapy seeds was limited by the orientation of the laser incident irradiation and the ultrasound transducer. An assumption was made that the surface area of the seed facing the ultrasound transducer was irradiated evenly. This did not occur since the irradiation source was placed off-axis, which is not optimal nor realistic for irradiation alignment with the obliquely positioned transducer face. Future imaging probes will either integrate both US and PA together, or use oppositely facing light irradiation and acoustic detection. Furthermore, the laser beam profile was not homogeneous across the seed surface causing irregularities in the produced photoacoustic signal. Imaging in-vivo tissue will improve light irradiation as prostate tissue will lessen these non-homogenous effects by diffusing the light around the seed. In a more realistic clinical setting, the laser delivery system would be aligned with the US transducer or at opposing directions, providing more direct irradiation of the seeds

being imaged. Future work would involve irradiating the prostate by inserting an optical fiber through the urethra and receiving through a TRUS transducer, thereby reducing the required light propagation depth from several centimeters to only 2-3 cm. Future studies will address the optimal geometry of light irradiation and acoustic detection, allowing for implementation of photoacoustic imaging to be used in clinical practice, introducing a new innovative approach to brachytherapy implantation and follow-up procedures.

7.4 CONCLUSIONS

A framework for using combined ultrasound and photoacoustic imaging to guide, detect and characterize metal implants was successfully investigated. In this study, phantom, ex-vivo and in vivo experiments were conducted to demonstrate the efficacy of photoacoustic imaging to detect metal. Planning was first conducted by examining the absorption properties of metal. Experiments were conducted using three different metal implants that required separately designed imaging setups for proper visualization. Photoacoustic imaging was conducted on metal injection needles using a handheld array transducer, and a signal filtering algorithm was utilized to enhance the location accuracy of the needles. Secondly, brachytherapy seeds were imaged in bovine prostate tissue. It was proposed that in-vivo photoacoustic imaging of seeds would be performed using an optical fiber introduced trans-urethrally, with acoustic detection performed using a standard trans-rectal ultrasound probe. Finally, photoacoustic imaging of coronary stents was performed using a combined intravascular ultrasound and photoacoustic catheter. Light delivered intravascularly was subject to extinction by blood and fibrous growth due to restenosis and additional lesion growth. Quantitative analysis showed that

photoacoustic imaging of metal in tissue background resulted in a greater than 30 dB increase in contrast compared to the use of ultrasound.

Further studies are necessary in-vivo to establish the laser fluence requirements necessary for photoacoustic imaging, as well as to determine the ability to characterize tissue composition based on changes in the Grüneisen coefficient. Overall, this research has built the foundation for a new perspective on clinical applications of combined ultrasound and photoacoustic imaging has the potential to help guide, detect and follow-up on clinical metal implants introduced in-vivo.

7.5 REFERENCES

1. Chapman, G.A., D. Johnson, and A.R. Bodenham, *Visualisation of needle position using ultrasonography.* Anaesthesia, 2006. **61**(2): p. 148-58.

2. Butany, J., K. Carmichael, S.W. Leong, and M.J. Collins, *Coronary artery stents: identification and evaluation.* J Clin Pathol, 2005. **58**(8): p. 795-804.

3. Davis, B.J., R.R. Kinnick, M. Fatemi, E.P. Lief, R.A. Robb, and J.F. Greenleaf, *Measurement of the ultrasound backscatter signal from three seed types as a function of incidence angle: application to permanent prostate brachytherapy.* International journal of radiation oncology, biology, physics, 2003. **57**(4): p. 1174-82.

4. Nath, S., Z. Chen, N. Yue, S. Trumpore, and R. Peschel, *Dosimetric effects of needle divergence in prostate seed implant using 125I and 103Pd radioactive seeds.* Medical physics, 2000. **27**(5): p. 1058-66.

5. Lee, E.K. and M. Zaider, *Intraoperative dynamic dose optimization in permanent prostate implants.* International journal of radiation oncology, biology, physics, 2003. **56**(3): p. 854-61.

6. Westendorp, H., C.J. Hoekstra, A. van't Riet, A.W. Minken, and J.J. Immerzeel, *Intraoperative adaptive brachytherapy of iodine-125 prostate implants guided by C-arm cone-beam computed tomography-based dosimetry.* Brachytherapy, 2007. **6**(4): p. 231-7.

7. Corbett, J.F., J.J. Jezioranski, J. Crook, T. Tran, and I.W. Yeung, *The effect of seed orientation deviations on the quality of 125I prostate implants.* Physics in medicine and biology, 2001. **46**(11): p. 2785-800.

8. Maehara, A., G.S. Mintz, and N.J. Weissman, *Advances in intravascular imaging.* Circulation. Cardiovascular interventions, 2009. **2**(5): p. 482-90.

9. Okabe, T., G.S. Mintz, A.N. Buch, P. Roy, Y.J. Hong, K.A. Smith, R. Torguson, N. Gevorkian, Z. Xue, L.F. Satler, K.M. Kent, A.D. Pichard, N.J. Weissman, and R. Waksman, *Intravascular ultrasound parameters associated with stent thrombosis after drug-eluting stent deployment.* The American journal of cardiology, 2007. **100**(4): p. 615-20.

10. Su, J.L., B. Wang, and S.Y. Emelianov, *Photoacoustic imaging of coronary artery stents.* Opt Express, 2009. **17**(22): p. 19894-901.

11. Wang, B., J.L. Su, J. Amirian, S.H. Litovsky, R. Smalling, and S. Emelianov, *Detection of lipid in atherosclerotic vessels using ultrasound-guided spectroscopic intravascular photoacoustic imaging.* Optics express, 2010. **18**(5): p. 4889-97.

12. Vancraeynest, D., A. Pasquet, V. Roelants, B.L. Gerber, and J.L. Vanoverschelde, *Imaging the vulnerable plaque.* Journal of the American College of Cardiology, 2011. **57**(20): p. 1961-79.

13. Li, X., J. Yin, C. Hu, Q. Zhou, K.K. Shung, and Z. Chen, *High-resolution coregistered intravascular imaging with integrated ultrasound and optical coherence tomography probe.* Applied Physics Letters, 2010. **97**(13): p. 133702.

14. Goderie, T.P., G. van Soest, H.M. Garcia-Garcia, N. Gonzalo, S. Koljenovic, G.J. van Leenders, F. Mastik, E. Regar, J.W. Oosterhuis, P.W. Serruys, and A.F. van der Steen, *Combined optical coherence tomography and intravascular ultrasound radio frequency data analysis for plaque characterization. Classification accuracy of human coronary plaques in vitro.* The international journal of cardiovascular imaging, 2010. **26**(8): p. 843-50.

15. Karpiouk, A.B., B. Wang, and S.Y. Emelianov, *Development of a catheter for combined intravascular ultrasound and photoacoustic imaging.* The Review of scientific instruments, 2010. **81**(1): p. 014901.

16. Schultz, C.J., P.W. Serruys, M. van der Ent, J. Ligthart, F. Mastik, S. Garg, J.E. Muller, M.A. Wilder, A.F. van de Steen, and E. Regar, *First-in-man clinical use of combined near-infrared spectroscopy and intravascular ultrasound: a potential key to predict distal embolization and no-reflow?* Journal of the American College of Cardiology, 2010. **56**(4): p. 314.

17. Simpson, C.R., M. Kohl, M. Essenpreis, and M. Cope, *Near-infrared optical properties of ex vivo human skin and subcutaneous tissues measured using the Monte Carlo inversion technique.* Phys Med Biol, 1998. **43**(9): p. 2465-78.

18. Delpy, D.T., M. Cope, P. van der Zee, S. Arridge, S. Wray, and J. Wyatt, *Estimation of optical pathlength through tissue from direct time of flight measurement.* Phys Med Biol, 1988. **33**(12): p. 1433-42.

19. Laufer, J., R. Simpson, M. Kohl, M. Essenpreis, and M. Cope, *Effect of temperature on the optical properties of ex vivo human dermis and subdermis.* Phys Med Biol, 1998. **43**(9): p. 2479-89.

20. Laufer, J., D. Delpy, C. Elwell, and P. Beard, *Quantitative spatially resolved measurement of tissue chromophore concentrations using photoacoustic spectroscopy: application to the measurement of blood oxygenation and haemoglobin concentration.* Physics in medicine and biology, 2007. **52**(1): p. 141-68.

21. Maslov, K., H.F. Zhang, and L.H. Wang, *Effects of wavelength-dependent fluence attenuation on the noninvasive photoacoustic imaging of hemoglobin oxygen saturation in subcutaneous vasculature in vivo.* Inverse Problems, 2007. **23**(6): p. S113-S122.

22. Hourdakis, C.J. and A. Perris, *A Monte Carlo estimation of tissue optical properties for use in laser dosimetry.* Phys Med Biol, 1995. **40**(3): p. 351-64.

23. Wang, L. and S.L. Jacques, *Hybrid model of Monte Carlo simulation and diffusion theory for light reflectance by turbid media.* Journal of the Optical Society of America. A, Optics, image science, and vision, 1993. **10**(8): p. 1746-52.

24. Cox, B.T., S.R. Arridge, and P.C. Beard, *Estimating chromophore distributions from multiwavelength photoacoustic images.* Journal of the Optical Society of America. A, Optics, image science, and vision, 2009. **26**(2): p. 443-55.

Bibliography

American National Standards Institute *ANSI Z136.1-2007 American national standards for safe use of lasers*. 2007.

Abolhassani, N., R.V. Patel, and F. Ayazi, *Minimization of needle deflection in robot-assisted percutaneous therapy.* Int J Med Robot, 2007. **3**(2): p. 140-8.

Andreev, V.G., A.A. Karabutov, and A.A. Oraevsky, *Detection of ultrawide-band ultrasound pulses in optoacoustic tomography.* IEEE Trans Ultrason Ferroelectr Freq Control, 2003. **50**(10): p. 1383-90.

Barash, P. and S. Akhtar, *Coronary stents: factors contributing to perioperative major adverse cardiovascular events.* British journal of anaesthesia, 2010. **105 Suppl 1**: p. i3-15.

Barlis, P., K. Dimopoulos, J. Tanigawa, E. Dzielicka, G. Ferrante, F. Del Furia, and C. Di Mario, *Quantitative analysis of intracoronary optical coherence tomography measurements of stent strut apposition and tissue coverage.* Int J Cardiol, 2009.

Bell, A.G., *On the production and reproduction of sound by light.* American Journal of Science, 1880. **20**(305-324).

Butany, J., K. Carmichael, S.W. Leong, and M.J. Collins, *Coronary artery stents: identification and evaluation.* J Clin Pathol, 2005. **58**(8): p. 795-804.

Calasso, I.G., W. Craig, and G.J. Diebold, *Photoacoustic Point Source.* Physical Review Letters, 2001. **86**(16): p. 3550-3553.

Chapman, G.A., D. Johnson, and A.R. Bodenham, *Visualisation of needle position using ultrasonography.* Anaesthesia, 2006. **61**(2): p. 148-58.

Charboneau, J.W., C.C. Reading, and T.J. Welch, *CT and sonographically guided needle biopsy: current techniques and new innovations.* AJR Am J Roentgenol, 1990. **154**(1): p. 1-10.

Chen, Y.S., W. Frey, S. Kim, K. Homan, P. Kruizinga, K. Sokolov, and S. Emelianov, *Enhanced thermal stability of silica-coated gold nanorods for photoacoustic imaging and image-guided therapy.* Optics express, 2010. **18**(9): p. 8867-78.

Chen, Y.S., W. Frey, S. Kim, P. Kruizinga, K. Homan, and S. Emelianov, *Silica-coated gold nanorods as photoacoustic signal nanoamplifiers.* Nano Letters, 2011. **11**(2): p. 348-54.

Chin, K.J., A. Perlas, V.W. Chan, and R. Brull, *Needle visualization in ultrasound-guided regional anesthesia: challenges and solutions.* Reg Anesth Pain Med, 2008. **33**(6): p. 532-44.

Corbett, J.F., J.J. Jezioranski, J. Crook, T. Tran, and I.W. Yeung, *The effect of seed orientation deviations on the quality of 125I prostate implants.* Physics in medicine and biology, 2001. **46**(11): p. 2785-800.

Costa, M.A. and D.I. Simon, *Molecular basis of restenosis and drug-eluting stents.* Circulation, 2005. **111**(17): p. 2257-73.

Cox, B., J. Laufer, and P. Beard. *The challenges for quantitative photoacoustic imaging*. in *Proceedings of SPIE Vol. 7177*. 2009.

Cox, B.T., S.R. Arridge, and P.C. Beard, *Estimating chromophore distributions from multiwavelength photoacoustic images.* J Opt Soc Am A Opt Image Sci Vis, 2009. **26**(2): p. 443-55.

Cox, B.T., S.R. Arridge, and P.C. Beard, *Estimating chromophore distributions from multiwavelength photoacoustic images.* Journal of the Optical Society of America. A, Optics, image science, and vision, 2009. **26**(2): p. 443-55.

Davis, B.J., R.R. Kinnick, M. Fatemi, E.P. Lief, R.A. Robb, and J.F. Greenleaf, *Measurement of the ultrasound backscatter signal from three seed types as a function of incidence angle: application to permanent prostate brachytherapy.* International journal of radiation oncology, biology, physics, 2003. **57**(4): p. 1174-82.

Delpy, D.T., M. Cope, P. van der Zee, S. Arridge, S. Wray, and J. Wyatt, *Estimation of optical pathlength through tissue from direct time of flight measurement.* Phys Med Biol, 1988. **33**(12): p. 1433-42.

Diebold, G.J., A.C. Beveridge, and T.J. Hamilton, *The photoacoustic effect generated by an incompressible sphere.* The Journal of the Acoustical Society of America, 2002. **112**(5 Pt 1): p. 1780-6.

Elgort, D.R., C.M. Hillenbrand, S. Zhang, E.Y. Wong, S. Rafie, J.S. Lewin, and J.L. Duerk, *Image-guided and -monitored renal artery stenting using only MRI.* J Magn Reson Imaging, 2006. **23**(5): p. 619-27.

Faber, D.J., M.C. Aalders, E.G. Mik, B.A. Hooper, M.J. van Gemert, and T.G. van Leeuwen, *Oxygen saturation-dependent absorption and scattering of blood.* Phys

Rev Lett, 2004. **93**(2): p. 028102.

Faraggi, E., S. Wang, and B. Gerstman. *Stress confinement, shock wave formation, and laser-induced damage*. in *Optical Interactions with Tissue and Cells XVI* 2005. San Jose, CA, USA

Finet, G., C. Cachard, P. Delachartre, E. Maurincomme, and J. Beaune, *Artifacts in intravascular ultrasound imaging during coronary artery stent implantation.* Ultrasound Med Biol, 1998. **24**(6): p. 793-802.

Goderie, T.P., G. van Soest, H.M. Garcia-Garcia, N. Gonzalo, S. Koljenovic, G.J. van Leenders, F. Mastik, E. Regar, J.W. Oosterhuis, P.W. Serruys, and A.F. van der Steen, *Combined optical coherence tomography and intravascular ultrasound radio frequency data analysis for plaque characterization. Classification accuracy of human coronary plaques in vitro.* The international journal of cardiovascular imaging, 2010. **26**(8): p. 843-50.

Gonzalez, M.G., X. Liu, R. Niessner, and C. Haisch, *Strong size-dependent photoacoustic effect on gold nanoparticles by laser-induced nanobubbles.* Applied Physics Letters, 2010. **96**(17): p. 174104.

Gronningsaeter, A., T. Lie, K. Bolz, and A. Heimdal, *Ultrasonographic stent-imaging artifacts.* Journal of Vascular Investigation, 1995. **3**: p. 140-149.

Gusev, V.E. and A.A. Karabutov, *Laser Optoacoustics*1993, New York: American Institute of Physics. 336.

Han, B.H., K. Wallner, G. Merrick, W. Butler, S. Sutlief, and J. Sylvester, *Prostate brachytherapy seed identification on post-implant TRUS images.* Medical physics, 2003. **30**(5): p. 898-900.

Hatada, T., H. Ishii, S. Ichii, K. Okada, and T. Yamamura, *Ultrasound-guided fine-needle aspiration biopsy for breast tumors: needle guide versus freehand technique.* Tumori, 1999. **85**(1): p. 12-4.

Hebard, S. and G. Hocking, *Echogenic Technology Can Improve Needle Visibility During Ultrasound-Guided Regional Anesthesia.* Reg Anesth Pain Med, 2011. **36**(2): p. 185-189.

Hoelen, C.G., F.F. de Mul, R. Pongers, and A. Dekker, *Three-dimensional photoacoustic imaging of blood vessels in tissue.* Optics letters, 1998. **23**(8): p. 648-50.

Homan, K., S. Kim, Y.S. Chen, B. Wang, S. Mallidi, and S. Emelianov, *Prospects of*

molecular photoacoustic imaging at 1064 nm wavelength. Optics letters, 2010. **35**(15): p. 2663-5.

Homan, K., J. Shah, S. Gomez, H. Gensler, A.B. Karpiouk, L. Brannon-Peppas, and S.Y. Emelianov. *Combined Ultrasound and Photoacoustic Imaging of Pancreatic Cancer Using Nanocage Contrast Agents*. in *Proceedings of the 2009 SPIE Photonics West Symposium: Photons Plus Ultrasound: Imaging and Sensing*. 2009.

Hourdakis, C.J. and A. Perris, *A Monte Carlo estimation of tissue optical properties for use in laser dosimetry.* Phys Med Biol, 1995. **40**(3): p. 351-64.

Hricak, H., R.B. Jeffrey, G.C. Dooms, and E.A. Tanagho, *Evaluation of prostate size: a comparison of ultrasound and magnetic resonance imaging.* Urologic radiology, 1987. **9**(1): p. 1-8.

Hu, S. and L.V. Wang, *Photoacoustic imaging and characterization of the microvasculature.* Journal of Biomedical Optics, 2010. **15**(1): p. 011101-15.

Hug, J., E. Nagel, A. Bornstedt, B. Schnackenburg, H. Oswald, and E. Fleck, *Coronary arterial stents: safety and artifacts during MR imaging.* Radiology, 2000. **216**(3): p. 781-7.

Jandzinski, D.I., N. Carson, D. Davis, D.J. Rubens, S.L. Voci, and R.H. Gottlieb, *Treated needles: do they facilitate sonographically guided biopsies?* Journal of ultrasound in medicine : official journal of the American Institute of Ultrasound in Medicine, 2003. **22**(11): p. 1233-7.

Jang, I.K., B.E. Bouma, D.H. Kang, S.J. Park, S.W. Park, K.B. Seung, K.B. Choi, M. Shishkov, K. Schlendorf, E. Pomerantsev, S.L. Houser, H.T. Aretz, and G.J. Tearney, *Visualization of coronary atherosclerotic plaques in patients using optical coherence tomography: comparison with intravascular ultrasound.* J Am Coll Cardiol, 2002. **39**(4): p. 604-9.

Jansen, K., A.F. van der Steen, H.M. van Beusekom, J.W. Oosterhuis, and G. van Soest, *Intravascular photoacoustic imaging of human coronary atherosclerosis.* Optics letters, 2011. **36**(5): p. 597-9.

Jemal, A., R. Siegel, J. Xu, and E. Ward, *Cancer statistics, 2010.* CA: a cancer journal for clinicians, 2010. **60**(5): p. 277-300.

Karlsson, B. and C.G. Ribbing, *Optical constants and spectral selectivity of stainless steel and its oxides.* J. Appl. Phys., 1982. **53**(9): p. 6340-6346.

Karpiouk, A.B., B. Wang, and S.Y. Emelianov, *Development of a catheter for combined intravascular ultrasound and photoacoustic imaging.* The Review of scientific instruments, 2010. **81**(1): p. 014901.

Karpiouk, A.B., B. Wang, and S.Y. Emelianov, *Development of a catheter for combined intravascular ultrasound and photoacoustic imaging.* The Review of scientific instruments, 2010. **81**(1): p. 014901.

Kawase, Y., K. Hoshino, R. Yoneyama, J. McGregor, R.J. Hajjar, I.K. Jang, and M. Hayase, *In vivo volumetric analysis of coronary stent using optical coherence tomography with a novel balloon occlusion-flushing catheter: a comparison with intravascular ultrasound.* Ultrasound Med Biol, 2005. **31**(10): p. 1343-9.

Kolodgie, F.D., A.S. Katocs, Jr., E.E. Largis, S.M. Wrenn, J.F. Cornhill, E.E. Herderick, S.J. Lee, and R. Virmani, *Hypercholesterolemia in the rabbit induced by feeding graded amounts of low-level cholesterol. Methodological considerations regarding individual variability in response to dietary cholesterol and development of lesion type.* Arteriosclerosis, thrombosis, and vascular biology, 1996. **16**(12): p. 1454-64.

Kruger, R.A., *Photoacoustic ultrasound.* Medical physics, 1994. **21**(1): p. 127-31.

Kruger, R.A., P. Liu, Y.R. Fang, and C.R. Appledorn, *Photoacoustic ultrasound (PAUS)--reconstruction tomography.* Med Phys, 1995. **22**(10): p. 1605-9.

Ku, G. and L.V. Wang, *Deeply penetrating photoacoustic tomography in biological tissues enhanced with an optical contrast agent.* Opt Lett, 2005. **30**(5): p. 507-9.

Laufer, J., D. Delpy, C. Elwell, and P. Beard, *Quantitative spatially resolved measurement of tissue chromophore concentrations using photoacoustic spectroscopy: application to the measurement of blood oxygenation and haemoglobin concentration.* Physics in medicine and biology, 2007. **52**(1): p. 141-68.

Laufer, J., R. Simpson, M. Kohl, M. Essenpreis, and M. Cope, *Effect of temperature on the optical properties of ex vivo human dermis and subdermis.* Phys Med Biol, 1998. **43**(9): p. 2479-89.

Laufer, J.G., C.E. Elwell, D.T. Delpy, and C.C. Beard, *Spatially resolved blood oxygenation measurements using time-resolved photoacoustic spectroscopy.* Adv Exp Med Biol, 2006. **578**: p. 155-60.

Lee, E.K. and M. Zaider, *Intraoperative dynamic dose optimization in permanent prostate implants.* International journal of radiation oncology, biology, physics, 2003. **56**(3): p. 854-61.

Lee, E.K. and M. Zaider, *Intraoperative dynamic dose optimization in permanent prostate implants.* International journal of radiation oncology, biology, physics, 2003. **56**(3): p. 854-61.

Li, P.C., C.W. Wei, C.K. Liao, C.D. Chen, K.C. Pao, C.R. Wang, Y.N. Wu, and D.B. Shieh, *Photoacoustic imaging of multiple targets using gold nanorods.* IEEE Trans Ultrason Ferroelectr Freq Control, 2007. **54**(8): p. 1642-7.

Li, X., J. Yin, C. Hu, Q. Zhou, K.K. Shung, and Z. Chen, *High-resolution coregistered intravascular imaging with integrated ultrasound and optical coherence tomography probe.* Applied Physics Letters, 2010. **97**(13): p. 133702.

Maehara, A., G.S. Mintz, and N.J. Weissman, *Advances in intravascular imaging.* Circulation. Cardiovascular interventions, 2009. **2**(5): p. 482-90.

Maintz, D., R.M. Botnar, R. Fischbach, W. Heindel, W.J. Manning, and M. Stuber, *Coronary magnetic resonance angiography for assessment of the stent lumen: a phantom study.* J Cardiovasc Magn Reson, 2002. **4**(3): p. 359-67.

Maintz, D., K.U. Juergens, T. Wichter, M. Grude, W. Heindel, and R. Fischbach, *Imaging of coronary artery stents using multislice computed tomography: in vitro evaluation.* Eur Radiol, 2003. **13**(4): p. 830-5.

Mallidi, S. and S. Emelianov, *Photoacoustic technique to measure beam profile of pulsed laser systems.* Rev Sci Instrum, 2009. **80**(5): p. 054901.

Mallidi, S., T. Larson, J. Tam, P.P. Joshi, A. Karpiouk, K. Sokolov, and S. Emelianov, *Multiwavelength photoacoustic imaging and plasmon resonance coupling of gold nanoparticles for selective detection of cancer.* Nano Lett, 2009. **9**(8): p. 2825-31.

Maslov, K., H.F. Zhang, and L.H. Wang, *Effects of wavelength-dependent fluence attenuation on the noninvasive photoacoustic imaging of hemoglobin oxygen saturation in subcutaneous vasculature in vivo.* Inverse Problems, 2007. **23**(6): p. S113-S122.

McDonald, M.A., L. Jankovic, K. Shahzad, M. Burcher, and K.C. Li, *Acoustic fingerprints of dye-labeled protein submicrosphere photoacoustic contrast agents.* J Biomed Opt, 2009. **14**(3): p. 034032.

Merrick, G.S., W.M. Butler, A.T. Dorsey, J.H. Lief, and M.L. Benson, *Seed fixity in the prostate/periprostatic region following brachytherapy.* Int J Radiat Oncol Biol Phys, 2000. **46**(1): p. 215-20.

Mintz, G.S., S.E. Nissen, W.D. Anderson, S.R. Bailey, R. Erbel, P.J. Fitzgerald, F.J. Pinto, K. Rosenfield, R.J. Siegel, E.M. Tuzcu, and P.G. Yock, *American College of Cardiology Clinical Expert Consensus Document on Standards for Acquisition, Measurement and Reporting of Intravascular Ultrasound Studies (IVUS). A report of the American College of Cardiology Task Force on Clinical Expert Consensus Documents.* J Am Coll Cardiol, 2001. **37**(5): p. 1478-92.

Modgil, D., M.A. Anastasio, and P.J.L. Riviere, *Image reconstruction in photoacoustic tomography with variable speed of sound using a higher-order geometrical acoustics approximation.* Journal of Biomedical Optics, 2010. **15**(2): p. 021308.

Morooka, M., K. Kubota, Y. Kono, K. Ito, K. Kurihara, T. Mitsumoto, T. Sato, Y. Oshiro, T. Aruga, K. Hasuo, M. Kanemura, and S. Minowada, *Scintigraphic detection of I-125 seeds migration after permanent brachytherapy for prostate cancer: how far do seeds travel?* Clin Nucl Med, 2009. **34**(7): p. 466-9.

Moule, R.N. and P.J. Hoskin, *Non-surgical treatment of localised prostate cancer.* Surg Oncol, 2009.

Nag, S., D. Beyer, J. Friedland, P. Grimm, and R. Nath, *American Brachytherapy Society (ABS) recommendations for transperineal permanent brachytherapy of prostate cancer.* International journal of radiation oncology, biology, physics, 1999. **44**(4): p. 789-99.

Nag, S., J.P. Ciezki, R. Cormack, S. Doggett, K. DeWyngaert, G.K. Edmundson, R.G. Stock, N.N. Stone, Y. Yu, and M.J. Zelefsky, *Intraoperative planning and evaluation of permanent prostate brachytherapy: report of the American Brachytherapy Society.* International journal of radiation oncology, biology, physics, 2001. **51**(5): p. 1422-30.

Nath, S., Z. Chen, N. Yue, S. Trumpore, and R. Peschel, *Dosimetric effects of needle divergence in prostate seed implant using 125I and 103Pd radioactive seeds.* Med Phys, 2000. **27**(5): p. 1058-66.

Nath, S., Z. Chen, N. Yue, S. Trumpore, and R. Peschel, *Dosimetric effects of needle divergence in prostate seed implant using 125I and 103Pd radioactive seeds.* Medical physics, 2000. **27**(5): p. 1058-66.

Nguyen, B.D., S.E. Schild, W.W. Wong, and S.A. Vora, *Prostate brachytherapy seed*

embolization to the right renal artery. Brachytherapy, 2009.

Oh, J.T., M.L. Li, H.F. Zhang, K. Maslov, G. Stoica, and L.V. Wang, *Three-dimensional imaging of skin melanoma in vivo by dual-wavelength photoacoustic microscopy.* J Biomed Opt, 2006. **11**(3): p. 34032.

Okabe, T., G.S. Mintz, A.N. Buch, P. Roy, Y.J. Hong, K.A. Smith, R. Torguson, N. Gevorkian, Z. Xue, L.F. Satler, K.M. Kent, A.D. Pichard, N.J. Weissman, and R. Waksman, *Intravascular ultrasound parameters associated with stent thrombosis after drug-eluting stent deployment.* The American journal of cardiology, 2007. **100**(4): p. 615-20.

Oraevsky, A.A. and A.A. Karabutov, *Optoacoustic tomography*2003: CRC Press.

Oraevsky, A.A., A.A. Karabutov, and E.V. Savateeva, *Enhancement of optoacoustic tissue contrast with absorbing nanoparticles.* Proc. SPIE, 2001. **4434**: p. 60-69.

Park, S., S.R. Aglyamov, W.G. Scott, and S.Y. Emelianov, *Strain imaging using conventional and ultrafast ultrasound imaging: numerical analysis.* IEEE Trans Ultrason Ferroelectr Freq Control, 2007. **54**(5): p. 987-95.

Phal, P.M., D.M. Brooks, and R. Wolfe, *Sonographically guided biopsy of focal lesions: a comparison of freehand and probe-guided techniques using a phantom.* AJR Am J Roentgenol, 2005. **184**(5): p. 1652-6.

Prahl, S.A. *Optical properties spectra compiled by Scott Prahl*. 2001 July 1, 2010]; Available from: http://omlc.ogi.edu/spectra/.

Raymer, M.G., *The silicon web : physics for the Internet age*2009, New York: Taylor & Francis. xxv, 571 p.

Schafhalter-Zoppoth, I., C.E. McCulloch, and A.T. Gray, *Ultrasound visibility of needles used for regional nerve block: an in vitro study.* Reg Anesth Pain Med, 2004. **29**(5): p. 480-8.

Schultz, C.J., P.W. Serruys, M. van der Ent, J. Ligthart, F. Mastik, S. Garg, J.E. Muller, M.A. Wilder, A.F. van de Steen, and E. Regar, *First-in-man clinical use of combined near-infrared spectroscopy and intravascular ultrasound: a potential key to predict distal embolization and no-reflow?* Journal of the American College of Cardiology, 2010. **56**(4): p. 314.

Sethuraman, S., S.R. Aglyamov, J.H. Amirian, R.W. Smalling, and S.Y. Emelianov, *Intravascular photoacoustic imaging using an IVUS imaging catheter.* IEEE

Trans Ultrason Ferroelectr Freq Control, 2007. **54**(5): p. 978-86.

Sethuraman, S., J.H. Amirian, S.H. Litovsky, R.W. Smalling, and S.Y. Emelianov, *Ex vivo Characterization of Atherosclerosis using Intravascular Photoacoustic Imaging.* Opt Express, 2007. **15**(25): p. 16657-66.

Sethuraman, S., J.H. Amirian, S.H. Litovsky, R.W. Smalling, and S.Y. Emelianov, *Spectroscopic intravascular photoacoustic imaging to differentiate atherosclerotic plaques.* Opt Express, 2008. **16**(5): p. 3362-7.

Shah, J., S. Park, S. Aglyamov, T. Larson, L. Ma, K. Sokolov, K. Johnston, T. Milner, and S.Y. Emelianov, *Photoacoustic imaging and temperature measurement for photothermal cancer therapy.* J Biomed Opt, 2008. **13**(3): p. 034024.

Shashkov, E.V., M. Everts, E.I. Galanzha, and V.P. Zharov, *Quantum dots as multimodal photoacoustic and photothermal contrast agents.* Nano Lett, 2008. **8**(11): p. 3953-8.

Shih, C.C., C.M. Shih, Y.L. Chen, Y.Y. Su, J.S. Shih, C.F. Kwok, and S.J. Lin, *Growth inhibition of cultured smooth muscle cells by corrosion products of 316 L stainless steel wire.* J Biomed Mater Res, 2001. **57**(2): p. 200-7.

Shih, C.-C., C.-M. Shih, Y.-Y. Su, L. Hui, J. Su, M.-S. Chang, and S.-J. Lin, *Effect of surface oxide properties on corrosion resistance of 316L stainless steel for biomedical applications.* Corrosion Science, 2004. **46**(2): p. 427-441.

Simpson, C.R., M. Kohl, M. Essenpreis, and M. Cope, *Near-infrared optical properties of ex vivo human skin and subcutaneous tissues measured using the Monte Carlo inversion technique.* Phys Med Biol, 1998. **43**(9): p. 2465-78.

Singh, R. and N.B. Dahotre, *Corrosion degradation and prevention by surface modification of biometallic materials.* J Mater Sci Mater Med, 2007. **18**(5): p. 725-51.

Slottow, T.L., R. Pakala, T. Okabe, D. Hellinga, R.J. Lovec, F.O. Tio, A.B. Bui, and R. Waksman, *Optical coherence tomography and intravascular ultrasound imaging of bioabsorbable magnesium stent degradation in porcine coronary arteries.* Cardiovasc Revasc Med, 2008. **9**(4): p. 248-54.

Stein, E.W., K. Maslov, and L.V. Wang, *Noninvasive, in vivo imaging of blood-oxygenation dynamics within the mouse brain using photoacoustic microscopy.* J Biomed Opt, 2009. **14**(2): p. 020502.

Su, J.L., A.B. Karpiouk, B. Wang, and S.Y. Emelianov, *Photoacoustic imaging of clinical metal needles in tissue.* Journal of Biomedical Optics, 2010. **15**(2): p. 021309-6.

Su, J.L., B. Wang, and S.Y. Emelianov, *Photoacoustic imaging of coronary artery stents.* Opt Express, 2009. **17**(22): p. 19894-901.

Svensson, T., E. Alerstam, M. Einarsdottir, K. Svanberg, and S. Andersson-Engels, *Towards accurate in vivo spectroscopy of the human prostate.* Journal of biophotonics, 2008. **1**(3): p. 200-3.

Tavakoli, M., E.J. Kellar, D. Nassiri, and A.E. Joseph, *A novel polymeric coating for enhanced ultrasound visibility of medical devices.* Med Device Technol, 2006. **17**(2): p. 8-10, 12.

Van Gellekom, M.P., M.A. Moerland, J.J. Battermann, and J.J. Lagendijk, *MRI-guided prostate brachytherapy with single needle method--a planning study.* Radiotherapy and oncology : journal of the European Society for Therapeutic Radiology and Oncology, 2004. **71**(3): p. 327-32.

Vancraeynest, D., A. Pasquet, V. Roelants, B.L. Gerber, and J.L. Vanoverschelde, *Imaging the vulnerable plaque.* Journal of the American College of Cardiology, 2011. **57**(20): p. 1961-79.

Varghese, T. and J. Ophir, *An analysis of elastographic contrast-to-noise ratio.* Ultrasound Med Biol, 1998. **24**(6): p. 915-24.

Wang, B., A.B. Karpiouk, and S.Y. Emelianov, *Design of catheter for combined intravascular photoacoustic and ultrasound imaging.* Proceedings of the 2008 IEEE Ultrasonics Symposium, 2008: p. 1150-1153.

Wang, B., J. Su, J. Amirian, S.H. Litovsky, R. Smalling, and S. Emelianov, *On the possibility to detect lipid in atherosclerotic plaques using intravascular photoacoustic imaging.* Conference proceedings : ... Annual International Conference of the IEEE Engineering in Medicine and Biology Society. IEEE Engineering in Medicine and Biology Society. Conference, 2009. **2009**: p. 4767-70.

Wang, B., J.L. Su, J. Amirian, S.H. Litovsky, R. Smalling, and S. Emelianov, *Detection of lipid in atherosclerotic vessels using ultrasound-guided spectroscopic intravascular photoacoustic imaging.* Optics express, 2010. **18**(5): p. 4889-97.

Wang, L. and S.L. Jacques, *Hybrid model of Monte Carlo simulation and diffusion theory*

for light reflectance by turbid media. Journal of the Optical Society of America. A, Optics, image science, and vision, 1993. **10**(8): p. 1746-52.

Wang, X., Y. Xu, M. Xu, S. Yokoo, E.S. Fry, and L.V. Wang, *Photoacoustic tomography of biological tissues with high cross-section resolution: reconstruction and experiment.* Med Phys, 2002. **29**(12): p. 2799-805.

Wei, Z., M. Ding, D. Downey, and A. Fenster, *3D TRUS guided robot assisted prostate brachytherapy.* Med Image Comput Comput Assist Interv Int Conf Med Image Comput Comput Assist Interv, 2005. **8**(Pt 2): p. 17-24.

Wei, Z., M. Ding, D. Downey, and A. Fenster, *3D TRUS guided robot assisted prostate brachytherapy.* Medical image computing and computer-assisted intervention : MICCAI ... International Conference on Medical Image Computing and Computer-Assisted Intervention, 2005. **8**(Pt 2): p. 17-24.

Westendorp, H., C.J. Hoekstra, A. van't Riet, A.W. Minken, and J.J. Immerzeel, *Intraoperative adaptive brachytherapy of iodine-125 prostate implants guided by C-arm cone-beam computed tomography-based dosimetry.* Brachytherapy, 2007. **6**(4): p. 231-7.

Xu, M. and L.V. Wang, *Photoacoustic imaging in biomedicine.* Review of Scientific Instruments, 2006. **77**(4): p. 041101-22.

Xue, J., F. Waterman, J. Handler, and E. Gressen, *Localization of linked 125I seeds in postimplant TRUS images for prostate brachytherapy dosimetry.* International journal of radiation oncology, biology, physics, 2005. **62**(3): p. 912-9.

Ziskin, M.C., D.I. Thickman, N.J. Goldenberg, M.S. Lapayowker, and J.M. Becker, *The comet tail artifact.* J Ultrasound Med, 1982. **1**(1): p. 1-7.

Vita

Jimmy Su was born in Taipei, TAIWAN on January 1, 1980 to Shey-Min Su and Ruey-Shya Su. His parents immigrated to the United States shortly afterwards, ending up in Austin, Texas. Jimmy obtained a Bachelor's degree in Biomedical Engineering from the Johns Hopkins University in Baltimore, Maryland in the spring of 2002. Following a brief stint at BAE SYSTEMS developing biological agent detection systems, he joined the Nonlinear Biodynamics Laboratory at the University of Texas at Austin working with Dr. Jonathan Dingwell investigating the inherent mechanical stability of human walking using a passive dynamic model. Through this work, Jimmy obtained a Master's degree in Biomedical Engineering from the University of Texas at Austin in May 2006.

For his doctoral studies, Jimmy joined the Ultrasound Imaging and Therapeutics Laboratory under the supervision of Dr. Stanislav Emelianov. His research concentrated on the use of ultrasound and photoacoustic imaging to detect and characterize placement of metal implants in-vivo. The results of his work were published in 4 first author publications. He was also a contributor to a few other articles. He was the 2010-2011 recipient of the President Powers Continuing Fellowship at the University of Texas at Austin.

Permanent email: jimmysu@gmail.com

This dissertation was typed by Jimmy Li-Shin Su